Enrico Roverato

System-Level Design of All-Digital LTE / LTE-A Transmitter Hardware

School of Electrical Engineering

Thesis submitted for examination for the degree of Master of Science in Technology.

Espoo 17.12.2012

Thesis supervisor:

Prof. Jussi Ryynänen

Thesis instructor:

D.Sc. Marko Kosunen

Aalto University
School of Electrical
Engineering

AALTO UNIVERSITY
SCHOOL OF ELECTRICAL ENGINEERING

ABSTRACT OF THE
MASTER'S THESIS

Author: Enrico Roverato

Title: System-Level Design of All-Digital
LTE / LTE-A Transmitter Hardware

Date: 17.12.2012 Language: English Number of pages:10+94

Department of Micro- and Nanosciences

Professorship: Electronic Circuit Design Code: S-87

Supervisor: Prof. Jussi Ryynänen

Instructor: D.Sc. Marko Kosunen

This thesis presents a detailed system-level analysis of an all-digital transmitter hardware based on the Direct-Digital RF-Modulator (DDRM). The purpose of the presented analysis is to evaluate whether this particular transmitter architecture is suitable to be used in LTE / LTE-A mobile phones.

The DDRM architecture is based on the Radio Frequency Digital-to-Analog Converter (RF-DAC), whose system-level characteristics are investigated in this work through mathematical analysis and MATLAB simulations. In particular, a new analytical model for the timing error in the distributed upconversion is developed and verified. Moreover, this thesis reviews the LTE and LTE-A standards, and describes how a baseband environment for signal generation/demodulation can be implemented in MATLAB. The presented system enables much more flexibility with respect to current commercial softwares like Agilent Signal Studio.

Simulation results show that the most challenging specification to meet is the out-of-band noise floor, because of the stringent linearity and timing requirements posed on the RF-DAC. This suggests that new means of reducing the out-of-band noise in all-digital transmitters should be researched, in order not to make their design more complicated than for their analog counterpart.

Keywords: CMOS, Direct-Digital RF-Modulator (DDRM), Radio Frequency Digital-to-Analog Converter (RF-DAC), LTE, LTE-A, timing error, noise floor.

Preface

This thesis was carried out at the Department of Micro- and Nanosciences of Aalto University, School of Electrical Engineering.

I feel extremely thankful to Professor Jussi Ryynänen for giving me the unique opportunity to work in his research group, on such an interesting and challenging topic. I express my sincerest gratitude to my instructor Marko Kosunen for his guidance, expertise, and sense of humor. Special acknowledgments also to the two other members of my research team, Jerry Lemberg and Kari Stadius, for very interesting discussions and new ideas that we shared throughout this year. Thanks also to the rest of my colleagues, especially Lauri Koskinen, for creating a comfortable and relaxing working environment.

I would like to express my warmest thanks to all the people who contributed to make these two years in Finland one of the greatest experiences of my life: Kha, Lur, Ben, Caroline, and many others who have already returned back to their home countries.

My dearest gratitude is reserved to my beloved family. Thanks to my mum, Maria, for taking so much care about my education throughout my life. Without that, I wouldn't be about to start a PhD. Thanks to my dad, Paolo, for teaching me how to enjoy other aspects of life as well, like sports and nature. Without that, I wouldn't have come to study in Finland. Special thanks also to my brother Michele and my sister Giulia.

Finally, I would like to thank my girlfriend Mari for her support during these last weeks of high workload.

Otaniemi, November 2012

Enrico Roverato

Contents

Symbols and abbreviations

Symbols

BW_{occ}	Occupied channel bandwidth
dB	Decibels
dBc	Decibels relative to the Carrier
d_i	LO delay to the i-th cell
f_0	BB signal frequency
f_c	Carrier frequency
F_s	Sampling frequency
$F_{s,0}$	Nominal sampling frequency (with $OSR = 1$)
I_{LSB}	Current corresponding to one LSB
j	Imaginary unit
L_r	Symbol rolloff length
n_0	Time shift (in samples)
N_{bits}	Number of bits
N_{CP}	Cyclic Prefix size (samples)
$N_{CP,0}$	Nominal Cyclic Prefix size (with $OSR = 1$)
N_{FFT}	FFT size (samples)
$N_{FFT,0}$	Nominal FFT size (with $OSR = 1$)
N_{RB}	Number of Resource Blocks
n_s	Slot index
N_{sc}	Number of occupied subcarriers
N_{slots}	Number of slots
N_{symb}	Number of SC-FDMA symbols per slot
N_{ZC}	Length of the Zadoff-Chu sequence
T_{CP}	Cyclic Prefix duration
T_{FFT}	Useful symbol duration
T_{LO}	Local Oscillator period
T_s	Sampling period
V_{DD}	Supply voltage
$x_{BB}(t)$	Baseband signal
$x_{RF}(t)$	RF signal

W_{EVM}	EVM window range
$W_{EVM,0}$	Nominal EVM window range (with $OSR = 1$)
w_{MAX}	Maximum value of jitter signal
$w(n)$	Discrete-time jitter signal
$w(t)$	Continuous-time jitter signal
Δf	Subcarrier spacing
$\varphi(i)$	Phase error profile
$\tilde{\varphi}(a)$	Phase error profile (normalized index)
$\sigma_{I_{LSB}}$	Standard deviation of LSB current

Abbreviations

3G	3^{rd} Generation (cellular standards)
3GPP	3^{rd} Generation Partnership Project
4G	4^{th} Generation (cellular standards)
ACLR	Adjacent Channel Leakage Ratio
AM-AM	Amplitude-Amplitude Modulation
AM-PM	Amplitude-Phase Modulation
BB	Baseband
BPSK	Binary Phase Shift Keying
BW	Channel bandwidth
CA	Carrier Aggregation
CC	Carrier Component
CIM	Counter-intermodulation
CMOS	Complementary Metal-Oxide Semiconductor
CP	Cyclic Prefix
CW	Continuous Wave
DAC	Digital-to-Analog Converter
DDRM	Direct Digital-to-RF Modulator
DFT	Discrete Fourier Transform
DMRS	Demodulation Reference Signal
DNL	Differential Nonlinearity
DSP	Digital Signal Processing
EVM	Error Vector Magnitude
FDD	Frequency-Division Duplexing
FDMA	Frequency-Division Multiple Access
FFT	Fast Fourier Transform
FIR	Finite Impulse Response
GPS	Global Positioning System
I	In-phase
IC	Integrated Circuit
ICI	Inter Carrier Interference

IDFT	Inverse Discrete Fourier Transform
IFFT	Inverse Fast Fourier Transform
INL	Integral Nonlinearity
IRR	Image Rejection Ratio
ISI	Inter-Symbol Interference
ISM	Industrial, Scientific and Medical
LO	Local Oscillator
LSB	Least Significant Bit
LTE	Long Term Evolution
LTE-A	LTE-Advanced
MOS	Metal-Oxide Semiconductor
MSB	Most Significant Bit
OFDM	Orthogonal Frequency Division Multiplexing
OSR	Oversampling Ratio
PA	Power Amplifier
PAPR	Peak-to-Average Power Ratio
PSD	Power Spectral Density
PWM	Pulse-Width Modulation
Q	Quadrature-phase
QAM	Quadrature Amplitude Modulation
QPSK	Quadrature Phase Shift Keying
RB	Resource Block
RF	Radio Frequency
RF-DAC	Radio Frequency Digital-to-Analog Converter
RX	Receiver
SC-FDMA	Single Carrier Frequency Division Multiple Access
SNR	Signal-to-Noise Ratio
TDD	Time-Division Multiplexing
TX	Transmitter
US	Useful Symbol
WCDMA	Wideband Code Division Multiple Access
WLAN	Wireless local Area Network
ZOH	Zero-Order Hold

Chapter 1

Introduction

1.1 Motivation

With the continuous advance of deep sub-micron CMOS technologies, the design of Radio Frequency (RF) circuits is being pushed more and more towards the digital domain. There, IC designers can exploit the growing availability of fast, cheap, and low-power digital logic, which compensates for the increasing difficulty of analog structures to offer adequate RF performance as supply voltage decreases. The ultimate target of this digitalization trend is the so called "all-digital radio transceiver", where most of the RF functions are performed by digital-like circuits, and the interface between analog and digital domains is located just in front of the antenna.

In the context of all-digital transmitters, one of the focus areas of current academic and industrial research is the Direct-digital RF-modulator (DDRM). The DDRM architecture is based on the Radio Frequency Digital-to-Analog Converter (RF-DAC), which is a modified version of the traditional current-steering D/A converter. The RF-DAC combines upconversion, digital-to-analog conversion, and power control into a single mixed-signal circuit. This allows to reduce the number of analog components, with most of the signal processing being moved to the digital front-end.

A large amount of literature has been recently published about the DDRM and RF-DAC structures [1–8]. However, most of the papers only focus on the actual circuit implementation and prototyping. There is lack of good system-level theoretical studies on the DDRM properties. For example, a mathematical model of the nonlinearity caused by error mechanisms in the distributed upconversion has not been developed yet.

The last 20 years have seen a dramatic growth of the mobile communications market. The increasing demand for high-speed connectivity has recently lead to the emerging of the fourth generation (4G) mobile radio standards, such as Long Term Evolution (LTE) and its enhancement LTE-Advanced (LTE-A). These wideband standards bring a great deal of challenges to transmitter design. Even though the DDRM seems to be a mature architecture, recently published LTE transmitters are still mostly based on traditional circuit structures [9, 10].

This thesis addresses the aforementioned issues. The work presented in this

thesis is part of a larger project, funded by Renesas Mobile Europe. The aim of this specific work is to study the DDRM from a system-level point of view, and to evaluate its suitability to be used in a 4G mobile handset, as the core of an LTE / LTE-A radio transmitter.

1.2 Organization of the thesis

The thesis is organized as follows. Chapter 2 provides all the necessary background information. The chapter starts with a general overview about the LTE and LTE-A standards. The DDRM structure is then introduced and compared to the conventional direct-conversion transmitter. The RF requirements for an LTE / LTE-A transmitter are also defined in this chapter.

Chapter 3 delves deep into the details of LTE / LTE-A signal generation and demodulation. Such details are used for the MATLAB implementation of a baseband LTE / LTE-A environment, that enables much more flexibility with respect to commercial softwares like Agilent Signal Studio.

Chapter 4 is the most important part of this thesis. It focuses on the theoretical analysis which is lacking in the published literature about DDRM and RF-DAC. First, a couple of well-known issues in digital signal processing, such as quantization and zero-order hold, are reviewed. Then the non-idealities of the RF-DAC are discussed. Current source mismatches and nonlinear output impedance are widely studied issues, and are just shortly introduced in this thesis. Clock jitter and timing errors are also widely studied, but the way they affect the RF-DAC structure is something worth of analysis. Therefore, the mathematical treatment of these two topics is very thorough, and new analytical models are developed.

Chapter 5 presents the system-level design of an RF-DAC based all-digital transmitter for LTE / LTE-A. The discussion starts from frequency planning and required converter resolution. After that, the first MATLAB simulation results on the ideal DDRM are shown, and some features that can be observed in the output RF spectrum are explained. The last part of the chapter shows what happens when different non-idealities are added to the MATLAB model of the DDRM. All simulation results are compared with the expectations from the theoretical analysis.

Finally, Chapter 6 wraps up the whole work and gives some conclusions.

Chapter 2

Background

2.1 LTE & LTE-A overview

The rapid growth of the mobile communications market has recently lead to the emerging of the so-called fourth generation (4G) mobile radio standards. Originally, the primary goal for 4G systems was set to providing ultra-broadband internet access, with data rate up to 1 Gbit/s [11]. Successively, the definition of 4G was extended, in order to include those technologies representing "a substantial level of improvement in performance and capabilities with respect to the initial third generation systems" [12].

Long Term Evolution (LTE) is a standard for high data rate wireless communications, that has been adopted by the 3^{rd} Generation Partnership Project (3GPP) for the 4G cellular system [13,14]. Unlike 3G systems, LTE is based on Orthogonal Frequency Division Multiplexing (OFDM), a mature technology that is already used in other standards like WiFi and WiMAX. In order to achieve high data rates, OFDM splits the input data into parallel streams, that are used to modulate a number of independent, narrowband subcarriers. These are made orthogonal to each other by selecting the useful OFDM symbol duration T_{FFT} as the inversion of the subcarrier spacing $\Delta f = 15\,\text{kHz}$, in order to avoid Inter Carrier Interference (ICI).

This mechanism can be seen in the frequency domain, as shown in Figure 2.1. Each subcarrier can be thought as a complex exponential $e^{j2\pi k\Delta f t}$, truncated through multiplication by a rectangular window of duration T_{FFT}. The spectrum of such a window is a *sinc* function with zeros at the multiples of $1/T_{FFT} = \Delta f$. Upon multiplication between window and subcarrier, the *sinc* spectrum is frequency shifted by an amount $k\Delta f$, so that its peak corresponds exactly to a zero of all other subcarriers.

The above observation suggests that the spectrum of each OFDM symbol could be sampled at frequencies $k\Delta f$ with no ICI. This leads to the efficient FFT-based implementation of OFDM. The sampled spectrum can be computed directly from the time-domain OFDM symbol by means of a Fast Fourier Transform (FFT), which is an efficient algorithm to calculate the Discrete Fourier Transform (DFT). The number of points N_{FFT} must equal the total number of subcarriers (modulated + guard subcarriers), for the spectrum to be sampled correctly. On the other hand,

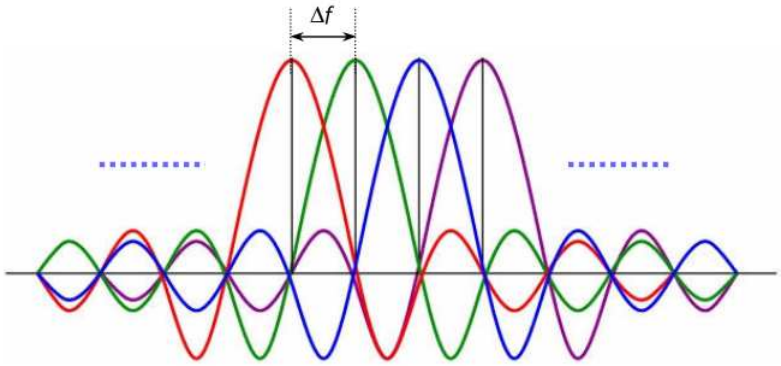

Figure 2.1: Orthogonality between four OFDM subcarriers in the frequency-domain: the peak of each *sinc* pattern corresponds to zeros of other patterns.

a sampled version of the time-domain OFDM symbol can be obtained from the discrete spectrum through Inverse Discrete Fourier Transform (IDFT), which can be efficiently implemented by means of the Inverse Fast Fourier Transform (IFFT) algorithm.[1]

Due to random constructive addition of the subcarriers, OFDM is characterized by a very high Peak-to-Average Power Ratio (PAPR), resulting in poor Power Amplifier (PA) efficiency. This makes pure OFDM implementation unpractical in battery-powered devices such as cellular handsets. For this reason, Single Carrier Frequency Division Multiple Access (SC-FDMA) has been chosen for LTE uplink.[2] SC-FDMA is a modified form of OFDM, with similar throughput performance and complexity, often referred to as DFT-precoded OFDM. Instead of directly using the input stream to modulate the subcarriers, data are first processed by a DFT block, and the resulting spectrum is then "spread" (i.e. mapped) over various subcarriers. Hence, although SC-FDMA is still a multi-carrier scheme, the underlying signal is in fact single-carrier. This leads to about 2 dB lower PAPR compared to OFDM, since the subcarriers are no longer modulated independently.

In LTE, transmission and reception are performed by either Time-Division Duplexing (TDD) or Frequency-Division Duplexing (FDD). TDD consists of transmitting and receiving on the same frequency band, but during different time slots. In FDD mode the transmitter and receiver operate simultaneously, but at different carrier frequencies. The transmit and receive bands are separated by the so-called "duplex distance". In this work, the duplex distance is defined to be positive if the downlink band is located at higher frequencies than the uplink band, negative oth-

[1] In the rest of this thesis, the acronym DFT will be replaced by FFT, and the same with IDFT and IFFT. This is due to the fact that, whenever a DFT/IDFT function is to be computed or implemented, this is always done by means of the efficient FFT/IFFT algorithms. However, the two concepts must not be confused: DFT/IDFT are *discrete transforms*, whereas FFT/IFFT denote a family of *algorithms*.

[2] *Uplink* denotes the transmission from user equipment to base station, whereas *downlink* indicates the transmission in the opposite direction.

Subcarrier spacing (kHz)	Δf	15
Frame duration (ms)		10
Subrame duration (ms)		1
Slot duration (ms)		0.5
US duration (μs)	T_{FFT}	66.7
CP duration, symbol 0 (μs)	T_{CP}	5.21
CP duration, symbols 1-6 (μs)	T_{CP}	4.69

(a) *Parameters that do not depend on BW*

Channel Bandwidth (MHz)	BW	1.4	3	5	10	15	20
Number of RBs	N_{RB}	6	15	25	50	75	100
Sampling rate (MHz)	$F_{s,0}$	1.92	3.84	7.68	15.36	23.04	30.72
FFT size	$N_{FFT,0}$	128	256	512	1024	1536	2048
CP size (symbol 0)	$N_{CP,0}$	10	20	40	80	120	160
CP size (symbols 1-6)	$N_{CP,0}$	9	18	36	72	108	144
Occupied subcarriers	N_{sc}	72	180	300	600	900	1200
Guard subcarriers	$N_{FFT,0} - N_{sc}$	56	76	212	424	636	848
Occupied bandwidth (MHz)	BW_{occ}	1.08	2.7	4.5	9	13.5	18
EVM window range	$W_{EVM,0}$	5	12	32	66	102	136

(b) *Parameters that depend on BW*

Table 2.1: LTE uplink physical layer parameters. Subscript "0" indicates nominal values, that scale proportionally with the oversampling ratio.

erwise. For example, a duplex distance of 80 MHz means that the carrier frequency of the downlink signal is 80 MHz higher than that of the uplink signal.

Table 2.1 lists some important LTE uplink physical layer parameters that will be used throughout this text. LTE transmission supports 6 different channel bandwidths (BWs), from 1.4 up to 20 MHz. Each BW is characterized by a nominal sampling rate $F_{s,0}$, being a multiple or integer fraction of 3.84 Ms/s.[3]

The time-domain structure of an LTE SC-FDMA FDD vector is shown in Figure 2.2. The generic radio frame (Figure 2.2a) has a length of 10 ms. Each frame is divided into 10 subframes of 1 ms duration. Each subframe is further divided into 2 slots of 0.5 ms duration. Each slot usually contains 7 SC-FDMA symbols.[4] Therefore, each frame includes 20 slots and 140 SC-FDMA symbols. However, not all of the 7 SC-FDMA symbols in each slot are dedicated to data transmission. For example, the 4^{th} symbol is reserved for Demodulation Reference Signal (DMRS)

[3] 3.84 Ms/s is also the chip rate defined in the WCDMA (3G) standard. Using integer ratios alleviates the design of multistandard devices.

[4] In some special applications (e.g. very large cells in rural areas), the number of symbols for each slot can be configured to be 6, corresponding to a longer Cyclic Prefix (CP) duration. This option is meaningless for the purposes of this thesis, and thus it will not be considered.

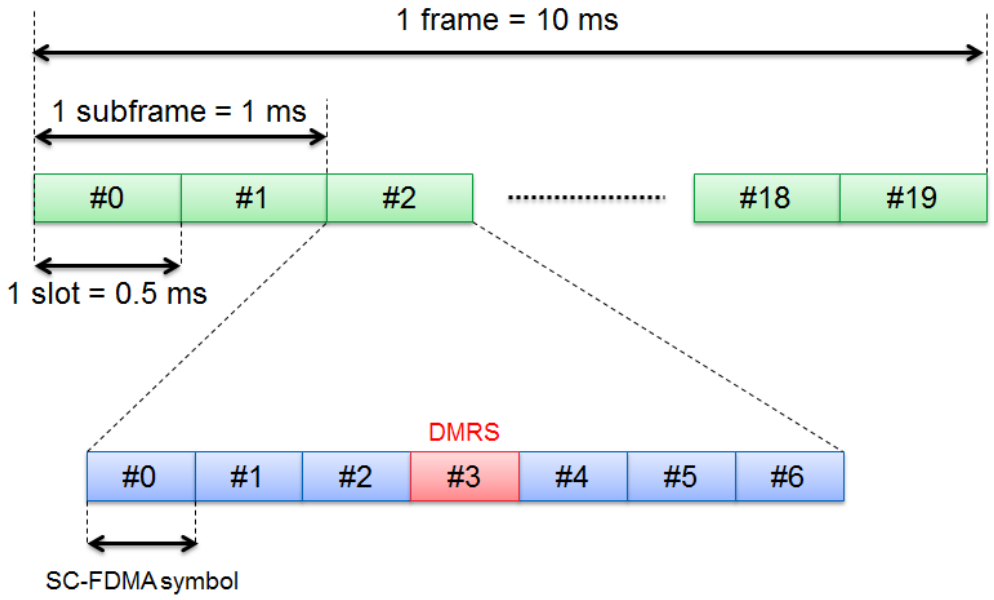

(a) *Radio frame structure*

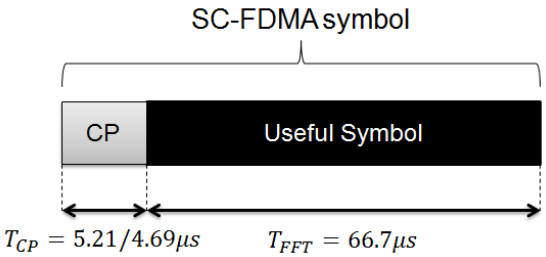

(b) *SC-FDMA symbol structure*

Figure 2.2: Time-domain structure of an LTE SC-FDMA FDD vector.

transmission. This is a predefined sequence, that is used in the receiver for various purposes (e.g. coherent demodulation).

As shown in Figure 2.2b, each SC-FDMA symbol consists of two parts: the Useful Symbol (US) and the Cyclic Prefix (CP). The US corresponds to the IFFT of N_{FFT} data samples. The CP is a copy of the last N_{CP} samples of the US, and it is used to eliminate the Inter-Symbol Interference (ISI) caused by multipath-induced delay spread in the radio channel. For a 7-symbol SC-FDMA slot, the CP of the first symbol is longer than for the remaining 6 symbols, resulting in exact 0.5 ms slot duration.

The subcarriers can be represented in the time-frequency space, on a grid of Resource Blocks (see Figure 2.3). A RB is the smallest element of resource allocation, consisting of 12 subcarriers (180 kHz) for the duration of one slot. Different RBs are assigned to different users by the base station scheduler, allowing traffic to be multiplexed to the same channel. In the case of full-filled LTE vectors, i.e. all of

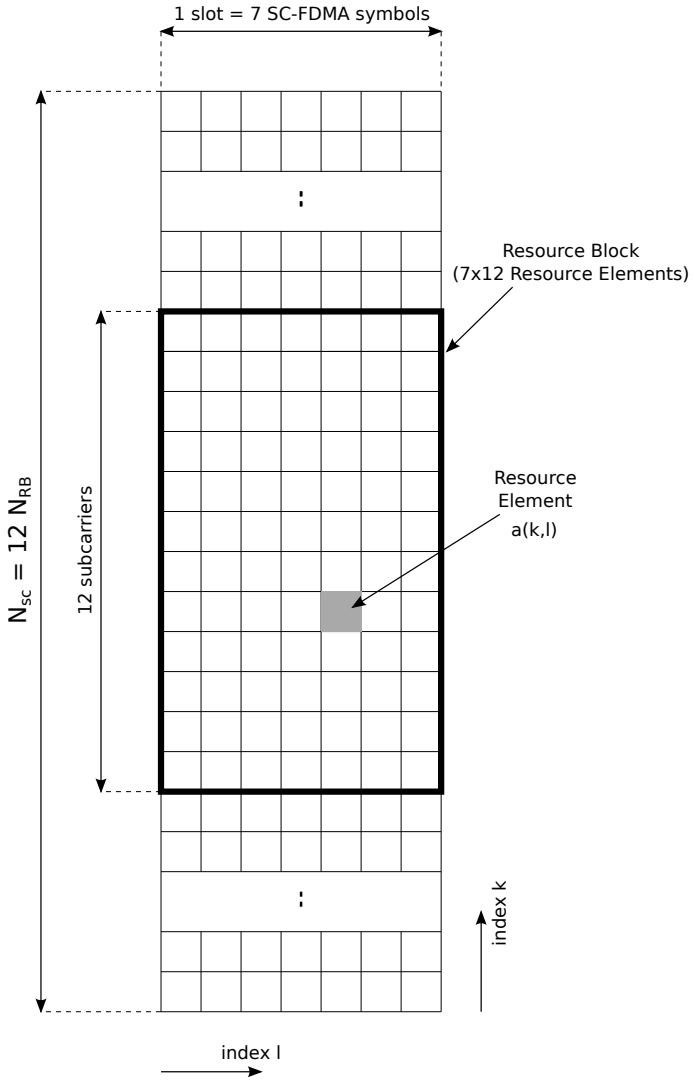

Figure 2.3: Uplink resource grid.

the available RBs are assigned to a single user, the number of occupied subcarriers is then given by $N_{sc} = 12N_{RB}$.

The LTE-Advanced (LTE-A) standard is an enhancement of LTE, designed to support even higher data rates while maintaining backward compatibility [15]. Higher data rates are achieved thanks to the Carrier Aggregation (CA) technique, where multiple LTE carriers (Carrier Components, CCs) are "aggregated" in order to obtain transmission bandwidths up to 100 MHz. Carrier aggregation can be "intra-band", when multiple CCs are aggregated in the same operating band, or "inter-band", when the CCs are located in different operating bands. In this work, for simplicity, only intra-band CA of two contiguous carriers (15+15 or 20+20 MHz) is considered. In such case, the LTE-A carrier is simply obtained as the sum of two independent, frequency-shifted LTE vectors, as illustrated in Figure 2.4.

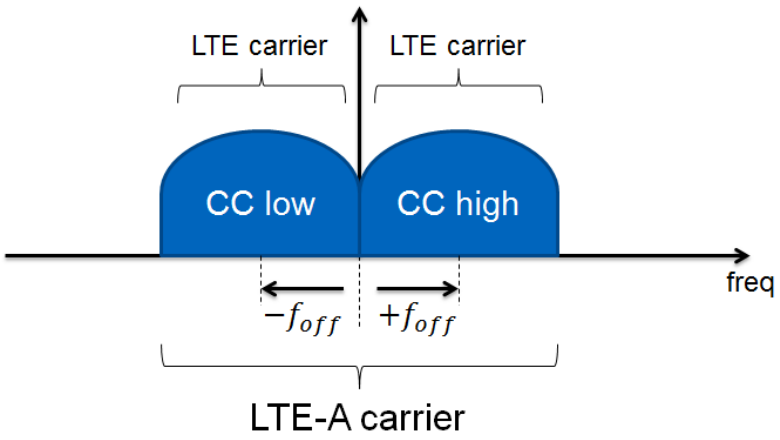

Figure 2.4: Carrier Aggregation (CA) of two independent LTE carriers.

2.2 Principle of I-Q modulation

Most recent radio standards, including LTE and LTE-A, are based on the In-phase/Quadrature-phase (I-Q) modulation scheme, also known as quadrature amplitude modulation [16,17]. In this scheme, two baseband data streams, $I(t)$ and $Q(t)$, are upconverted to Radio Frequency (RF) by means of mixing with two 90°-shifted carriers, according to

$$x_{RF}(t) = I(t) \cdot \cos(2\pi f_c t) - Q(t) \cdot \sin(2\pi f_c t), \tag{2.1}$$

where f_c is the carrier frequency, and $x_{RF}(t)$ is the output of the I-Q modulator.

If we define the "complex" baseband signal as

$$x_{BB}(t) = I(t) + jQ(t), \tag{2.2}$$

then the output RF signal can be expressed in the form

$$x_{RF}(t) = \mathrm{Re}\big[x_{BB}(t) \cdot e^{j2\pi f_c t}\big], \tag{2.3}$$

where the exponential term represents the RF carrier. In the frequency-domain, equation (2.3) is equivalent to shifting the spectrum of $x_{BB}(t)$ by a quantity f_c. Since taking the real part in (2.3) only causes the RF spectrum to be mirrored with respect to the y-axis[5], the complex form of the I-Q modulation formula will be sometimes used in the next chapters, in order to ease the mathematical analysis.

If the complex baseband signal is written with the modulus/phase notation

$$x_{BB}(t) = |x_{BB}(t)|e^{j\phi(t)}, \tag{2.4}$$

where $\phi(t) = \angle x_{BB}(t)$, equation (2.3) takes the form

$$x_{RF}(t) = \mathrm{Re}\big[|x_{BB}(t)| \cdot e^{j(2\pi f_c t + \phi(t))}\big], \tag{2.5}$$

[5]The spectrum of a real signal always presents *hermitian symmetry*.

which explicitly shows that both the amplitude and phase of the carrier are modulated by the baseband data. This feature is the main advantage of I-Q modulation, because twice as much data as with simple in-phase modulation can be transmitted over the same frequency band.

As will be explained in the next sections, many performance metrics of I-Q modulators are measured by feeding a single tone with frequency f_0 as input signal. The complex baseband input is

$$x_{BB}(t) = e^{j2\pi f_0 t}, \tag{2.6}$$

which can be split into the I and Q components

$$I(t) = \mathrm{Re}\big[x_{BB}(t)\big] = \cos(2\pi f_0 t), \tag{2.7a}$$
$$Q(t) = \mathrm{Im}\big[x_{BB}(t)\big] = \sin(2\pi f_0 t). \tag{2.7b}$$

The ideal RF output signal is given by substituting (2.6) into (2.3), yielding

$$x_{RF}(t) = \mathrm{Re}\big[e^{j2\pi(f_c+f_0)t}\big] = \cos\big(2\pi(f_c+f_0)t\big). \tag{2.8}$$

Equation (2.8) states that the ideal output of an I-Q modulator fed with the cosine/sine inputs given by (2.7a) and (2.7b) should be a single tone located at $f_c + f_0$. Possible tones at other frequencies are classified as spurs, being caused by the non-idealities of any real implementation of the I-Q modulation.

2.3 Transmitter structures

The I-Q modulation scheme can be implemented with a number of different transmitter architectures [17]. This section focuses on two particular realizations: the direct-conversion transmitter, and the direct-digital RF transmitter. Both structures can be conceptually divided into two parts: the I-Q modulator itself, which produces the output signal given by (2.1), and the Power Amplifier (PA), which amplifies the RF signal to a level suitable for transmission. The focus of this thesis will be on the I-Q modulator only.

2.3.1 Direct-conversion transmitter

One of the most common architectures used to implement the I-Q modulation scheme is the direct-conversion transmitter [16, 17], shown in Figure 2.5. In such architecture, the baseband digital signals $I(n)$ and $Q(n)$ from the Digital Signal Processing (DSP) block are converted to analog by two Digital-to-Analog Converters (DACs), followed by reconstruction low-pass filters and optional gain control stages. The resulting $I(t)$ and $Q(t)$ are then upconverted directly to the carrier frequency f_c (which equals the Local Oscillator (LO) frequency), by means of mixing with in-phase and quadrature-phase carriers. An RF bandpass filter is used to filter out the generated spurs and noise outside the operating band. Finally, the RF signal goes through an additional gain control stage, before being amplified by the PA.

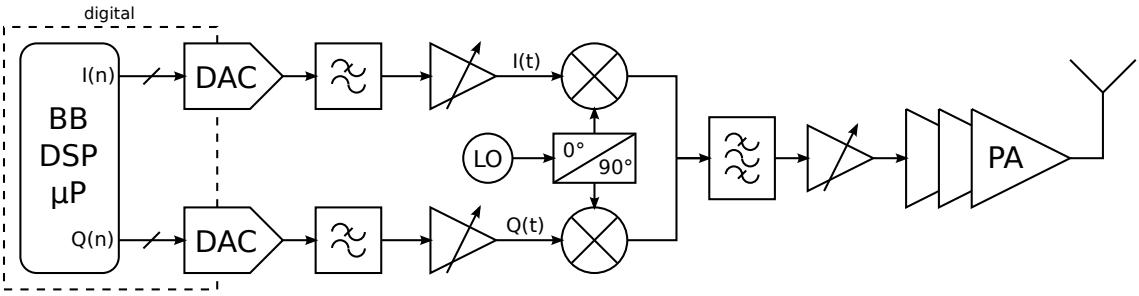

Figure 2.5: Direct-conversion transmitter architecture.

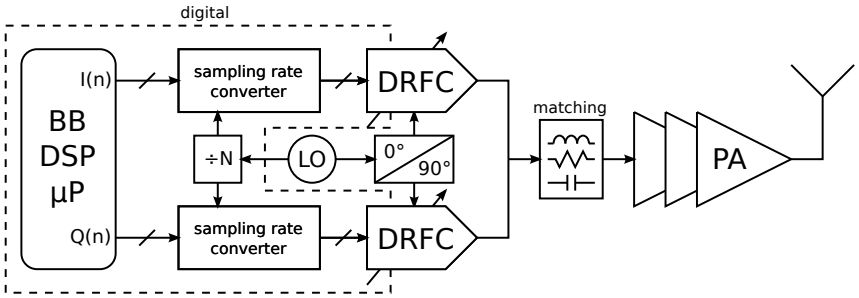

Figure 2.6: Direct-digital RF-modulator architecture.

The disadvantage of the architecture shown in Figure 2.5 is its analog-intensive signal processing. Area and power consumption do not benefit from technology scaling in the same extent as DSP. Furthermore, some typical impairments coming from the analog baseband, such as DC-offset and amplitude/phase mismatches between the I and Q branches, increasingly affect the modulator performance, and often require calibration. This motivates the research of structures that perform most of the functions within DSP.

2.3.2 Direct-digital RF transmitter

In the context of radio transmitters, the digitalization trend started over one decade ago with digital baseband modulators [18, 19]. However, the first effort towards an "all-digital" solution is the Direct-digital RF-modulator (DDRM) [1–8], whose block diagram is presented in Figure 2.6. In the DDRM, the increased sampling rate of the digital baseband signal allows to remove the analog reconstruction filters from the signal path, i.e. the functionality of the baseband filters is now moved to the DSP side of the transmitter.

The DDRM is based on an I-Q modulator constructed with two Radio Frequency Digital-to-Analog Converters (RF-DACs), also known as Digital-to-RF Converters (DRFCs). The RF-DAC is a traditional current-steering DAC, where an additional pair of switching transistors is integrated in each unit conversion cell, in a "Gilbert mixer"-like fashion. This enables to perform the upconversion individually for each

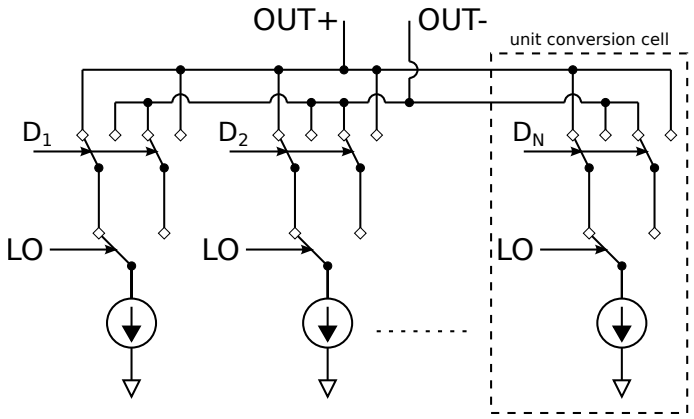

(a) *Working principle*

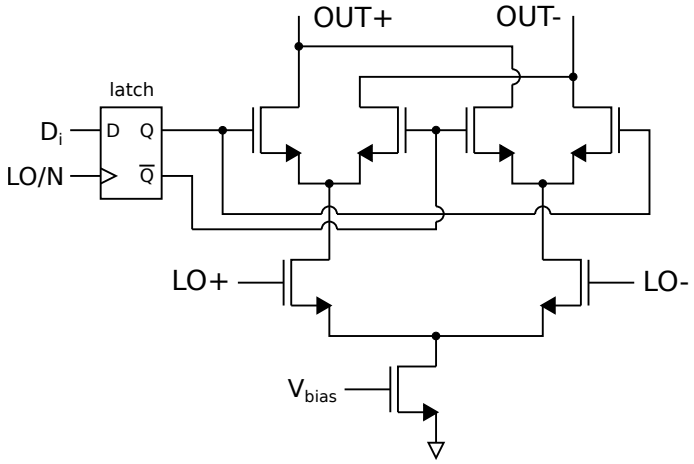

(b) *Possible implementation of the unit conversion cell*

Figure 2.7: Radio Frequency Digital-to-Analog Converter.

of the digital unit signals, together with the D/A conversion. Figures 2.7a and 2.7b show the working principle of the RF-DAC and one possible implementation of the unit conversion cell respectively.

Like in a traditional current-steering DAC, segmentation can be adopted in the converter, which consists of partitioning the N_{bits} bits of the digital input word into M Most Significant Bits (MSBs) and $L = N_{bits} - M$ Least Significant Bits (LSBs). Thermometer- or binary-coding can be used to size the current source transistors of the unit conversion cells in the MSB and LSB blocks, such that the D/A conversion is performed independently for MSBs and LSBs, and the resulting analog signals are then summed at the output. This partitioning sets a trade-off between DC linearity (transistor mismatches) and circuit complexity (number of conversion cells). In order not to complicate the distribution of the high-frequency LO signal to the unit cells, the avoidance of excessive complexity turns out to be the preferable choice in RF-DACs [3].

In the RF-DAC, the sampling rate of the digital baseband input can be derived

through integer multiplication/division from either the baseband processor clock, or the LO clock. The latter approach is advantageous because the occurrence of glitches in the output signal is avoided [5,7], thus resulting in a cleaner RF spectrum. However, when the DDRM is targeted to a specific radio standard, the LO frequency is usually specified to be changeable. Hence, programmable fractional sampling rate converters are needed in the DDRM, as shown in Figure 2.6, in order to provide the necessary interface between baseband DSP processor and RF-DACs. Because of the missing analog reconstruction filter, such sampling rate converters should also increase the oversampling ratio of the baseband signal as much as possible. Indeed, this alleviates the problems of repetition spectrum and out-of-band quantization noise to a level that can be handled by the RF matching network, without need of complex analog bandpass filters.

The advantages of the DDRM over the direct-conversion transmitter are several. First, the baseband signal processing is now entirely digital, making it immune to DC-offset and amplitude/phase mismatches between the I and Q branches. Second, the amplitude of the RF signal is defined by the number of parallel current sources currently connected to the output. Therefore, the linearity of the output signal is ideally defined by the linearity of the D/A converter. Third, it is possible to handle most of the power control by simply adjusting the bias current of the converters, thus avoiding the need of variable gain amplifiers. Finally, as most of the transistors act as switches, the DDRM is a "digitally-intensive" architecture, thus it benefits more from technology scaling than its analog direct-conversion counterpart.

2.4 Requirements for LTE / LTE-A transmitter

This section gives a detailed overview of the RF requirements for an LTE[6] User Equipment (UE) radio transmitter [20]. Performance requirements are derived for the I-Q modulator only, which is the main focus of this thesis. However, the typical characteristics of PAs are taken into account during the derivation.

2.4.1 Transmission bandwidth

LTE increases spectrum flexibility by supporting multiple channel bandwidths of 1.4, 3, 5, 10, 15, and 20 MHz, as well as the CA bandwidths of 10+20, 15+15, 15+20, and 20+20 MHz. The highest transmission bandwidth to be supported is thus 40 MHz. This is 8 times larger than the 5 MHz channel bandwidth of 3G WCDMA systems.

Due to this high bandwidth requirement, wideband techniques are needed while designing the TX circuit.

Band	UL freq. range (MHz)	DL freq. range (MHz)	Band width (MHz)	Allowed BWs (MHz)	Duplex mode	Duplex dist. (MHz)
1	1920 - 1980	2110 - 2170	60	5, 10, 15, 20, 15+15, 20+20	FDD	190
2	1850 - 1910	1930 - 1990	60	1.4, 3, 5, 10, 15, 20	FDD	80
3	1710 - 1785	1805 - 1880	75	1.4, 3, 5, 10, 15, 20	FDD	95
4	**1710 - 1755**	**2110 - 2155**	**45**	**1.4, 3, 5, 10, 15, 20**	**FDD**	**400**
5	**824 - 849**	**869 - 894**	**25**	**1.4, 3, 5, 10**	**FDD**	**45**
6	Not applicable	Not applicable				
7	**2500 - 2570**	**2620 - 2690**	**70**	**5, 10, 15, 20**	**FDD**	**120**
8	880 - 915	925 - 960	35	1.4, 3, 5, 10	FDD	45
9	1749.9 - 1784.9	1844.9 - 1879.9	35	5, 10, 15, 20	FDD	95
10	**1710 - 1770**	**2110 - 2170**	**60**	**5, 10, 15, 20**	**FDD**	**400**
11	**1427.9 - 1447.9**	**1475.9 - 1495.9**	**20**	**5, 10**	**FDD**	**48**
12	**699 - 716**	**729 - 746**	**17**	**1.4, 3, 5, 10**	**FDD**	**30**
13	**777 - 787**	**746 - 756**	**10**	**5, 10**	**FDD**	**-31**
14	**788 - 798**	**758 - 768**	**10**	**5, 10**	**FDD**	**-30**
15	Reserved	Reserved	-		FDD	-
16	Reserved	Reserved	-		FDD	-
17	**704 - 716**	**734 - 746**	**12**	**5, 10**	**FDD**	**30**
18	**815 - 830**	**860 - 875**	**15**	**5, 10, 15**	**FDD**	**45**
19	830 - 845	875 - 890	15	5, 10, 15	FDD	45
20	**832 - 862**	**791 - 821**	**30**	**5, 10, 15, 20**	**FDD**	**-41**
21	**1447.9 - 1462.9**	**1495.9 - 1510.9**	**15**	**5, 10, 15**	**FDD**	**48**
22	3410 - 3490	3510 - 3590	80	5, 10, 15, 20	FDD	100
23	2000 - 2020	2180 - 2200	20	1.4, 3, 5, 10	FDD	180
24	**1626.5 - 1660.5**	**1525 - 1559**	**34**	**5, 10**	**FDD**	**-101.5**
25	1850 - 1915	1930 - 1995	65	1.4, 3, 5, 10, 15, 20	FDD	80
26	**814 - 849**	**859 - 894**	**35**	**1.4, 3, 5, 10, 15**	**FDD**	**45**
...						
33	1900 - 1920	1900 - 1920	20	5, 10, 15, 20	TDD	
34	2010 - 2025	2010 - 2025	15	5, 10, 15	TDD	
35	1850 - 1910	1850 - 1910	60	1.4, 3, 5, 10, 15, 20	TDD	
36	1930 - 1990	1930 - 1990	60	1.4, 3, 5, 10, 15, 20	TDD	
37	1910 - 1930	1910 - 1930	20	5, 10, 15, 20	TDD	
38	2570 - 2620	2570 - 2620	50	5, 10, 15, 20	TDD	
39	1880 - 1920	1880 - 1920	40	5, 10, 15, 20	TDD	
40	**2300 - 2400**	**2300 - 2400**	**100**	**5, 10, 15, 20, 10+20, 15+15, 20+20**	**TDD**	
41	**2496 - 2690**	**2496 - 2690**	**194**	**5, 10, 15, 20, 10+20, 15+15, 15+20, 20+20**	**TDD**	
42	3400 - 3600	3400 - 3600	200	5, 10, 15, 20	TDD	
43	3600 - 3800	3600 - 3800	200	5, 10, 15, 20	TDD	

Table 2.2: LTE operating bands. Some critical bands discussed in the frequency planning (Section 5.1) are highlighted in bold.

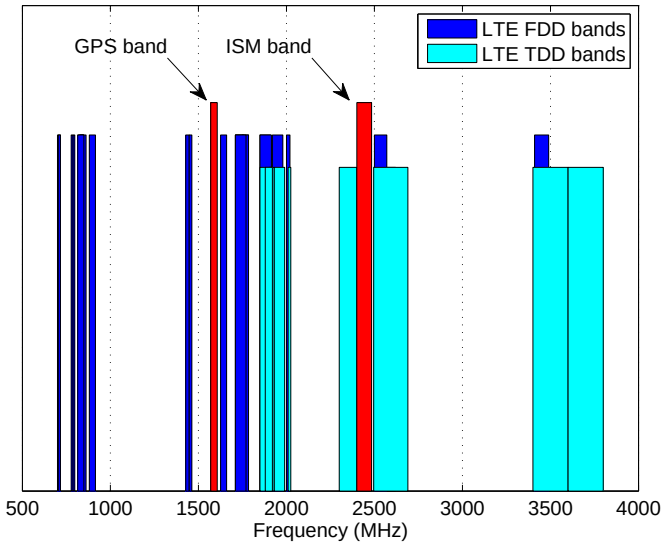

Figure 2.8: Location of the GPS, ISM, and LTE uplink bands on the radio spectrum.

2.4.2 Operating bands

LTE is designed to operate in the frequency bands defined in Table 2.2. Each row of Table 2.2 specifies the band number, the frequency ranges for transmission (Uplink, UL) and reception (Downlink, DL), the width of the operating band, the allowed LTE channel bandwidths (BWs) on that specific band, the duplex mode (FDD or TDD), and the duplex distance (when duplex mode is FDD).

The location of the uplink frequency bands on the radio spectrum is plotted in the graph of Figure 2.8. It can be noticed that the bands can be gathered into four groups:

- Group I: 699 - 915 MHz;
- Group II: 1427.9 - 2025 MHz;
- Group III: 2300 - 2690 MHz;
- Group IV: 3400 - 3800 MHz.

The coverage of such a broad radio spectrum, from 0.7 to 3.8 GHz, is extremely challenging from the TX point of view. The highest carrier frequency is more than 5 times larger than the lowest one. Because RLC structures typically used in RF circuits can be only optimized for a narrow range of frequencies, tuning or parallelism is required in order to cover all uplink frequency bands [8].

[6]Throughout the rest of this section, "LTE" will stand for both LTE / LTE-A.

2.4.3 Output power

Output power requirements are demanding in LTE systems. Maximum, minimum and OFF transmit powers are specified to be 23, -40, and -50 dBm respectively. The total power control range when the TX is ON is thus 63 dB.

By assuming a PA with a power gain in the neighborhood of 20 dB [21], the maximum average output power of I-Q modulator alone must be 3 dBm. Since the PAPR of LTE uplink signals is about 8.5 dB [22], the corresponding peak power turns out to be 11-12 dBm. This power has to be delivered to the input impedance of the PA, which is typically $50\,\Omega$ ($100\,\Omega$ if the PA input is differential).

2.4.4 Linearity

Another challenge in LTE systems is set by linearity requirements. In a practical transmitter, linearity is usually dominated by the performance of the PA. However, the linearity of the I-Q modulator must leave enough margin for the PA, without excessive power consumption penalty. Therefore, the requirements for the I-Q modulator are stricter than defined by the specific radio standard.

The easiest way to see the nonlinearities is to transmit a single baseband tone, and look at the RF output spectrum. The most significant spurs that can be observed are the 3^{rd} Harmonic Distortion (HD_3), and the 3^{rd} Counter Intermodulation product (CIM_3). On the other hand, nonlinearities can be also observed by directly testing the transmitter in an LTE environment. Due to the complex modulation used in LTE, two parameters are affected by nonlinearities: Adjacent Channel Leakage Ratio (ACLR), and Error Vector Magnitude (EVM).

Harmonic Distortion and Counter Intermodulation

As demonstrated in Section 2.2, if we upconvert a baseband tone with frequency f_0 to RF with an ideal I-Q modulator, the only output is a single tone located at frequency $f_c + f_0$. However, due to nonlinearities in the circuit, some extra tones will also appear in the RF output spectrum. These tones are located at frequencies that can be generally expressed in the form

$$f_i = mf_c \pm nf_0, \tag{2.9}$$

where m and n are integers. Specifications for distortion products are usually given in the form of power ratio.

One important figure of merit in radio transmitters is the 3^{rd} Harmonic Distortion (HD_3), located at $f_{HD3} = 3f_c \pm f_0$ (see Figure 2.9), which originates from the large third harmonic of the square-wave LO signal.[7] The transmitter must filter out the HD_3 component, which would otherwise result in unwanted out-of-band power.

[7]The term "Harmonic Distortion" is therefore slightly inappropriate, because the third RF harmonic of the signal at $f_c + f_0$ is by definition located at $3(f_c + f_0)$. However, since $f_c \gg f_0$, this imprecision is insignificant to our purposes, and HD_3 will be used to indicate whatever spurs are located around $3f_c$.

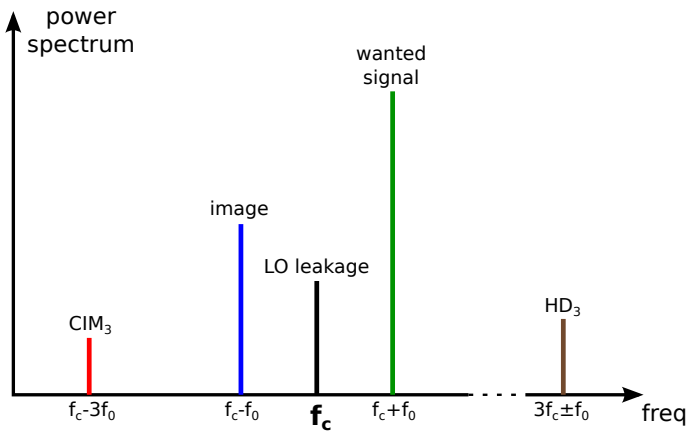

Figure 2.9: Location of wanted signal, distortion components HD_3 and CIM_3, LO leakage, and image tone on the output RF spectrum of a real I-Q modulator, when the baseband input signals are cosine/sine.

Since f_{HD3} is located around three times the carrier frequency, filtering requirements at RF are quite relaxed. However, if f_c is specified to be changeable, it is possible that a single filter cannot be used at the RF output. In LTE, for example, it can be seen from Figure 2.8 that the HD_3 of the operating bands around 800 MHz, being located near 2.4 GHz, falls exactly within some higher-frequency bands.

Another critical figure of merit specific to LTE transmitters is the 3^{rd} Counter Intermodulation product [10], or CIM_3, which is located at $\pm 3f_0$ offset from the carrier frequency (e.g. $f_{CIM3} = f_c - 3f_0$, see Figure 2.9). This is thus an expression of the third-order nonlinearity in the *baseband* signal. This parameter must be well controlled, because it directly causes in-band emissions when only part of the available LTE channel bandwidth is actually used to transmit information. If we account for further degradation introduced by the PA, values of CIM_3 below -60 dBc can be considered good enough for the I-Q modulator [10].

Adjacent Channel Leakage Ratio

Adjacent Channel Leakage Ratio (ACLR) is defined as the ratio of the filtered mean power centered on the assigned channel P_{Ch}, to the filtered mean power centered on the n-th adjacent channel $P_{adj,n}$ [23]. This concept, illustrated in Figure 2.10, is expressed by

$$ACLR_n = 10\log_{10}\left(\frac{P_{Ch}}{P_{adj,n}} \cdot \frac{BW_{adj,n}}{BW_{occ}}\right), \tag{2.10}$$

where the rightmost normalization factor is needed to compare powers correctly when main and adjacent channels have different occupied bandwidths BW_{occ} and $BW_{adj,n}$ respectively. The LTE standard specifies ACLR requirements in two cases.

- The first adjacent channel is another LTE channel of the same bandwidth: $ACLR_1 \geqslant 30\,\text{dB}$.

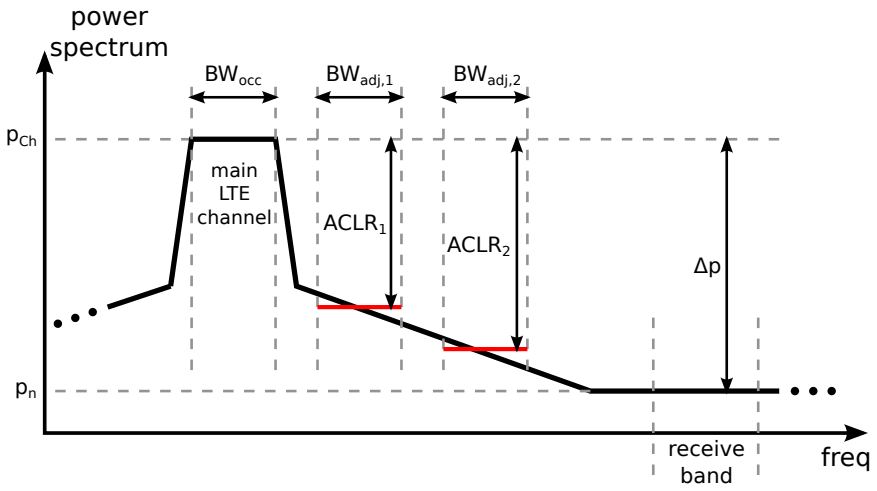

Figure 2.10: Illustration of Adjacent Channel Leakage Ratio for the first two adjacent channels, and noise floor in one of the receive bands.

- The first two adjacent channels are 3G WCDMA channels: $ACLR_1 \geqslant 33\,\text{dB}$, and $ACLR_2 \geqslant 36\,\text{dB}$.[8]

In order to leave enough room for the PA, the ACLR at the output of the I-Q modulator must be higher than the values given above. Acceptable values for ACLR from recently published LTE I-Q modulators [9, 10] range around 45 dB.

Error Vector Magnitude

Error Vector Magnitude (EVM) is the average deviation of the received constellation points $S_{rx}(i)$, $i = 1, \ldots, N$, from the ideal points $S_{id}(i)$, expressed as a percentage of the average symbol magnitude. "Received constellation points" means that the symbols are demodulated from the waveform measured at the TX output. The basic formula for EVM calculation is

$$EVM = \sqrt{\frac{\sum_{i=1}^{N} \left| S_{rx}(i) - S_{id}(i) \right|^2}{N \cdot P_{avg}}} \cdot 100, \tag{2.11}$$

where P_{avg} is the average power of the N ideal symbols. The LTE standard [20] explains in details how to perform EVM measurements, and Chapter 3 will treat this topic extensively. LTE specifications for EVM are as follows.

- For QPSK or BPSK modulation schemes: $EVM < 17.5\%$.
- For 16-QAM modulation scheme: $EVM < 12.5\%$.

[8] There is no $ACLR_2$ requirement for the 1.4 and 3 MHz LTE channel bandwidths.

Again, EVM specifications at the output of the I-Q modulator must account for further degradation coming from the PA. According to recent literature [3, 6, 8, 9], an EVM below 4% can be considered good enough.

2.4.5 LO leakage

Local Oscillator (LO) leakage is an additive sinusoidal waveform at the RF output of the transmitter, having the same frequency f_c as the carrier signal. In direct-conversion transmitters, this effect originates from DC offset in the analog baseband circuitry, mismatches in the I-Q modulator, and direct coupling of the LO signal to the TX output [3]. LO leakage is measured by transmitting a single tone with frequency f_0, and calculating the ratio between the powers of the leakage and wanted signals. As shown in Figure 2.9, LO leakage is well visible on the RF output spectrum, as an unwanted tone located at frequency f_c.

Although the LTE standard specifies an upper limit for the LO leakage of -25 dBc (at high output power), a good target for the I-Q modulator (accounting for PA non-idealities) is -40 dBc [1, 9].

2.4.6 Image Rejection Ratio

In addition to the single tone located at frequency $f_c + f_0$, some non-idealities in the circuit (e.g. deviation of the LO signal phase shift from 90°, amplitude and phase mismatches affecting the signal along the I and Q branches of a direct-conversion transmitter [3]), may cause an unwanted "image" tone at $f_c - f_0$ to appear in the RF output spectrum as well, as shown in Figure 2.9. Image Rejection Ratio (IRR) is calculated as the ratio between the power of this image tone, and that of the wanted tone.

Although the LTE standard does not mention any explicit limit for this parameter, a poor IRR has a direct influence on the modulation quality. Acceptable values for IRR are in the neighborhood of -45 dBc [1, 3].

2.4.7 Noise floor

Noise floor requirements are perhaps the most troublesome in LTE. When the transceiver operates in FDD mode, the finite isolation between TX and RX may lead to interference between the two circuits. An excess of TX power leaking to the RX-band can potentially block the reception of weak signals, thus degrading the receiver sensitivity. Therefore, in order to ensure a correct FDD operation, the out-of-band noise produced by the transmitter must be as low as possible in the own RX-band. Moreover, a 4G handheld device is likely to support other radio standards as well, such as Bluetooth, Global Positioning System (GPS), and Wireless Local Area Network (WLAN). In order to permit coexistence of different radios, the out-of-band noise of the LTE transmitter is required to be also very low in the receive bands of the considered standards.

BW (MHz)	$f_{DD,min}$ (MHz)	Δp_{min} (dB)
1.4	30	100
3	30	96
5	30	93
10	30	90
15	-41	89
20	-41	87
15+15	190	85
20+20	190	84

Table 2.3: Minimum duplex distance ($f_{DD,min}$) and required relative noise power density (Δp_{min}) for each LTE channel bandwidth.

The duplex distances of all LTE FDD bands are listed in Table 2.2. For simplicity, the minimum duplex distances for each LTE channel bandwidth are reported in Table 2.3. Figure 2.8 highlights the location of the ISM and GPS bands on the radio spectrum (the ISM band is used by both Bluetooth and WLAN radios). The TX noise must be low enough in all of these bands. If such requirement is not met by the TX itself, a Surface Acoustic Wave (SAW) isolation filter is needed before the PA, which is very undesirable in a multiband transmitter.

By taking into account duplexer attenuation and receiver sensitivity, the allowed TX noise level at maximum transmit power is typically around -160 dBc/Hz for SAW-less operation [8–10]. This is actually a measure of noise density to channel power. However, since the in-band Power Spectral Density (PSD) of LTE signals is flat, it is more practical to relate the noise level to the channel PSD. As shown in Figure 2.10, the difference Δp between the two power density levels p_{Ch} (for the main channel) and p_n (for the noise) is immediately visible on the RF output spectrum.

In order to calculate a lower limit for Δp, let us first determine the main channel power P_{Ch} by integrating the channel power density over the occupied channel bandwidth BW_{occ}:

$$P_{Ch} = p_{Ch} + 10 \log_{10} BW_{occ} \qquad [\text{dBm}], \tag{2.12}$$

where the factor $10 \log_{10} BW_{occ}$ can assume values in the range $60 \sim 76$ dB depending on the LTE channel bandwidth. Table 2.1 lists the values of BW_{occ} for channel bandwidths from 1.4 up to 20 MHz. The noise level is defined as the difference between p_n and P_{Ch}, and it should be smaller or equal to -160 dBc/Hz, as expressed by

$$p_n - P_{Ch} = p_n - \left(p_{Ch} + 10 \log_{10} BW_{occ}\right) \leqslant -160, \tag{2.13}$$

which can be inverted to yield

$$\Delta p = p_{Ch} - p_n \geqslant 160 - 10 \log_{10} BW_{occ} = 84 \sim 100\,\text{dB}. \tag{2.14}$$

The above calculation shows that the "height" of the LTE signal over the noise floor in the RF bands of interest (see Figure 2.10) must be in the order of 90 dB,

Channel bandwidth	40 MHz
Carrier frequency	0.7 - 3.8 GHz
Output power	3 dBm
CIM_3	-60 dBc
LO leakage	-40 dBc
IRR	-45 dBc
EVM	4%
$ACLR_{1,2}$	45 dB
Noise floor	-160 dBc/Hz

Table 2.4: Typical targets for LTE I-Q modulator, as derived in the previous subsections.

which is a very tight requirement. Table 2.3 gives the exact values of the minimum allowed Δp for each channel bandwidth.

2.4.8 Summary of transmitter requirements

Table 2.4 summarizes the requirements for the I-Q modulator that were defined and justified in the previous subsections. These values will be used in Chapter 5 in order to evaluate the maximum allowed level of various modulator impairments.

Chapter 3

Signal generation and demodulation

The design of a highly configurable transmitter for LTE and LTE-A requires acquaintance with the flexibility inherent to these radio standards. From the RF designer's point of view, the best way to familiarize with such flexibility is to fully understand the operation of the overall transceiver chain, including the baseband signal processing. For this reason, a consistent part of this work is dedicated to study, from a practical perspective, how signal modulation and demodulation are performed in the baseband DSP. In addition, the acquired knowledge proves useful for the practical task of evaluating the Error Vector Magnitude (EVM) of LTE / LTE-A vectors.

This extensive study has led to the MATLAB implementation of a baseband LTE / LTE-A environment with EVM analyzer, which is described in this chapter. The presented implementation is based directly on 3GPP specifications [20, 24]. If compared to commercial softwares like Agilent Signal Studio [25], the proposed system has the benefit of being much more flexible. For example, it is possible to create/demodulate test vectors with arbitrary integer oversampling ratio, whereas Agilent Signal Studio only supports oversampling ratios of 1 or 2. The added flexibility has proven very useful in the context of the larger project to which this thesis is related.

3.1 Modulator details

Figure 3.1 shows a block diagram of the LTE modulator implemented with MATLAB. The function of each block is briefly described below.

QAM generation An input constellation is generated through a random algorithm. This constellation represents the "single carrier" data. The input symbols are divided into groups of the appropriate size, such that each group will be mapped to a single SC-FDMA symbol. Only 16-QAM is considered in this work, but the input constellation could actually be anything (e.g. QPSK or 64-QAM).

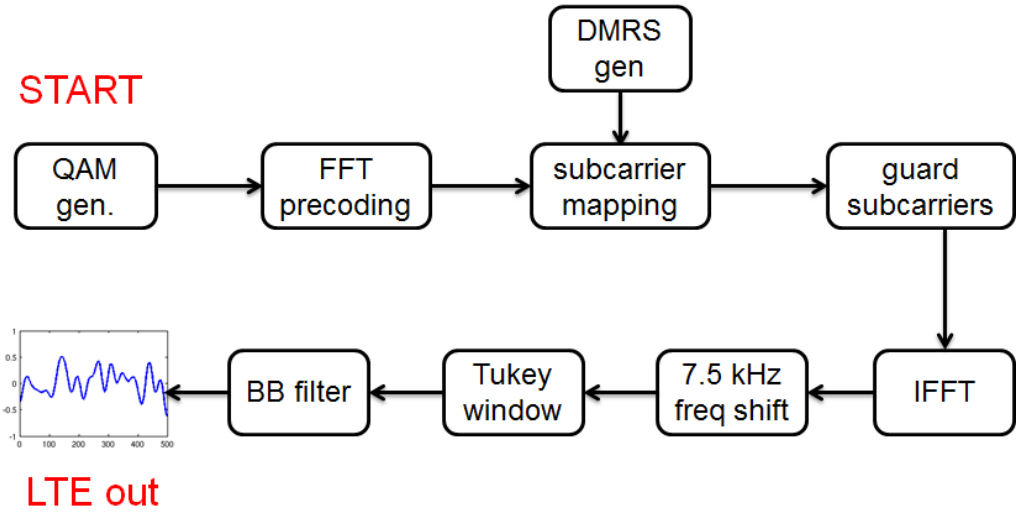

Figure 3.1: Block diagram of the LTE signal generator.

FFT transform precoding The input constellation is precoded by applying the FFT to each group of symbols, in order to obtain a frequency-domain representation of the single carrier.

DMRS generation A Demodulation Reference Signal (DMRS) of the appropriate size is generated according to the algorithm described in LTE specifications, which is based on Zadoff-Chu sequences. The DMRS will be needed later on in the demodulator.

Subcarrier mapping The spectra of input carrier and DMRS are mapped to the appropriate Resource Blocks (RBs), i.e. to the SC-FDMA subcarriers. The DMRS is mapped to the 4^{th} SC-FDMA symbol of each slot, whereas the remaining 6 symbols are used for the input carrier.

Guard subcarrier insertion A number of empty RBs (i.e. null subcarriers) is inserted at the channel edge. This number is directly proportional to the desired oversampling ratio (OSR) of the output signal.

IFFT Once the frequency-domain representation of the output vector is complete, the signal is converted back to time-domain. This is performed by applying the IFFT algorithm to each frequency-domain SC-FDMA symbol.

Frequency shift A 7.5 kHz frequency shift is applied to each of the SC-FDMA symbols. Because 7.5 kHz is half of the subcarrier spacing, this shift has to be applied in the time domain.

Tukey window Since each SC-FDMA symbol is generated independently, there is a discontinuity between two consecutive symbols. This causes high frequency spurious components that are visible as long "tails" in the spectrum of the

output vector. In order to smoothen the discontinuity, windowing can be applied at the symbol boundaries [25]. As will be demonstrated in the following sections, windowing involves a trade-off between far-off noise and EVM. Furthermore, the Cyclic Prefixes (CPs) are automatically created while windowing the SC-FDMA symbols.

Baseband filter Windowing greatly helps against the high frequency spurious components, but it has no effect in the vicinity of the main channel, i.e. it does not improve ACLR. A baseband FIR filter is then applied to the LTE vector, in order to produce a sharp spectrum with almost no degradation on the EVM [25].

In the next subsections, the implementation details of each block are presented, together with some simulation results.

3.1.1 QAM generation

The input symbols must be arranged in a $N_{sc} \times 6N_{slots}$ matrix, where N_{sc} is the number of occupied subcarriers (given by $N_{sc} = 12N_{RB}$), and N_{slots} is the desired number of slots for the output LTE vector (usually $N_{slots} = 20$ to create one entire frame). The factor 6 arises because each slot is composed of 7 SC-FDMA symbols, but one of them is reserved for the DMRS.

A random 16-QAM input matrix d is generated with MATLAB. Each element of the matrix is calculated as

$$d(k,l) = \left(\text{round}\left[4x_I - \frac{1}{2}\right] - \frac{3}{2}\right) + j \cdot \left(\text{round}\left[4x_Q - \frac{1}{2}\right] - \frac{3}{2}\right) \tag{3.1}$$

$$k = 0, \ldots, N_{sc} - 1$$

$$l = 0, \ldots, 6N_{slots} - 1,$$

where x_I and x_Q are random variables with uniform distribution on the open interval $(0, 1)$, and round$[x]$ is the nearest integer to x.

Note that, with such an arrangement of the QAM symbols, each column of d corresponds to one SC-FDMA symbol.

3.1.2 Transform precoding

Transform precoding is used to "spread" the spectrum of the single input carrier over N_{sc} different subcarriers. It is performed by applying the FFT to each column of the matrix d, according to

$$\tilde{y}(k,l) = \sum_{i=0}^{N_{sc}-1} d(i,l) \cdot e^{-j\frac{2\pi ik}{N_{sc}}}, \qquad l = 0, \ldots, 6N_{slots} - 1. \tag{3.2}$$

The result is a matrix $\tilde{y}$ (with the same size as d) containing the complex-valued spectra of each group of N_{sc} QAM symbols in each column.

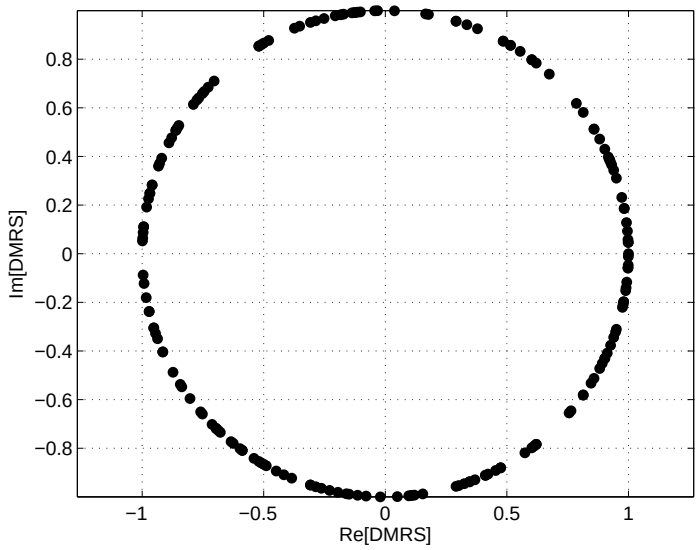

Figure 3.2: The DMRS on the first slot of a 15 RB (3 MHz) LTE vector, generated in MATLAB by the algorithm described in Appendix A.

After that, matrix $\tilde{y}$ is normalized as

$$y = \frac{\tilde{y}}{k_{\tilde{y}}} \tag{3.3}$$

where $k_{\tilde{y}}$ is a scalar normalization factor such that the mean-square of all elements in matrix y equals 1.

3.1.3 DMRS generation

The Demodulation Reference Signal (DMRS) consists of a set of SC-FDMA symbols (one for each slot), where all of the N_{sc} subcarriers have:

- unity magnitude;
- a pseudorandom phase shift.

The generation of this phase shift is based on Zadoff-Chu sequences. The procedure is described in details in Appendix A. It returns a $N_{sc} \times N_{slots}$ matrix r, whose columns contain the complex amplitudes of the N_{sc} subcarriers for each DMRS symbol.

Figure 3.2 shows an example DMRS spectrum plotted on the complex plane, where each point represents a single subcarrier. It can be seen that the complex amplitudes are disposed randomly on the unit circle.

3.1.4 Subcarrier mapping

In the simplest case where uplink frequency-hopping is disabled, subcarrier mapping involves the insertion of the DMRS symbols in the 4^{th} position of each slot. This means that a $N_{sc} \times 7N_{slots}$ matrix z must be created, where

- $z(k, 7n_s + i) = y(k, 6n_s + i), \qquad i = 0,\ 1,\ 2;$
- $z(k, 7n_s + 3) = r(k, n_s);$
- $z(k, 7n_s + i) = y(k, 6n_s + i - 1), \qquad i = 4,\ 5,\ 6,$

for $k = 0,\ \ldots,\ N_{sc} - 1$, and $n_s = 0,\ \ldots,\ N_{slots} - 1$.

3.1.5 Guard subcarrier insertion

The matrix z must be extended to a new $N_{FFT} \times 7N_{slots}$ matrix a, by adding $N_{FFT} - N_{sc}$ zeros at the end of each column of z:

- $a(k, l) = z(k, l), \qquad k = 0,\ \ldots,\ N_{sc} - 1;$
- $a(k, l) = 0, \qquad k = N_{sc},\ \ldots,\ N_{FFT} - 1,$

for $l = 0,\ \ldots,\ 7N_{slots} - 1$.

The number of FFT points is given by $N_{FFT} = N_{FFT,0} \cdot OSR$, where the nominal FFT size $N_{FFT,0}$ is given in Table 2.1 for each channel bandwidth.

3.1.6 SC-FDMA baseband signal generation

Each column of the matrix a is now ready to be converted back to time-domain. According to LTE specifications, the baseband signal in SC-FDMA symbol l is time-continuous, and it is created by taking the Fourier series of the discrete spectrum contained in the l-th column of a:

$$s_l(t) = \sum_{k=-N_{sc}/2}^{N_{sc}/2-1} a\left(k + \frac{N_{sc}}{2}, l\right) \cdot e^{j2\pi\left(k+\frac{1}{2}\right)\Delta f(t-T_{CP})} \tag{3.4}$$

$$0 \leqslant t < T_{FFT} + T_{CP},$$

where T_{FFT} and T_{CP} are the US and CP durations respectively, and $\Delta f = 15\,\text{kHz}$ is the subcarrier spacing.

Given that $T_{FFT} = 1/\Delta f$, it is easy to prove that

$$s_l(t) = -s_l(t + T_{FFT}), \qquad 0 \leqslant t < T_{CP}. \tag{3.5}$$

That is, the leftmost part of $s_l(t)$ is the negative copy of the rightmost part, i.e. the Cyclic Prefix of the SC-FDMA symbol. The fact that the CP is the *negative* copy comes from the 1/2 factor in the exponent of (3.4), which corresponds to a $\Delta f/2 =$

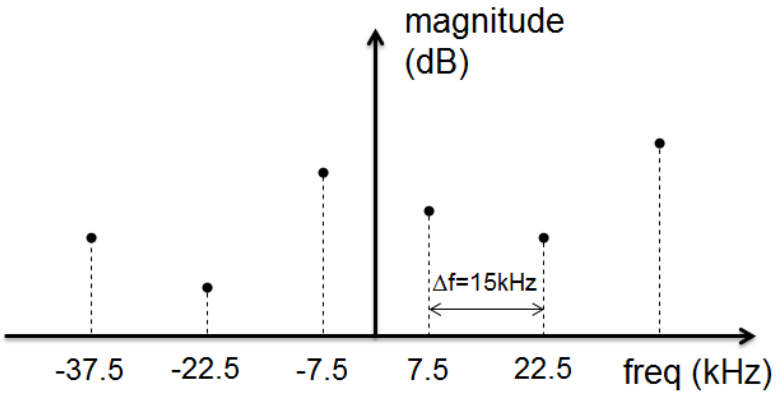

(a) *Magnitude spectrum of the subcarriers*

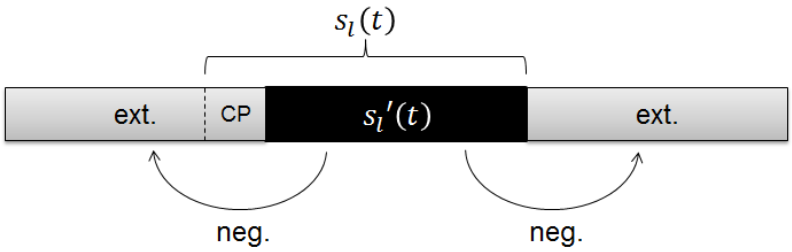

(b) *Extension of Useful Symbol*

Figure 3.3: Consequences of the 7.5 kHz frequency shift in the frequency- and time-domain.

7.5 kHz frequency shift of the subcarriers.[1] In other words, the subcarrier frequencies are odd multiples of 7.5 kHz, as shown in Figure 3.3a. Therefore, the output of the Fourier series is a periodic signal, with period $2/\Delta f = 2T_{FFT}$. However, because there are only odd harmonics, the signal presents odd symmetry with respect to its half period T_{FFT}, thus validating (3.5).

Hence, an SC-FDMA symbol can be created by generating the Useful Symbol $s_l'(t) = s_l(t + T_{CP})$, with $0 \leqslant t < T_{FFT}$. Possible *extensions* (like the CP) are then simply created as the negative copies of $s_l'(t)$, as can be seen in Figure 3.3b. This observation eliminates redundancy in the baseband DSP circuitry, thus simplifying the transmitter.

In practice, each US is created as a sampled version of $s_l'(t)$:

$$s_l'(nT_s) = \sum_{k=-N_{sc}/2}^{N_{sc}/2-1} a\left(k + \frac{N_{sc}}{2}, l\right) \cdot e^{j2\pi\left(k+\frac{1}{2}\right)\Delta f n T s}, \tag{3.6}$$

where the sampling period is $T_s = T_{FFT}/N_{FFT}$, and $n = 0, \ldots, N_{FFT} - 1$. It can

[1] The 7.5 kHz frequency shift has been introduced in LTE uplink, in order to better support the direct-conversion transmitter and receiver architectures, which can introduce significant DC subcarrier distortion [13, 26].

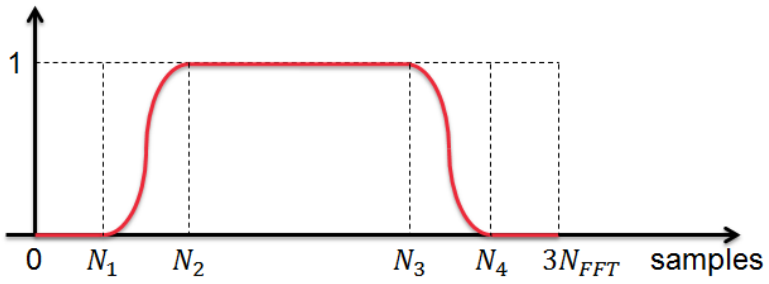

Figure 3.4: The Tukey window.

be shown that (3.6) is equivalent to

$$s'_l(nT_s) = \left[\sum_{k=0}^{N_{FFT}-1} a(k,l) \cdot e^{j\frac{2\pi kn}{N_{FFT}}} \right] e^{j\frac{\pi n(1-N_{sc})}{N_{FFT}}}. \tag{3.7}$$

This is the SC-FDMA baseband signal generation equation that was implemented in MATLAB.

Equation (3.7) has the following properties:

- The part in square brackets is the N_{FFT}-point IFFT of the l-th column of matrix a, scaled up by a factor N_{FFT}.
- The remaining exponential factor represents a frequency shift, including the 7.5 kHz offset. This shift has to be performed in the time-domain.

Equation (3.7) also shows explicitly the aforementioned simplification in the baseband DSP circuitry: the number of IFFT points is halved (from $2N_{FFT}$ that would be needed to generate the whole period $2T_{FFT}$, to N_{FFT}) at the expense of an extra multiplication by an exponential factor.

The result of the above derivation is a $N_{FFT} \times 7N_{slots}$ matrix s', where each column is the "frequency-shifted IFFT" of the corresponding column in matrix a. The output LTE vector could now be created by just generating the sampled versions of signals $s_l(t)$, $l = 0, \ldots, 7N_{slots}-1$, from the columns of s', and cascading them into a single output vector. However, as already stated, this would result in discontinuities between subsequent SC-FDMA symbols. The windowing strategy described in the next section effectively reduces the high frequency spurious components generated by these discontinuities.

3.1.7 Tukey window

The Tukey window [27], shown in Figure 3.4, has been chosen for the LTE signal generator because of its flatness around the window center, as well as its smooth transitions to zero at the window edges through *raised-cosine* lobes. The sampled

Tukey window is defined for $n = 0, \ldots, 3N_{FFT} - 1$ as

$$f_{win}(n) = \begin{cases} 0, & n = 0, \ldots, N_1 - 1, \\ 0.5 \cdot \left(1 - \cos \frac{\pi(n-N_1+1)}{L_r}\right), & n = N_1, \ldots, N_2 - 1, \\ 1, & n = N_2, \ldots, N_3 - 1, \\ 0.5 \cdot \left(1 + \cos \frac{\pi(n-N_3+1)}{L_r}\right), & n = N_3, \ldots, N_4 - 1, \\ 0, & n = N_4, \ldots, 3N_{FFT} - 1, \end{cases} \tag{3.8}$$

where L_r is the *symbol rolloff length* which determines the length (in samples) of the transition from 0 to 1 and vice versa, and the points N_i are given by

$$\begin{aligned} N_1 &= N_{FFT} - N_{CP} - L_r/2, \\ N_2 &= N_{FFT} - N_{CP} + L_r/2, \\ N_3 &= 2N_{FFT} - L_r/2, \\ N_4 &= 2N_{FFT} + L_r/2, \end{aligned} \tag{3.9}$$

where N_{CP} is the CP length (in samples). The distance between the middle points of the two raised-cosine lobes is exactly $N_{FFT} + N_{CP}$ samples, that is, the window accounts for both CP and US. Furthermore, N_{CP} depends on whether the window must be applied to the first symbol of one slot, or to the remaining six symbols. The exact values are given in Table 2.1.

Prior to windowing, the time-domain USs must be extended according to the procedure described in the previous section:

$$s'_{l,ext}(nT_s) = \begin{cases} -s'_l(nT_s), & n = 0, \ldots, N_{FFT} - 1, \\ s'_l\big((n - N_{FFT})T_s\big), & n = N_{FFT}, \ldots, 2N_{FFT} - 1, \\ -s'_l\big((n - 2N_{FFT})T_s\big), & n = 2N_{FFT}, \ldots, 3N_{FFT} - 1, \end{cases} \tag{3.10}$$

for $l = 0, \ldots, 7N_{slots} - 1$.

After that, actual windowing is performed for each extended US according to

$$s'_{l,win}(nT_s) = s'_{l,ext}(nT_s) \cdot f_{win}(n), \tag{3.11}$$

for $n = 0, \ldots, 3N_{FFT} - 1$, and $l = 0, \ldots, 7N_{slots} - 1$.

Last, all the windowed symbols must be aligned and summed up to the output LTE vector. Alignment itself is already a quite complex operation, and it is further complicated by the different CP lengths between symbol 0 and symbols 1 to 6 within each slot. To give insight to the procedure, alignment is illustrated graphically in Figure 3.5.

It is worth mentioning that the beginning of the first SC-FDMA symbol ($l = 0$) is aligned to the end of the last one ($l = 7N_{slots} - 1$), in a "circular" fashion. In other words, if $s_{LTE}(nT_s)$ is the output LTE vector after windowing, then the transition from the rightmost part of $s_{LTE}(nT_s)$ to its leftmost part is continuous. This means that the output LTE vector can be extended as the periodic repetition of $s_{LTE}(nT_s)$, without introducing discontinuities.

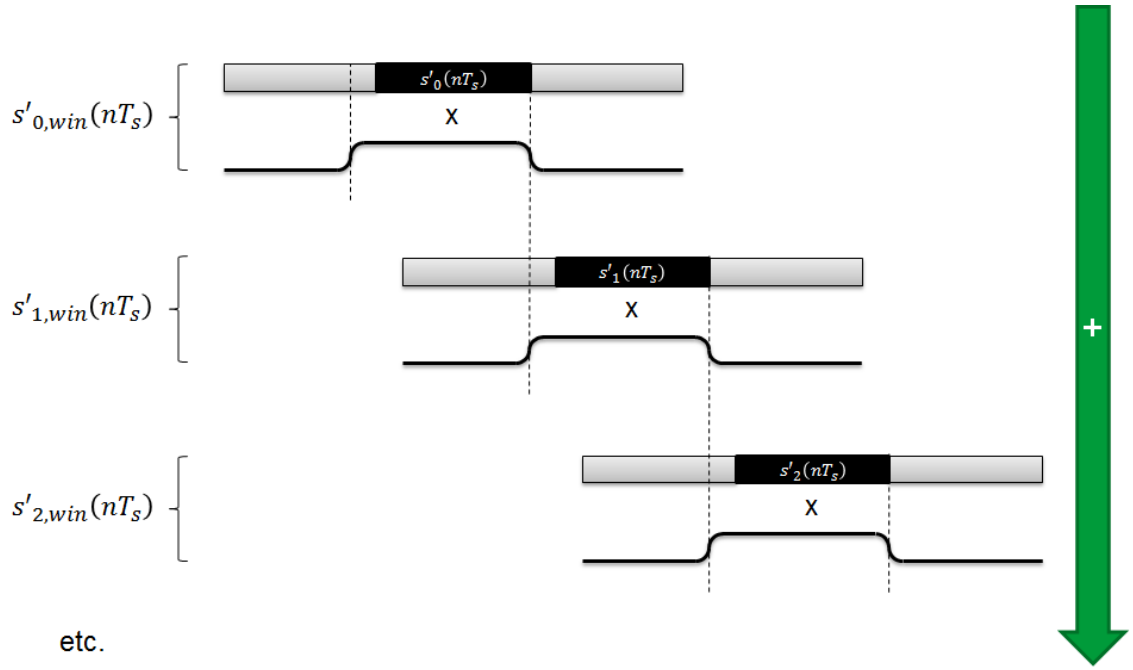

Figure 3.5: Extension, windowing, and alignment of the first three SC-FDMA symbols of an LTE vector. Extensions are shown in light gray. Note the alignment between the end of each symbol and the start of the CP of the next one.

Figures 3.6a and 3.6b illustrate the effect of windowing in the time- and frequency-domain respectively. In the time-domain, windowing consists of tapering smoothly to zero the extremities of two adjacent SC-FDMA symbols before they are summed up to the output vector, such that the discontinuity is removed. The benefits can be readily seen in the frequency-domain, for windows with different symbol rolloff lengths L_r. The far-off noise floor can decrease by more than 100 dB, and the improvement is higher as L_r becomes larger. However, as will be shown in section 3.3, the proper choice of L_r involves a trade-off between far-off noise and EVM performance.

3.1.8 Baseband filter

The last stage of the LTE vector generator consists of a baseband FIR filter. This filter is necessary because the ACLR performance of the windowed LTE vector $s_{LTE}(nT_s)$ is quite poor if compared to LTE specifications, and it does not leave enough margin for the various RF front-end impairments.

The baseband FIR filter is designed using MATLAB's built-in filter design routines, with the following parameters:[2]

- Design method: *FIR equiripple*

[2]These parameters have been chosen in order to make the frequency-domain characteristics of the own generated LTE signals as similar as possible to those generated with Agilent Signal Studio.

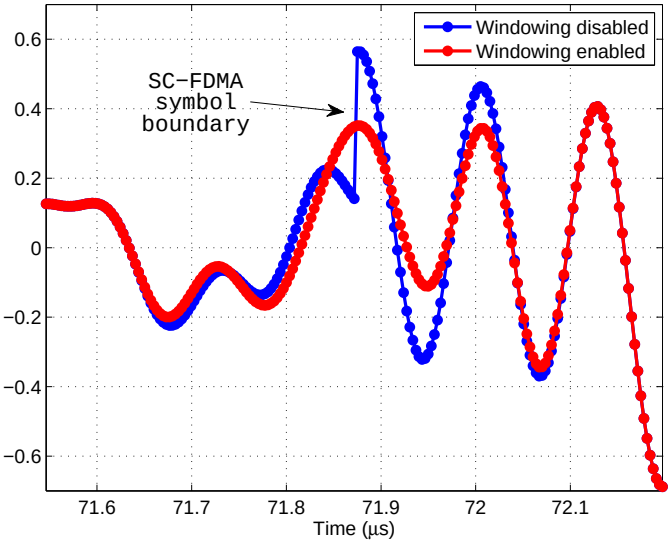

(a) *Effects in the time-domain (only real part shown)*

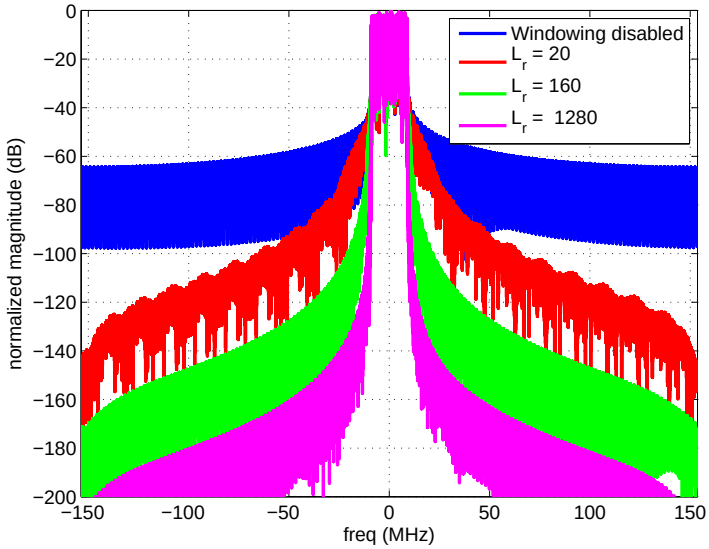

(b) *Effects in the frequency-domain for different values of* L_r

Figure 3.6: Effects of windowing on a 100 RB (20 MHz) LTE vector with $OSR = 10$.

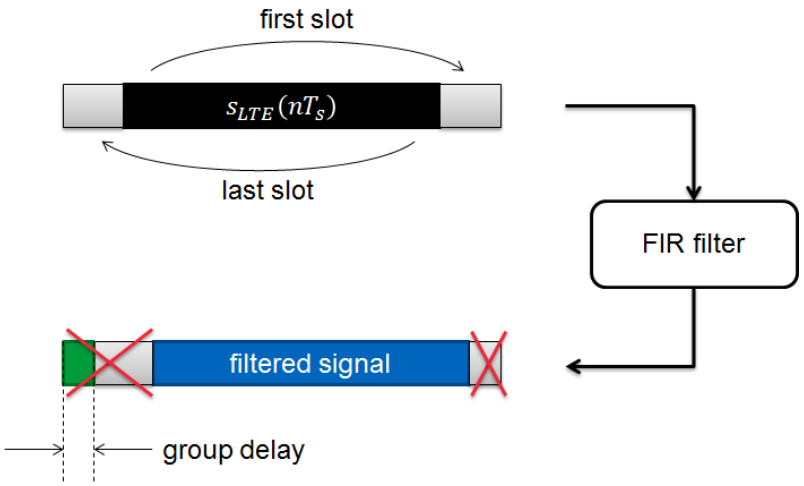

Figure 3.7: Filtering of the windowed LTE vector.

- Filter order: $N = 70 \cdot OSR$
- Transition bandwith center frequency: $f_c = BW/2$
- Transition bandwith width: $B_c = 1.2 \cdot BW/20$

where OSR is the oversampling ratio, and BW the channel bandwidth. All of the specified frequencies must be normalized with respect to the sampling frequency $F_s = F_{s,0} \cdot OSR$ (see Table 2.1).

The details of the filtering process are shown graphically in Figure 3.7. Thanks to the adopted windowing strategy, the entire process corresponds to the "circular convolution" of $s_{LTE}(nT_s)$ with the filter's impulse response. Therefore, the filtered LTE vector is also "circularly continuous" as the input.

Figure 3.8a shows a spectrum comparison between the channel edges of the same LTE vector, generated without and with BB filter. The measured $ACLR_1$ (for the first adjacent WCDMA channel) is 56 and 110 dB respectively. This improvement leaves a much higher margin for the subsequent TX blocks. Figure 3.8b shows a comparison between the spectra of LTE vectors generated with Agilent Signal Studio for 3GPP LTE FDD [25], and with the LTE signal generator implemented in MATLAB. The own generated LTE vector looks to have a slightly sharper power droop at the channel edges (not much visible in Figure 3.8b), as well as lower spurious power at higher frequencies.

3.1.9 LTE-A signal generation

The generation of an LTE-A vector does not require new concepts with respect to what has been discussed so far. The steps for LTE-A signal generation are listed below.

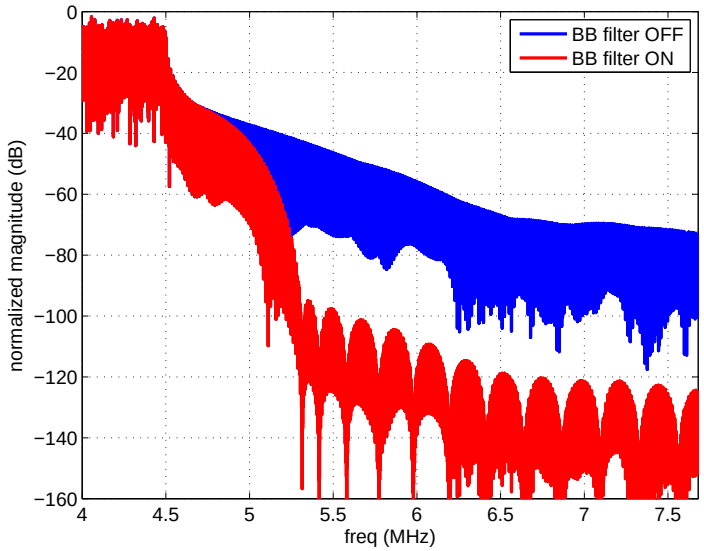

(a) *Comparison between the channel edges of two 50 RB (10 MHz) LTE vectors, generated from the same 16-QAM constellation, with and without using the BB filter*

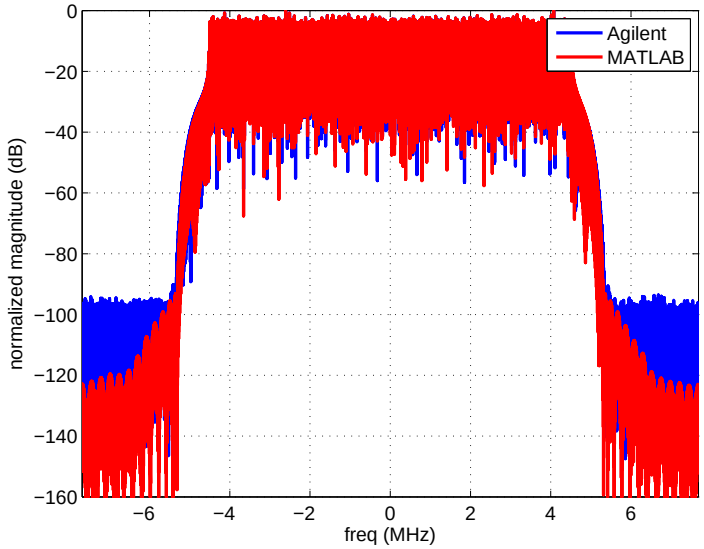

(b) *Comparison between two 50 RB (10 MHz) LTE vectors, created with Agilent Signal Studio and with the implemented MATLAB generator, starting from the same 16-QAM constellation*

Figure 3.8: Spectrum quality of the filtered LTE vectors.

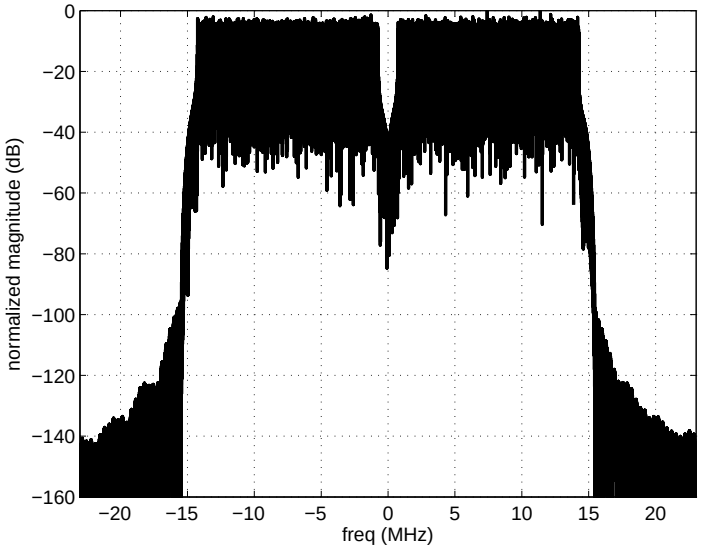

Figure 3.9: Spectrum of a 75+75 RB (15+15 MHz) LTE-A vector created with MATLAB.

1. Create the two Carrier Components (CCs) as two independent LTE vectors $s_1(nT_s)$ and $s_2(nT_s)$, by following the procedure described in the previous sections. The two CCs must have the same BW and an oversampling ratio of at least 2.

2. Apply two opposite frequency offsets $\pm f_{off} = \pm BW/2$ to the LTE vectors:

$$\begin{aligned} s_{low}(nT_s) &= s_1(nT_s) \cdot e^{-j2\pi f_{off} nT_s}, \\ s_{high}(nT_s) &= s_2(nT_s) \cdot e^{+j2\pi f_{off} nT_s}. \end{aligned} \tag{3.12}$$

3. Sum the resulting signals up to a single output LTE-A vector:

$$s_{LTE-A}(nT_s) = s_{low}(nT_s) + s_{high}(nT_s). \tag{3.13}$$

Figure 3.9 shows the spectrum of an LTE-A vector created with the implemented MATLAB generator. Note how the two CCs can be clearly distinguished from each other.

3.2 Demodulator details

Figure 3.10 shows a block diagram of the LTE demodulator implemented with MATLAB. The demodulator performs pretty much the inverse of the operations that were applied by the signal generator, with just a few differences [20, 24]. The function of each block is briefly described below.

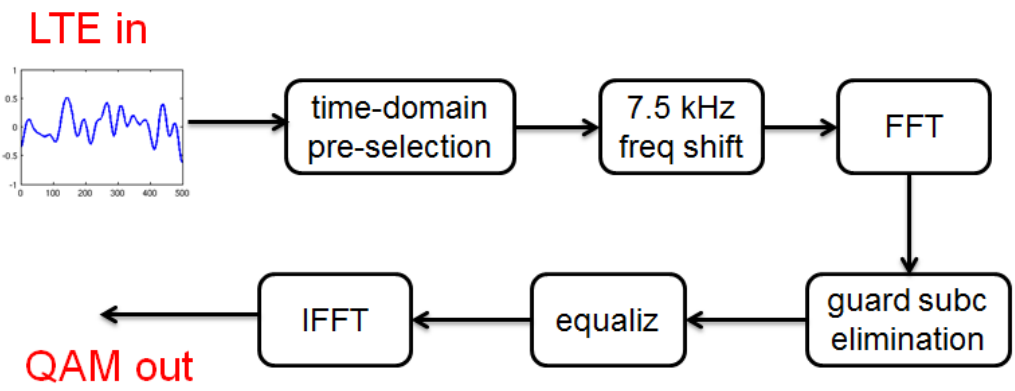

Figure 3.10: Block diagram of the LTE signal demodulator.

Time-domain pre-selection The first block selects the fraction of each time-domain SC-FDMA symbol that is useful to reconstruct the original QAM constellation. This can also include part of the CP.

Frequency shift The 7.5 kHz frequency shift that was applied by the modulator must be compensated by a time-domain frequency shifter.

FFT The FFT algorithm is used to calculate the complex amplitudes of the subcarriers, in order to obtain frequency-domain representations of each SC-FDMA symbol.

Guard subcarrier elimination The null subcarriers at the channel edge are discarded.

Equalization Frequency-domain equalization [13] is performed on the complex subcarrier amplitudes, in order to compensate for the linear distortion mechanisms in the TX chain as well as for the time shift applied on purpose by the pre-selection block.

IFFT The frequency-equalized subcarriers are converted back to time-domain through IFFT. This yields the demodulated QAM constellation.

In the LTE-A case, the vector must be first divided into the two Carrier Components, before each of them can be fed to the demodulator of Figure 3.10 separately. This is simply done by applying two opposite frequency offsets to the input signal, followed by filtering out of the unwanted CC.

Because of the similarities between modulator and demodulator, only the mathematical details of those blocks that do not have a counterpart in the modulator are described in the next subsections. Simulation results are also presented.

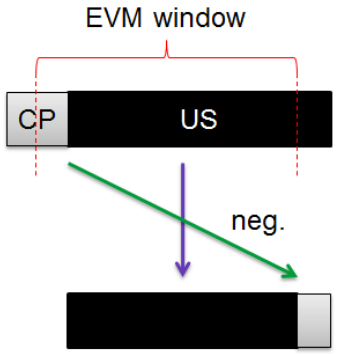

Figure 3.11: Time-domain pre-selection process.

3.2.1 Time-domain pre-selection

Because of the Cyclic Prefix in front of every SC-FDMA symbol, there is redundancy in the information carried by an LTE vector. Each symbol consists of $N_{CP} + N_{FFT}$ samples, but only N_{FFT} points are sufficient to recover the modulated data. However, the demodulator does not necessarily have to discard exactly the first N_{CP} samples. For example, the first $N_{CP}/2$ points could be left out, while the negative copies of the subsequent $N_{CP}/2$ points are used to replace the samples at the end of the SC-FDMA symbol.

This concept is illustrated graphically in Figure 3.11. The group of N_{FFT} samples involved in the demodulation process is called "EVM window". The position of the window within the SC-FDMA symbol can be freely chosen, because the information carried by the N_{FFT} samples does not change. However, some positions should be preferred. For example, if the EVM window is too close to one of the symbol ends, most likely some amount of Inter-Symbol Interference (ISI) will occur, because of the time-domain averaging effect introduced around the symbol boundaries by the windowing. Therefore, for a good demodulation result, it is good to place the EVM window as close as possible to the SC-FDMA symbol center.

The same concept can be also expressed mathematically. The US baseband signal generation equation is

$$s'_l(nT_s) = \sum_{k=-N_{sc}/2}^{N_{sc}/2-1} a\left(k + \frac{N_{sc}}{2}, l\right) \cdot e^{j2\pi\left(k+\frac{1}{2}\right)\Delta f n T s}. \tag{3.14}$$

If we apply a time shift of n_0 samples to (3.14), we obtain

$$s'_l\big((n-n_0)T_s\big) = \sum_{k=-N_{sc}/2}^{N_{sc}/2-1} \left[a\left(k + \frac{N_{sc}}{2}, l\right) \cdot e^{j\vartheta(k)}\right] \cdot e^{j2\pi\left(k+\frac{1}{2}\right)\Delta f n T s}, \tag{3.15}$$

with the linear phase term $\vartheta(k)$ defined as

$$\vartheta(k) = -2\pi\left(k + \frac{1}{2}\right)\Delta f n_0 T s. \tag{3.16}$$

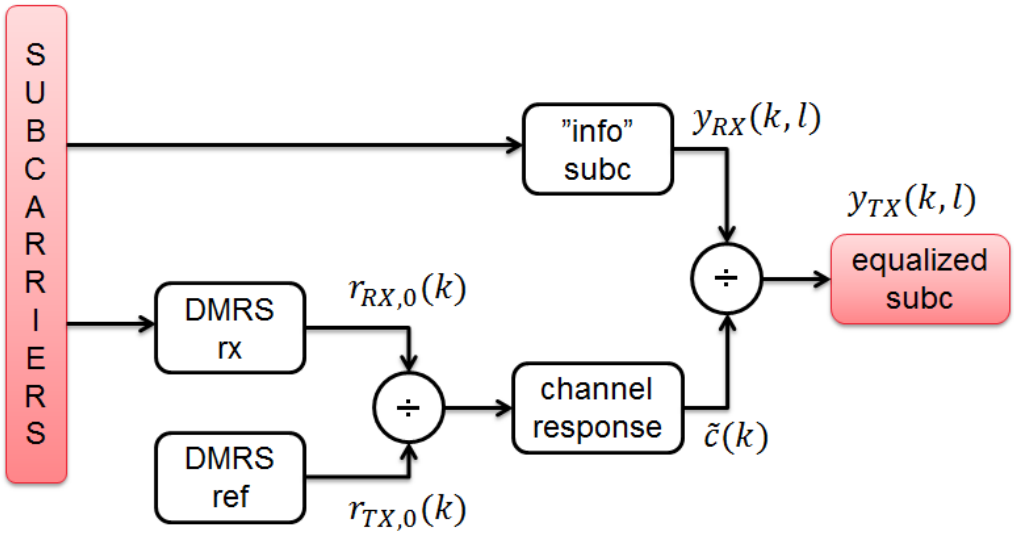

Figure 3.12: Block diagram of the frequency-domain equalizer.

This means that, if the EVM window is shifted backwards by n_0 samples, the subcarriers (whose amplitudes are obtained from $s'_l\big((n-n_0)T_s\big)$ by inverting (3.14)) undergo a linear phase shift that is given by (3.16), which can be compensated if n_0 is known. The condition $0 \leqslant n_0 \leqslant N_{CP}$ must be fulfilled, otherwise the EVM window happens to include part of the adjacent SC-FDMA symbol, leading to ISI.

In the implemented MATLAB model of the demodulator, the compensation of the subcarrier phase shift is actually performed with the frequency-domain equalizer described in the next subsection. This allows to handle the cases where n_0 is unknown.

3.2.2 Equalization

A block diagram of the frequency-domain equalizer is shown in Figure 3.12. The operation principle is based on DMRS: since the reference symbols are known, they can be used to estimate the channel response. The term "channel response" is used here to indicate a number of typical linear distortion mechanisms of the TX chain (e.g. filters, zero-order hold), as well as the time shift applied by the pre-selection block (i.e. linear phase shift in the frequency-domain). The TX and RX blocks are assumed to be directly connected to each other, as when testing only the TX block. In a real operation, the frequency-domain equalizer must be able to compensate for the actual radio channel response.

The frequency-domain equalization mechanism works as follows. The DMRS of the first slot $r_{RX,0}(k)$ is selected for channel response estimation. This choice is justified by the fact that our system is time-invariant. It is also assumed that the time shift n_0 applied by the pre-selection block is constant for all SC-FDMA symbols. In a DMRS, all of the N_{sc} subcarriers should have unity magnitude and a pseudorandom phase shift (see Figure 3.2). However, due to the linear distortion

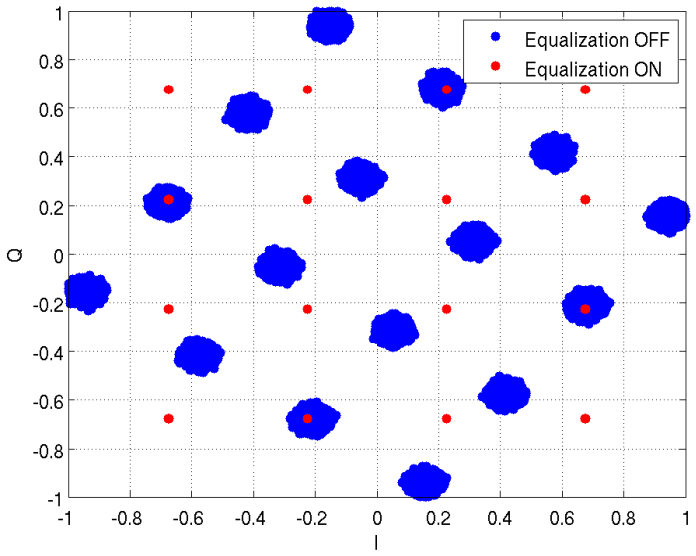

Figure 3.13: Comparison between the 16-QAM constellations demodulated from the same 100+100 RB (20+20 MHz) LTE-A vector, generated with Agilent Signal Studio, with and without equalization.

mechanisms, both magnitude and phase of the received subcarriers may have been altered. The channel response can thus be estimated in the frequency-domain, as

$$\tilde{c}(k) = \frac{r_{RX,0}(k)}{r_{TX,0}(k)}, \qquad k = 0, \ldots, N_{sc} - 1, \tag{3.17}$$

where $r_{TX,0}(k)$ is the "ideal" DMRS of the first slot, that can be generated in the demodulator by following exactly the same procedure that was described for the modulator (Appendix A).

The estimated channel response $\tilde{c}(k)$ is used to normalize the magnitude and phase of the received subcarriers. If y_{RX} is the $N_{sc} \times 6N_{slots}$ matrix containing the received subcarrier amplitudes (one column for each SC-FDMA symbol, excluding DMRS), then the matrix y_{TX}, which is an estimation of y defined in (3.3), is calculated as

$$y_{TX}(k,l) = \frac{y_{RX}(k,l)}{\tilde{c}(k)}, \tag{3.18}$$
$$k = 0, \ldots, N_{sc} - 1,$$
$$l = 0, \ldots, 6N_{slots} - 1.$$

Equalization is absolutely necessary when demodulating LTE-A vectors. Figure 3.13 compares the 16-QAM constellations demodulated from the same LTE-A vector (generated with Agilent Signal Studio), with and without equalization. The unequalized constellation appears to be "rotated" (i.e. phase-shifted) and its magnitude is distorted by the non-ideal channel response. The equalized constellation looks almost ideal.

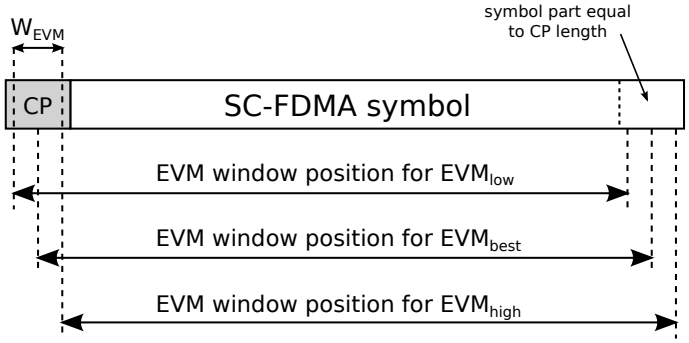

Figure 3.14: Position of the EVM windows used to measure EVM_{low}, EVM_{high}, and EVM_{best}. The range W_{EVM} is centered at the middle of the CP (for symbols 1-6 within each slot). The position of each window determines the time shift n_0 to be applied to the LTE vector during demodulation.

3.3 EVM measurement

The concepts presented in Sections 3.1 and 3.2 can be used to calculate the EVM of LTE / LTE-A vectors. The EVM measurement procedure reported here is based on the description that can be found in LTE specifications [20].

The optimum SC-FDMA demodulation result is obtained when the EVM window is placed close to the symbol center, because of the ISI introduced by time-domain windowing and filtering in the baseband modulator. However, the EVM limit reported in Table 2.4 has to be met when the EVM window is moved quite close to the symbol edges. This ensures enough margin for signal degradation introduced by the transmitter and the radio channel.[3] Hence, a good baseband LTE modulator has to reduce the out-of-band emissions without introducing excessive distortion at the SC-FDMA symbols boundaries, meaning that there is a trade-off between RF performance (in terms of ACLR and noise floor) and modulation quality (in terms of EVM).

The locations of EVM windows that must yield a good demodulation result are given by W_{EVM} in Table 2.1, for each LTE channel bandwidth. This quantity defines the minimum and maximum time shifts to be applied to the vector under test during demodulation, according to

$$n_{0,min} = \frac{N_{CP} - W_{EVM}}{2}, \tag{3.19a}$$

$$n_{0,max} = \frac{N_{CP} + W_{EVM}}{2}, \tag{3.19b}$$

where N_{CP} is the CP length for symbols 1-6 (see Table 2.1). Figure 3.14 illustrates this concept. The EVM is worst when the window is placed either at the lower edge

[3] As stated in Section 2.1, the CP is introduced to eliminate the ISI caused by a multipath radio channel. However, this technique remains effective only if the baseband modulator does not introduce excessive signal degradation at the SC-FDMA symbol boundaries.

($n_0 = n_{0,max}$) or upper edge ($n_0 = n_{0,min}$) of the range. Therefore, it makes sense to calculate the EVM only at such extremities, thus yielding the two worst-case measurements EVM_{low} and EVM_{high}. It is also possible to calculate EVM_{best}, i.e. with the EVM window placed at the center of the SC-FDMA symbol ($n_0 = N_{CP}/2$). This reveals how much degradation is actually introduced by the RF front-end itself, without accounting for the quality of the baseband modulator.

The EVM measurement procedure goes as follows.

1. Downconvert, filter and (optionally) downsample the RF signal measured at the I-Q modulator output, in order to recover the baseband vector.[4]

2. Demodulate the LTE vector (as explained in Section 3.2) with the EVM window placed at the lowest, middle, and highest points of the range defined by W_{EVM}. This yields three sets of QAM symbols.

3. Divide each set into groups of $6N_{sc}$ QAM symbols, such that each group contains only the data from one slot.

4. Apply the basic EVM calculation formula (2.11) to each group, in order to obtain the values of $EVM_{low}(k)$, $EVM_{high}(k)$, and $EVM_{best}(k)$ for each slot k.

5. The overall EVM values are given by computing the root-mean-square among all slot measurements, according to

$$EVM_i = \sqrt{\frac{1}{N_{slots}} \sum_{k=1}^{N_{slots}} EVM_i(k)^2}, \tag{3.20}$$

   where $i = low$, $high$ or $best$.

6. Finally, the worst EVM value is selected as the final measurement result:

$$EVM = max\big(EVM_{low}, EVM_{high}\big). \tag{3.21}$$

Figure 3.15 shows an example of how the EVM degrades, as the symbol rolloff length L_r (defined in Section 3.1.7) increases. By comparing this graph with Figure 3.6b, the trade-off between out-of-band emissions and EVM becomes clear. When the raised-cosine part of the Tukey window is extended, the transition between two consecutive SC-FDMA symbols becomes smoother. However, this comes at the expense of a larger ISI, because the "interference" between the two symbols caused by time-domain averaging extends for a longer time interval. Therefore, L_r must be chosen such that the EVM measured according to the above procedure remains within a predefined bound, leaving enough room for further signal degradation. For example, by applying the arbitrary constraint $EVM \leqslant 1\%$, one gets the symbol rolloff lengths reported in Table 3.1.

[4]This is done in MATLAB through an ideal direct-conversion receiver, followed by a cascade of decimation filters. The details of such "ideal receiver" are not discussed in this thesis.

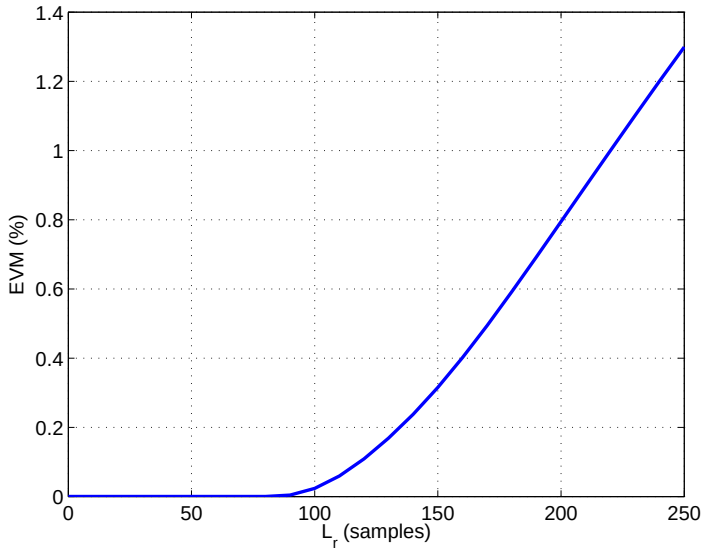

Figure 3.15: EVM versus symbol rolloff length, for a 100 RB (20 MHz) LTE vector with $OSR = 10$. The EVM is calculated according to (3.21), over a length of 4 slots.

BW (MHz)	L_r
1.4	6
3	8
5	6
10	10
15	10
20	16

Table 3.1: Maximum symbol rolloff lengths for each LTE channel bandwidth, fulfilling the arbitrary constraint $EVM \leqslant 1\%$. Values are given in samples, by assuming the base sampling rate for each BW.

Chapter 4

Analysis and modeling of the DDRM

This chapter focuses on the theoretical analysis of the system-level behavior of DDRM and RF-DAC. First, a couple of well-known issues in digital signal processing, such as quantization and zero-order hold, are reviewed. These mechanisms affect even the performance of an ideal DDRM, and are very typical of all-digital transmitters.

After that, all the non-idealities that could arise from a CMOS implementation of the RF-DAC are discussed. Most of the classical theory about current-steering DACs, including current source mismatches, clock jitter, and nonlinear output impedance, can be straightforwardly applied to the RF-DAC. On the other hand, the effects of timing error in the distributed upconversion have not been analyzed in published literature. Therefore, a new analytical model of the nonlinearity caused by this phenomenon is developed, which is one of the most important results achieved by this thesis.

4.1 MATLAB model

A block diagram of the MATLAB model of the DDRM is shown in Figure 4.1. The model was created resembling partially the work presented in [3].

The model works as follows. For each circuit branch (I and Q), the input bits are first partitioned into Most Significant Bits (MSBs) and Least Significant Bits (LSBs), as described in Section 2.3.2. The MSBs are processed by a binary-to-thermometer decoder, whereas the LSBs remain binary-coded. The length of the two segments is parametrizable. After segmentation, the baseband signals undergo a discrete-time Zero-Order Hold (ZOH), which adapts their sampling rate to that of the Local Oscillator.[1] The main components of the DDRM are the two RF-DACs, modeled as arrays of unit conversion cells. Each unit cell performs a logical XNOR between LO and data signals. The cell outputs are set by the biasing blocks,

[1] Continuous-time signals can be only represented in MATLAB as discrete-time signals with a sufficiently high sampling rate. This issue is discussed in details in Section 4.2.2.

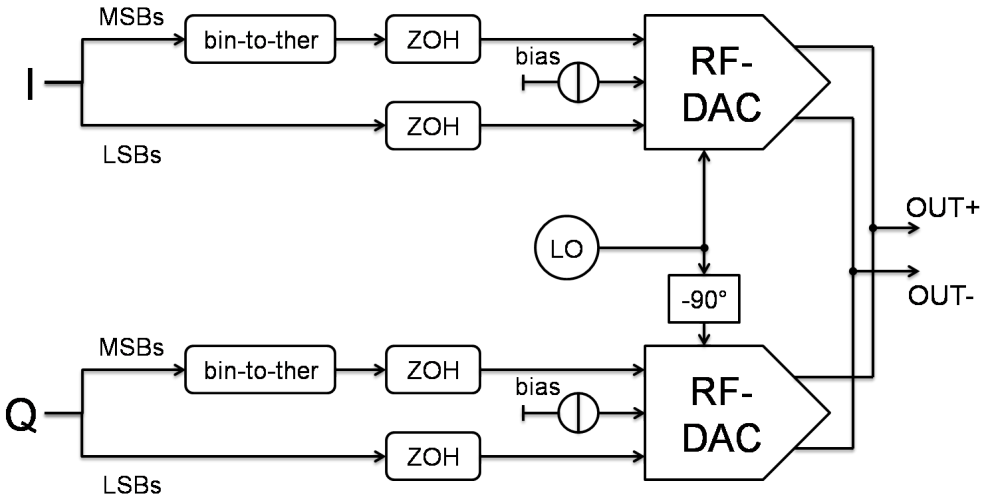

Figure 4.1: Block diagram of the MATLAB model of the RF-DAC.

consisting of vectors that contain the values of the current source weights.

A detailed description of the DDRM impairments and how they are modeled is presented in the next sections.

4.2 Digital TX effects

4.2.1 Quantization of the amplitudes

The theory of quantization is widely treated in literature. This section only addresses its main aspects, that are sufficient to quantify the amount of out-of-band noise produced by the ideal DDRM. A deeper treatment of the topic can be found, for example, in [28].

Figure 4.2a shows the transfer curve of a 2-bit uniform quantizer. The *quantization error* is defined as the difference between the quantized signal $x_q(nT_s)$, and the ideal signal $x(nT_s)$, according to

$$e_q(nT_s) = x_q(nT_s) - x(nT_s), \tag{4.1}$$

where $T_s = 1/F_s$ is the sampling period.

In most practical situations, the quantization process can be modeled as linear addition of noise to the ideal signal, as shown in Figure 4.2b. The following assumptions are made about the added noise:

- It is uncorrelated with the ideal signal $x(nT_s)$.
- Its amplitudes (assuming that no overflow occurs) are uniformly distributed within the range $[-\Delta/2, +\Delta/2]$, where Δ is the quantization step (equal to one LSB).

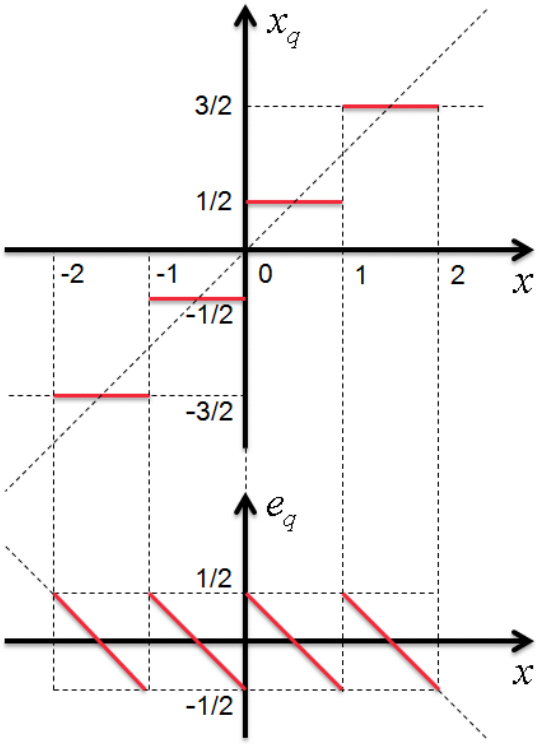

(a) *Transfer curve of a 2-bit quantizer with* $\Delta = 1$, *and corresponding quantization error*

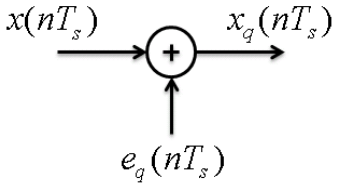

(b) *Linearized quantization error model*

Figure 4.2: Quantization of the amplitudes.

- Its Power Spectral Density (PSD) is flat.

Under these assumptions, it can be demonstrated that the Signal-to-Noise Ratio (SNR), i.e. the ratio of signal power to noise power in the quantized signal, is given by

$$SNR = \left.\frac{P_{signal}}{P_{noise}}\right|_{dB} = 6.02N_{bits} + 10\log_{10}(OSR) + C \qquad \text{[dB]}, \tag{4.2}$$

where

- P_{signal} is the total signal power.
- P_{noise} is the noise power falling within $[-B_s, +B_s]$, where B_s is the signal bandwidth.
- N_{bits} is the binary word length in bits.
- $OSR = F_s/(2B_s)$ is the Oversampling Ratio, indicating how much higher is the sampling frequency F_s with respect to the Nyquist rate $2B_s$.
- C is a constant which depends on the amplitude distribution of the ideal signal, and it can be usually neglected in hand calculations. For a sinusoidal signal, $C = 1.76\,\text{dB}$.

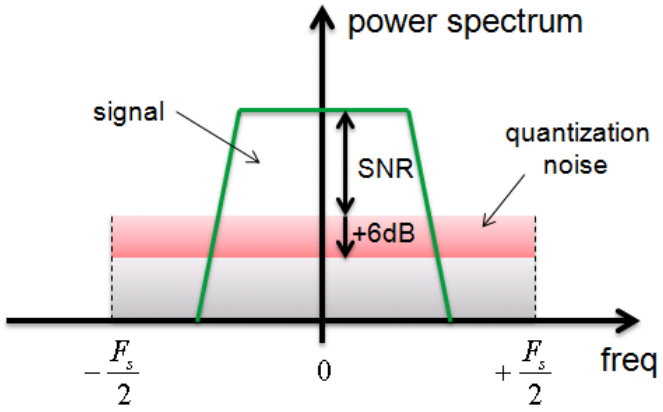

(a) *Word length increment by 1 bit*

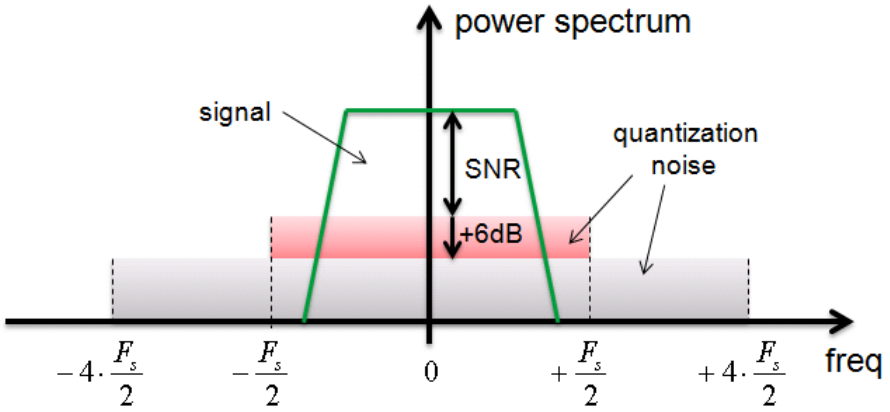

(b) *OSR increment by a factor of 4*

Figure 4.3: Techniques to improve the Signal-to-Noise Ratio. The original and improved quantization noise powers are shown in red and light gray respectively.

The effects of N_{bits} and OSR on the Signal-to-Noise Ratio are illustrated graphically in Figure 4.3. As stated by (4.2), adding one bit to the binary representation leads to an approximately 6 dB improvement in SNR. The same improvement can be also obtained by increasing the OSR by a factor $10^{0.6} = 4$. This happens because, as sampling rate is increased, the total noise power is spread over a wider frequency range, thus decreasing P_{noise}.

4.2.2 Zero-order hold

Signal reconstruction in a conventional DAC is usually performed as Zero-Order Hold (ZOH). In the RF-DAC, this operation is combined together with upconversion. A lot of literature exists about ZOH, for example [29].

Mathematically, the ZOH operation can be seen as a linear time-invariant filter applied to a discrete-time signal $x(n)$. In the time-domain, the continuous-time

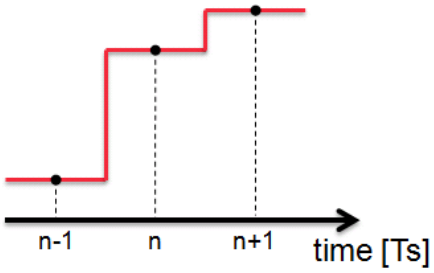

Figure 4.4: Ideal ZOH operation in the time-domain.

output signal $x_{ZOH}(t)$ is given by

$$x_{ZOH}(t) = \sum_{i=-\infty}^{+\infty} x(i) \cdot g(t - iT_s), \tag{4.3}$$

where T_s is the sampling period of $x(n)$, and the filter's impulse response $g(t)$ is the rectangular function

$$g(t) = \text{rect}\left(\frac{t}{T_s}\right) = \begin{cases} 1, & -T_s/2 \leqslant t < T_s/2, \\ 0, & \text{otherwise.} \end{cases} \tag{4.4}$$

The filter's frequency response is calculated as

$$G(f) = \mathcal{F}\big[g(t)\big] = \text{sinc}\left(\frac{f}{F_s}\right) = \frac{\sin\big(\pi f/F_s\big)}{\pi f/F_s}, \tag{4.5}$$

where $\mathcal{F}\big[\cdot\big]$ denotes the Fourier transform operator, and $F_s = 1/T_s$ is the sampling frequency. The Fourier transforms of $x(n)$ and its continuous-time version $x_c(t)$ are related to each other according to

$$X(f) = \mathcal{F}\big[x(n)\big] = \text{rep}_{F_s}\big[X_c(f)\big] = \sum_{i=-\infty}^{+\infty} X_c(f - iF_s), \tag{4.6}$$

where $X_c(f) = \mathcal{F}\big[x_c(t)\big]$. The Fourier transform of $x_{ZOH}(t)$ is then given by

$$X_{ZOH}(f) = \mathcal{F}\big[x_{ZOH}(t)\big] = X(f) \cdot G(f). \tag{4.7}$$

Figure 4.5 shows the effects of the ZOH operation in the frequency-domain. It can be seen that the *sinc* response causes

- a slight rolloff of the signal spectrum within $[-F_s/2, +F_s/2]$, and
- an attenuation of the digital images located at the multiples of F_s, i.e. around the zeros of the *sinc* response.

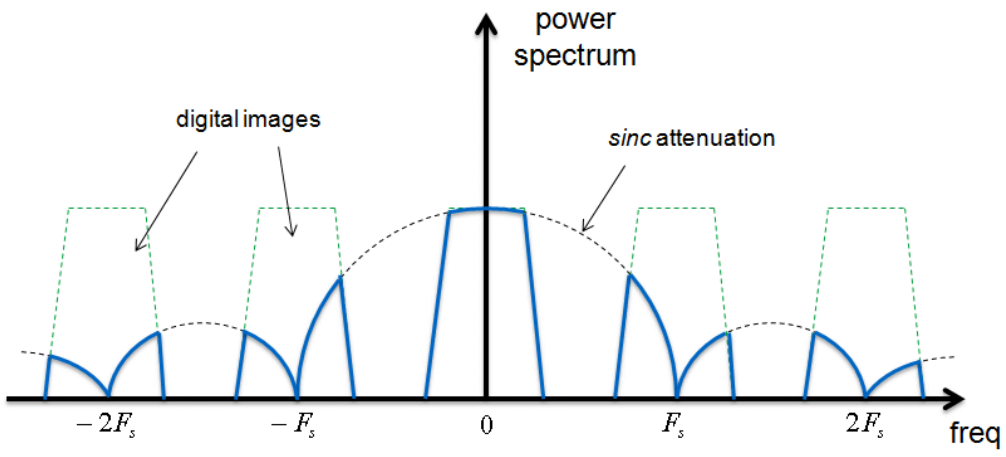

Figure 4.5: Effects of the ZOH operation in the frequency-domain.

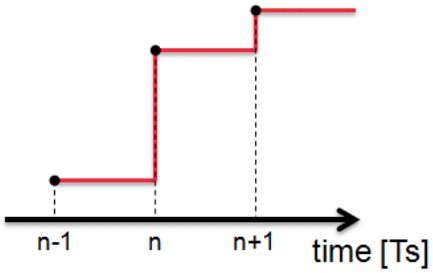

Figure 4.6: Real ZOH operation in the time-domain.

It can be observed that the spectrum rolloff decreases and the image attenuation increases as F_s becomes much larger than the Nyquist rate $2B_s$. Moreover, the digital images are pushed farther away from the main signal.

Equations (4.3) to (4.7) describe the ideal ZOH operation. In practice, the filter's impulse response is delayed with respect to $g(t)$ by $T_s/2$, for the filter to be causal. This means that each *rect* is no longer centered on the corresponding sample of $x(n)$, but it starts from the sample instead (compare Figure 4.4 to Figure 4.6 for clarity). The new impulse response is

$$g'(t) = g(t - T_s/2) = \begin{cases} 1, & 0 \leqslant t < T_s, \\ 0, & \text{otherwise}, \end{cases} \tag{4.8}$$

which results in a linear phase shift of the frequency response, according to

$$G'(f) = \mathcal{F}\big[g'(t)\big] = e^{-j2\pi \frac{T_s}{2} f} \cdot G(f) = e^{-j\pi \frac{f}{F_s}} \cdot \frac{\sin\big(\pi f/F_s\big)}{\pi f/F_s}. \tag{4.9}$$

The ZOH operation as described above cannot be modeled directly in MATLAB. Only a "discrete-time ZOH" can be performed, where each sample of $x(n)$ is repeated

N_{ZOH} times. The integer quantity N_{ZOH} is given by

$$N_{ZOH} = \frac{T_s}{T_{s,out}} = \frac{F_{s,out}}{F_s}, \tag{4.10}$$

where $T_{s,out}$ and $F_{s,out}$ are the new sampling period and frequency respectively. The whole process is equivalent to filtering $x(n)$ with the sampled version of $g'(t)$, expressed as

$$g''(k) = g'(kT_{s,out}) = \begin{cases} 1, & k = 0, \ldots, N_{ZOH} - 1, \\ 0, & \text{otherwise.} \end{cases} \tag{4.11}$$

The output signal is thus equal to the sampled version of $x_{ZOH}(t)$, with period $T_{s,out}$. The new frequency response of the filter is

$$G''(f) = \mathcal{F}\big[g''(k)\big] = \mathrm{rep}_{F_{s,out}}\big[G'(f)\big] = \sum_{i=-\infty}^{+\infty} G'(f - iF_{s,out}), \tag{4.12}$$

which approaches $G'(f)$ in the center of band $[-F_{s,out}/2, +F_{s,out}/2]$, if N_{ZOH} is large enough.

4.3 Non-idealities of the RF-DAC

4.3.1 Current source mismatches

Due to global and local variations during the manufacturing process of CMOS chips, the drain currents of the current source transistors are never perfectly matched. This causes static non-linearity in a current-steering DAC, where transistor mismatches manifest themselves as Integral Nonlinearity (INL) and Differential Nonlinearity (DNL) of the DAC transfer curve. A thorough treatment of this topic can be found in [17]. In this work, a simple MATLAB model for the transistor mismatches is developed, in order to quickly verify the DAC linearity through simulations.

The relative variance of the drain current of a MOS transistor can be expressed as [30, 31]

$$\frac{\sigma_{Id}^2}{I_d^2} = \frac{4A_{vt}^2}{WL(V_{GS} - V_T)^2} + \frac{A_\beta^2}{WL}, \tag{4.13}$$

where I_d is the nominal drain current, A_{vt} and A_β are technological parameters, $(V_{GS} - V_T)$ is the gate overdrive voltage, W is the channel width and L is the channel length. By assuming that all current sources of a converter have the same L and are biased with the same gate overdrive voltage, all constant terms of (4.13) can be gathered into

$$K_0 = \frac{4A_{vt}^2}{L(V_{GS} - V_T)^2} + \frac{A_\beta^2}{L}, \tag{4.14}$$

and the relative variance simplifies to

$$\frac{\sigma_{Id}^2}{I_d^2} = \frac{K_0}{W}. \tag{4.15}$$

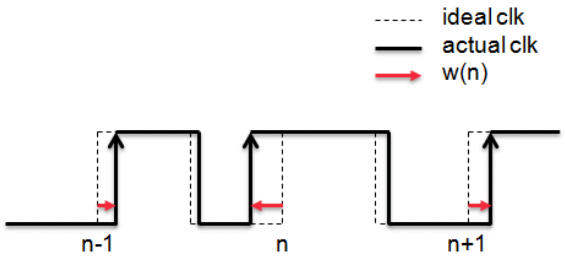

Figure 4.7: Clock waveform with jitter.

Under the above assumptions, the absolute standard deviation of the LSB current I_{LSB} can be written as

$$\sigma_{I_{LSB}} = I_{LSB}\sqrt{\frac{K_0}{W_{LSB}}}, \tag{4.16}$$

where W_{LSB} is the channel width of an LSB current source. Given that I_d is directly proportional to W, the current mismatch of a transistor providing $I_d = M \cdot I_{LSB}$ is thus given by

$$\begin{aligned} \sigma_{Id} &= M \cdot I_{LSB}\sqrt{\frac{K_0}{M \cdot W_{LSB}}} \\ &= \sqrt{M} \cdot \sigma_{I_{LSB}}. \end{aligned} \tag{4.17}$$

The above analysis leads to the following considerations. Equation (4.13) tells that, if the LSB current can be chosen freely, its relative variance can be reduced either by increasing the gate overdrive voltage, or by making the transistor larger (i.e. increasing W or L or both). On the other hand, if I_{LSB} is constrained (for example by the output power requirement), its relative variance can be only reduced by increasing the transistor area WL while keeping the aspect ratio W/L unchanged. In either cases, once $\sigma_{I_{LSB}}$ is fixed, the standard deviation of any current source larger than I_{LSB} is automatically determined by (4.17).

4.3.2 Clock jitter

Clock jitter is defined as the variation of the clock period over time. This concept is illustrated in Figure 4.7. In the case of an RF-DAC, the clock signals affected by jitter can be the the BB clock and the LO clock.[2]

There are a number of potential sources of clock jitter [17, 32]. Some examples are listed below.

- Phase noise of the PLL or other circuit that generates the clock signal results in jitter which is uncorrelated with the input data to be converted.

[2]Although the BB clock is derived from the LO clock through integer division in order to avoid glitches, the two signals are considered independently in this section.

- The load of the clock driver may vary with the data that are fed to the converter, which causes code-dependent clock jitter.

- The parasitic resistance of the power supply rails is also a source of code-dependent clock jitter, because of interference arising during input data transitions.

Jitter due to phase noise is a problem related to good PLL/oscillator design, and it is beyond the scope of this analysis. On the other hand, jitter caused by the activity of the circuitry must be well understood, since it can be a major source of nonlinearity in data converters. The derivation that follows is partially based on, and further expands, the model presented in [17].

The effect of clock jitter in the BB signal can be modeled as follows. As explained in Section 4.2.2, signal reconstruction takes place in the DAC by means of the ZOH operation

$$x_{ZOH}(t) = \sum_{i=-\infty}^{+\infty} x(i) \cdot g'(t - iT_s), \tag{4.18}$$

where $g'(t)$ is the delayed *rect* function given by (4.8). The sampling jitter signal $w(n)$, shown in Figure 4.7, is defined as the amount of deviation of the clock edge from its ideal position at time instant nT_s. The deviation is defined to be positive if the clock edge is delayed, negative otherwise. In the presence of sampling jitter, (4.18) modifies to

$$x_{ZOH}(t) = \left[\sum_{i=-\infty}^{+\infty} x(i) \cdot g'(t - iT_s) \right] + e_{BB}(t), \tag{4.19}$$

where the error signal $e_{BB}(t)$ is given by

$$e_{BB}(t) = \sum_{i=-\infty}^{+\infty} \left(\overbrace{\big[x(i) - x(i-1)\big]}^{\text{discrete-time derivative}} \cdot \overbrace{\big[u\big(t - iT_s - w(i)\big) - u\big(t - iT_s\big)\big]}^{\text{PWM jitter signal}} \right), \tag{4.20}$$

and $u(t)$ is the unit step function defined as

$$u(t) = \begin{cases} 0, & t < 0, \\ 1, & t \geqslant 0. \end{cases} \tag{4.21}$$

Figure 4.8 shows the various components of the output $x_{ZOH}(t)$. As stated by (4.20), the error signal can be thought as a multiplication between the discrete-time derivative of the input signal, and the "PWM jitter signal" given by

$$g(t) = \sum_{i=-\infty}^{+\infty} \big[u\big(t - iT_s - w(i)\big) - u\big(t - iT_s\big)\big], \tag{4.22}$$

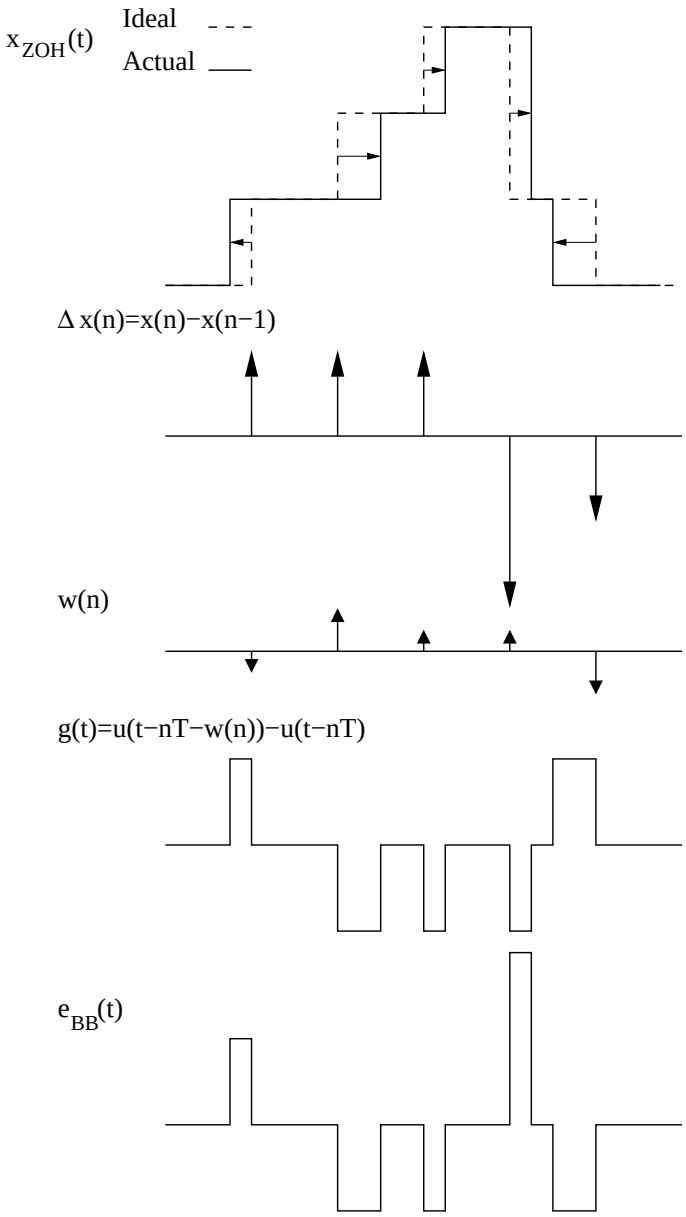

Figure 4.8: Components of the output $x_{ZOH}(t)$. Modified with permission from [17].

which looks like a train of rectangles with unity amplitude and lengths defined by $w(n)$, i.e. it resembles a Pulse-Width Modulated (PWM) signal. More insight into the properties of $g(t)$ can be gained by computing its Fourier transform

$$\begin{aligned} G(f) &= \mathcal{F}\big[g(t)\big] \\ &= \int_{-\infty}^{+\infty} \left[\sum_{i=-\infty}^{+\infty} \big[u\big(t - iT_s - w(i)\big) - u\big(t - iT_s\big)\big] \right] e^{-j2\pi ft} dt \\ &= \sum_{i=-\infty}^{+\infty} \left[\int_{iT_s+w(i)}^{+\infty} e^{-j2\pi ft} dt - \int_{iT_s}^{+\infty} e^{-j2\pi ft} dt \right] \\ &= \sum_{i=-\infty}^{+\infty} \int_{iT_s+w(i)}^{iT_s} e^{-j2\pi ft} dt \\ &= \sum_{i=-\infty}^{+\infty} \frac{e^{-j2\pi fiT_s}}{j2\pi f} \big[e^{-j2\pi fw(i)} - 1\big]. \end{aligned} \tag{4.23}$$

At low frequencies, i.e. comparable to the signal bandwidth, the product $fw(i)$ is very small. Therefore, the Taylor approximation $\big[e^{-j2\pi fw(i)} - 1\big] \approx -j2\pi fw(i)$ holds, and $G(f)$ becomes

$$G(f) \approx -\sum_{i=-\infty}^{+\infty} w(i) \cdot e^{-j2\pi fiT_s} = -W(f), \tag{4.24}$$

where $W(f)$ is the discrete-time Fourier transform of $w(n)$.

The relationship given in (4.24) is important, because it shows that the low-frequency spectral content of $G(f)$ equals that of $W(f)$. The similarity between $g(t)$ and $w(n)$ can be seen intuitively in Figure 4.8. If $w(n)$ is thought as a sequence of dirac impulses, then each impulse has the same area (with opposite sign) as the corresponding rectangle in $g(t)$.

The above discussion proves that code-dependent sampling jitter results in distortion of the output signal $x_{ZOH}(t)$. Indeed, $g(t)$ is multiplied by the discrete-time derivative of $x(n)$ in (4.20), i.e. by a highpass-filtered version of $x(n)$ itself.[3] Figure 4.9 plots the frequency response of the discrete-time derivative. If the dependency of $w(n)$ on $x(n)$ is of even-order, then the resulting distortion will be of odd-order, and vice versa [17]. Moreover, if the bandwidth of $x(n)$ is relatively high compared to its sampling rate $F_s = 1/T_s$ (i.e. the baseband signal has a low OSR), then the discrete-time derivative assumes larger values, and the output distortion is magnified.

The effect of clock jitter in the LO signal can be modeled as follows. As stated in Section 2.2, the output of an ideal I-Q upconverter can be expressed as

$$x_{RF}(t) = x_{BB}(t) \cdot e^{j2\pi f_c t}, \tag{4.25}$$

[3]The discrete-time derivative can be seen as a 2-tap FIR filter with coefficients $[1, -1]$, which shows a highpass frequency response.

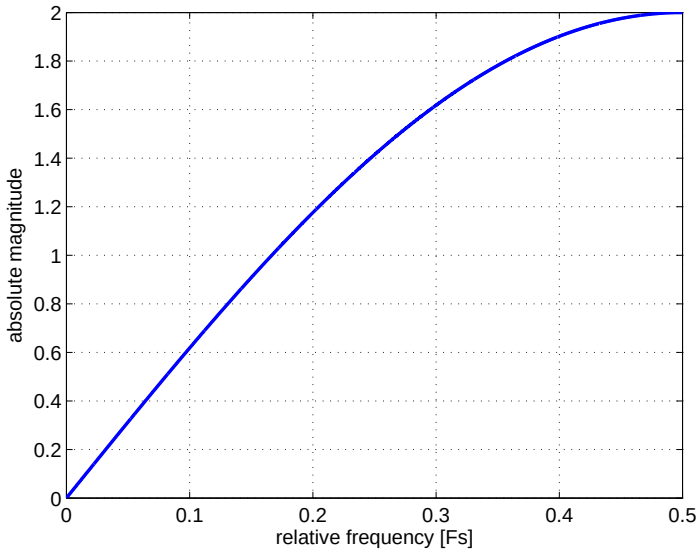

Figure 4.9: Frequency response of the discrete-time derivative.

although only the real part of (4.25) is actually taken. Here the jitter signal can be replaced by its continuous-time version $w(t)$, which is better suited to the sinusoidal carrier in (4.25). The I-Q upconverter output then becomes

$$x_{RF}(t) = x_{BB}(t) \cdot e^{j2\pi f_c(t+w(t))} = x_{BB}(t) \cdot e^{j2\pi f_c t} \cdot e^{j2\pi f_c w(t)}. \tag{4.26}$$

Since the maximum value assumed by $w(t)$ is expected to be much smaller than the LO period $T_{LO} = 1/f_c$, the rightmost exponential term in (4.26) can be approximated with its first-order Taylor-series expansion as

$$e^{j2\pi f_c w(t)} \approx 1 + j2\pi f_c w(t). \tag{4.27}$$

By substituting this relationship into (4.26), we get

$$x_{RF}(t) \approx \left[x_{BB}(t) + e_{LO}(t)\right] \cdot e^{j2\pi f_c t}, \tag{4.28}$$

where the error signal, which is upconveted to RF together with $x_{BB}(t)$, is given by

$$e_{LO}(t) = j2\pi f_c w(t) x_{BB}(t). \tag{4.29}$$

It can be seen from (4.29) that a multiplication takes place between the baseband signal and the jitter signal, resulting in odd-order distortion if the dependency of $w(t)$ on $x_{BB}(t)$ is of even-order, and vice versa. However, the amount of the distortion is now proportional to the relative magnitude of $w(t)$ with respect to the LO period $T_{LO} = 1/f_c$, rather than the discrete-time derivative of the baseband signal. Therefore, in presence of LO jitter, no improvement of the output signal quality can be expected by simply increasing the OSR of the baseband input.

In order to verify the models presented above, and to evaluate the effects on the system performance, the MATLAB model shown in Figure 4.1 was modified to include both BB and LO clock jitter in the RF-DAC. A high oversampling ratio of the output signal must be used in order to increase the time resolution, which results in rather long simulation time.

The BB sampling jitter was implemented as shown in the following example. Imagine that a discrete-time sine-wave baseband signal undergoes an ideal, discrete-time ZOH for the first 3 sampling periods, with an OSR of 5. This operation can be thought as a time vector

$$t = \begin{bmatrix} 0\ 0\ 0\ 0\ 0 \mid 1\ 1\ 1\ 1\ 1 \mid 2\ 2\ 2\ 2\ 2 \end{bmatrix} \cdot T_s, \tag{4.30}$$

which is used to sample the baseband signal

$$x(t) = \sin(2\pi f_0 t). \tag{4.31}$$

Now let us assume a jitter signal given by

$$w = \begin{bmatrix} 0 & -0.4 & 0.2 \end{bmatrix} \cdot T_s, \tag{4.32}$$

i.e. the rising edges of the sampling clock are delayed by 0%, -40%, and 20% of T_s respectively. This is an unreasonably large amount jitter, used only in this example for clarity. The time vector with jitter is then given by

$$t_{jitter} = \begin{bmatrix} 0\ 0\ 0\ \overbrace{1\ 1 \mid}^{-40\%}\ 1\ 1\ 1\ 1\ 1\ \overbrace{\mid 1}^{+20\%}\ 2\ 2\ 2\ 2 \end{bmatrix} \cdot T_s, \tag{4.33}$$

which shows how the sampling edges of the clock are moved away from their ideal positions. The time vector with jitter is then used to sample (4.31) as previously. Figure 4.10 shows the time-domain result of reconstructing a discrete-time sine-wave by means of the ZOH with jitter.

The LO jitter was implemented in a similar manner as in the BB case. However, now the edges of the LO clock are moved according to the jitter signal, resulting in a waveform like that of Figure 4.7.

4.3.3 Timing error

Timing error is defined as non-ideal synchronization between the unit elements of a DAC, i.e. the clock signal has different static delays to different unit conversion cells (Figure 4.11) [5, 33–35]. Like jitter, timing error can affect both the BB and the LO clocks in an RF-DAC. However, only the latter case will be considered in this section. Due to the importance of this topic, a new analytical model for the LO timing error is developed, which allows to predict the effect of imperfect timing synchronization on the RF-DAC performance.

There are different causes for timing error in data converters. The main sources are listed below.

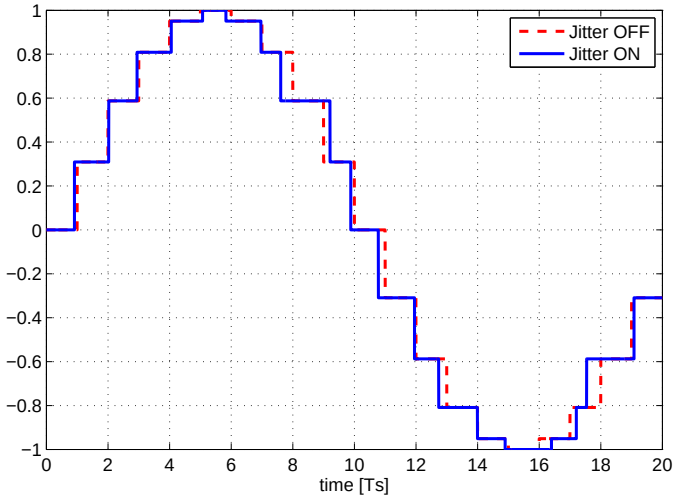

Figure 4.10: Reconstruction of a discrete-time sine-wave in presence of random clock jitter.

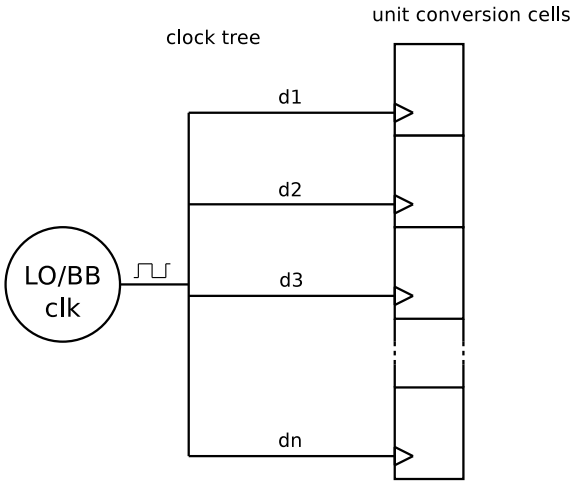

Figure 4.11: Timing error in the RF-DAC.

- Process variations are always present in silicon chips. These variations can lead to random delays between clock source and different unit cells.

- If not all conversion elements have the same weight, then the clock delays to differently weighted cells can be unbalanced, because of the different loads seen by the drivers.

- Process gradients (e.g. nonuniform oxide thickness over the silicon wafer) and unbalanced clock distribution network are also source of timing error. In this case, the delay is a function of the unit cell's position on the layout.

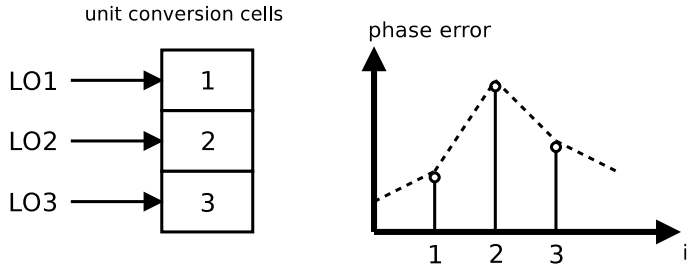

Figure 4.12: The phase error profile.

Careful floor planning and layout design can help to reduce the timing error due to cell weights, process gradients and unbalanced clock tree. However, timing error cannot be completely eliminated.

To see how timing error affects the performance of a differential, fully thermometer-coded RF-DAC, first consider the "phase error profile" $\varphi(i)$, shown in Figure 4.12. The phase error profile is formally defined as

$$\varphi(i) = 2\pi f_c d_i, \tag{4.34}$$

where f_c is the carrier (i.e. LO) frequency, and d_i is the clock delay from the LO source to the i-th cell of the converter (assumed to be much smaller than $T_{LO} = 1/f_c$). The signal that modulates the i-th cell is then given by

$$LO_i(t) = e^{j(2\pi f_c t + \varphi(i))}. \tag{4.35}$$

That is, $\varphi(i)$ represents the amount of phase shift of the LO signal modulating each cell, with respect to the ideal case.

Assume that the ideal output signal of the single RF-DAC can be expressed with the complex notation

$$RF_{ideal}(t) = \tilde{x}(t) \cdot e^{j2\pi f_c t}. \tag{4.36}$$

In this case, the normalized signal $\tilde{x}(t) \in [-1/2, +1/2]$ is the real baseband input to the converter. Notice that (4.36) is a continuous-time expression, and it does not take into account the effects of amplitude quantization. In this context, the phase error profile $\tilde{\varphi}(a)$ can be also thought as a continuous function of the normalized cell index $a \in [-1/2, +1/2]$. As will be shown later on, these simplifying assumptions do not compromise the validity of the model, as long as the number of bits used in the conversion N_{bits} is large enough.

Under all of the above assumptions, the actual RF-DAC output can be expressed as

$$RF_{real}(t) = RF_{ideal}(t) + e_{RF}(t), \tag{4.37}$$

where the "RF" error signal is given by

$$e_{RF}(t) = e_{BB}(t) \cdot e^{j\left(2\pi f_c t + \frac{\pi}{2}\right)}, \tag{4.38}$$

and the "baseband" error signal depends on the RF-DAC input as

$$e_{BB}(t) = \Psi\big(\tilde{x}(t)\big) - \frac{\Psi\left(\frac{1}{2}\right) + \Psi\left(-\frac{1}{2}\right)}{2}, \tag{4.39}$$

where the function $\Psi(a)$ is calculated as the primitive of the phase error profile, according to

$$\Psi(a) = \int \tilde{\varphi}(a) da. \tag{4.40}$$

Equations (4.37) to (4.40), whose detailed derivation can be found in Appendix B, can be directly used to evaluate how an arbitrary phase error profile $\tilde{\varphi}(a)$ affects the RF-DAC output. They are helpful when studying the effects of process gradients, which can be often modeled as linear or quadratic dependence of the clock delay on the unit cell's relative position [33]. In these cases, it is clear that timing error results in distortion to the output, because the baseband signal $\tilde{x}(t)$ is distorted through $\Psi(a)$ in (4.39), before being upconverted and added to the ideal RF signal. As will be shown in Section 5.6, it is possible to calculate the nonlinearity in closed form.

In the study of process variations, the discretized version of the timing error model has to be used, because each delay d_i is a random variable with Gaussian distribution [35]. The discrete model is also derived in Appendix B.

Regardless of continuous or discrete model, two implications can be obtained by exploiting the properties of the integral:

- $\tilde{\varphi}(a)$ even $\implies$ $\Psi(a)$ odd $\implies$ $e_{BB}(t) = \Psi\big(\tilde{x}(t)\big)$;
- $\tilde{\varphi}(a)$ odd $\implies$ $\Psi(a)$ even $\implies$ $e_{BB}(t) = \Psi\big(\tilde{x}(t)\big) - \Psi\big(1/2\big)$.

These two relationships lead to an important observation: the layout of the RF-DAC should be designed symmetrical, in order to make the phase error profile as symmetrical and even as possible. This allows to cancel the large LO leakage coming from the constant term in (4.39), as well as the even-order distortion.

In the MATLAB model of Figure 4.1, the LO timing error was implemented as follows. The square-wave LO signal is expanded into a $N_{cells} \times N_{samples}$ matrix, where N_{cells} is the number of unit conversion cells, and $N_{samples}$ is the total number of samples of the LO signal. A high oversampling ratio must be used in order to gain a good enough time resolution, and be able to model the timing error. The result is that now there is one copy of the LO signal in each row of the matrix, which can be fed to a single unit cell. Hence, it is possible to shift each of the LO signals, according to the phase error profile.

An example matrix with $OSR = 5$ may look like this:

$$LO = \left[\begin{array}{ccccc|ccccc|c} 0 & 0 & 0 & 0 & 0 & 1 & 1 & 1 & 1 & 1 & \dots \\ 0 & 0 & 0 & 0 & 0 & 1 & 1 & 1 & 1 & 1 & \dots \\ 1 & 0 & 0 & 0 & 0 & 0 & 1 & 1 & 1 & 1 & \dots \\ \multicolumn{11}{c}{\dots\dots\dots\dots\dots\dots\dots\dots\dots\dots\dots} \\ 0 & 0 & 0 & 1 & 1 & 1 & 1 & 1 & 0 & 0 & \dots \end{array}\right]. \tag{4.41}$$

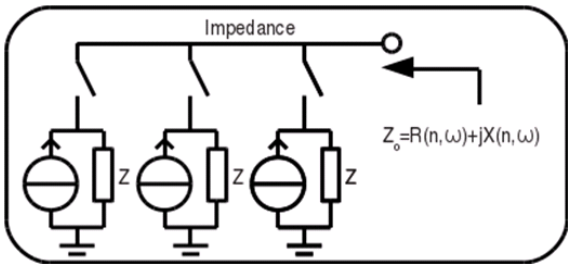

Figure 4.13: Overall output impedance of a current-steering DAC.

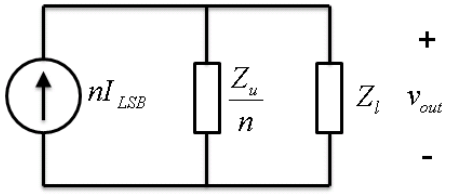

Figure 4.14: Model for the output impedance of a single-ended, fully thermometer-coded DAC.

Note how the third row is delayed by one sample, and the last row is anticipated by two samples.

4.3.4 Nonlinear output impedance

In a current-steering DAC, another major source of nonlinearity comes from the nonlinear output impedance of the converter itself [17,36]. The concept is illustrated in Figure 4.13. Each current source has its own finite output impedance, coming mainly from the channel length modulation effect of MOS transistors. Since the number of parallel current sources is code-dependent, the overall output impedance becomes code-dependent as well, which causes distortion. The individual current source impedances can be boosted by means of cascoding techniques. However, this comes at the expense of reduced voltage swing available at the output, which is an important consideration in low-V_{DD} designs.

The nonlinear output impedance inherently affects the RF-DAC as well, since it is directly based on the current-steering architecture. However, this effect was not included in the MATLAB model of the DDRM shown in Figure 4.1. Circuit-level simulators are better suited to this kind of analysis. Instead, a simple first-order analytical model for the single-ended DAC is described in this subsection, which partially follows the derivation in [17]. The purpose is just to show that this phenomenon leads to AM-AM and AM-PM modulation in the converter, i.e. the nonlinearity affects both *amplitude* and *phase* of the output signal.

The simple electric model for the single-ended, fully thermometer-coded DAC is shown in Figure 4.14. If the codeword is denoted with n, then the total output

impedance seen by the n parallel active current sources is given by

$$Z_t(n) = Z_l || \frac{Z_u}{n} = \frac{Z_u Z_l}{Z_u + nZ_l}, \tag{4.42}$$

where Z_u is the output impedance of a single unit conversion cell, and Z_l is the load impedance.

Before we proceed with our analysis, an important observation about the validity of this model must be stated. With (4.42), we are using a *linear* analysis to model a *nonlinear* situation. Talking about impedances makes some sense only if we assume n to be constant over time, and each unit current source is sinusoidal with amplitude I_{LSB}. Under these assumptions, the total output current of the n parallel current sources is

$$i_n(t) = nI_{LSB} \cos \omega t, \tag{4.43}$$

which results in output voltage signal

$$v_{out}(t) = Z_t(n) i_n(t) = A(n) \cos\big(\omega t + \phi(n)\big), \tag{4.44}$$

where $A(n)$ and $\phi(n)$ are the AM-AM and AM-PM modulation functions that we are trying to evaluate. Thereby, our analysis does not model the actual situation where each unit current source has a constant output current I_{LSB}, and n varies over time. The modeling of this situation would involve nonlinear differential equations, and it is beyond the scope of this thesis. We are just interested in a first-order behavior of the nonlinear output impedance effect, which is well approximated by equations (4.42) to (4.44).

By keeping in mind the aforementioned limitation of our analysis, we can then proceed with the derivation. We define the ratio between load and unit element impedances as[4]

$$Q = \frac{Z_l}{Z_u}. \tag{4.45}$$

This quantity is in general a complex number, whose magnitude and phase are given by

$$|Q| = \frac{|Z_l|}{|Z_u|}, \tag{4.46}$$

$$\phi_q = \phi_l - \phi_u, \tag{4.47}$$

where ϕ_l and ϕ_u are the phases of Z_l and Z_u respectively. In an ideal DAC, $Q = 0$ because Z_u is infinite. In a real DAC, Q should be still kept as small as possible, in order to minimize the nonlinearity.

By substituting (4.45) into (4.42), the complex output impedance becomes

$$Z_t(n) = \frac{Z_l}{1 + nQ}, \tag{4.48}$$

[4]This quantity has nothing to do with the *quality factor* of an RLC network, conventionally represented with the symbol Q.

whose magnitude and phase are given by

$$|Z_t(n)| = \frac{|Z_l|}{\sqrt{1 + 2n|Q|\cos\phi_q + n^2|Q|^2}}, \tag{4.49}$$

$$\phi_t(n) = \phi_l - \phi_e(n), \tag{4.50}$$

and the phase error $\phi_e(n)$ is defined as

$$\phi_e(n) = \arctan\frac{n|Q|\sin\phi_q}{1 + n|Q|\cos\phi_q}. \tag{4.51}$$

For small values of $|Q|$, the phase error can be linearly approximated as a function of n, according to

$$\phi_e(n) \approx n|Q|\sin\phi_q. \tag{4.52}$$

Equation (4.49) suggests that there exists an optimum value for ϕ_q, which allows to minimize the dependence of the output impedance magnitude on n (i.e. the AM-AM modulation). By analyzing the magnitude function, it could be shown that such angle is related to $|Q|$ and N according to

$$\cos\phi_q = -\frac{N|Q|}{2}. \tag{4.53}$$

On the other hand, it can be immediately noted by looking to (4.51) that the most straightforward means of canceling out the phase dependence (i.e. the AM-PM modulation) is by choosing

$$\phi_q = 0. \tag{4.54}$$

Figure 4.15a plots magnitude and phase of the total output impedance, when ϕ_q ranges in the neighborhood of the optimum angle given by (4.53). It is clear that the net effect of minimizing the AM-AM modulation is to remove the linear dependence of $|Z_t|$ of n, and only some weaker second-order dependence is left. Furthermore, it is confirmed that AM-PM modulation is approximately modeled as linear addition to the load impedance angle, as predicted by (4.52).

Figure 4.15b plots the same quantities as before, when ϕ_q is close to 0° (i.e. $\phi_l \approx \phi_u$). The AM-PM modulation is now completely eliminated, whereas the AM-AM modulation shows approximately linear dependence of $|Z_t|$ on n. More importantly, with $\phi_q = 0$ the impedance analysis can be traced back to the case where both Z_l and Z_u are real. Hence, the same results presented in [17, 36] can be exploited in order to calculate the nonlinearity.

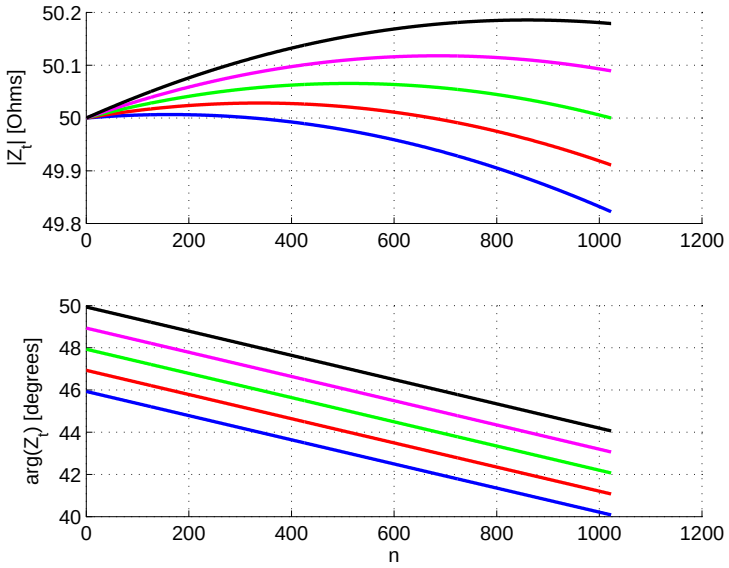

(a) *Minimized AM-AM modulation*

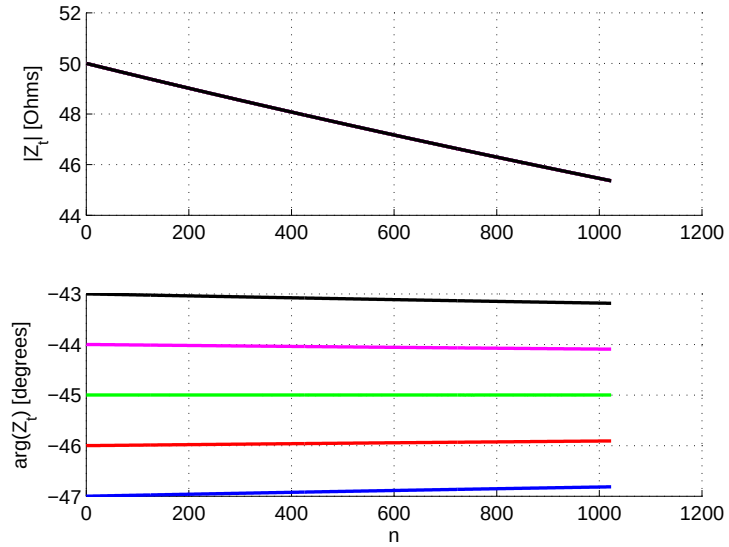

(b) *Minimized AM-PM modulation*

Figure 4.15: Overall output impedance seen by the n active parallel current sources of a 10-bit fully thermometer-coded DAC. Simulation with $|Z_l| = 50\Omega$, $|Q| = 10^{-4}$ (i.e. $|Z_u| = 500k\Omega$), $\phi_u = -45°$ (capacitive impedance). Different curves are plotted with ϕ_q ranging $\pm 2°$ around the optimum angles defined by (4.53) and (4.54).

Chapter 5

System-level design

This chapter presents the system-level design of an all-digital transmitter for LTE and LTE-A, based on the DDRM structure. The discussion starts from the frequency planning, where the most critical operating bands are identified. After that, the required converter resolution is derived form the out-of-band noise requirement. The first MATLAB simulation results on the ideal DDRM are then presented. These results reveal some problems, like the finite IRR, that are intrinsic to the DDRM architecture.

The second part of the chapter investigates, through MATLAB simulations, the effect of different non-idealities on the DDRM performance. All simulation results are compared with the expectations from the theoretical analysis of Chapter 4.

5.1 Frequency planning

Section 2.4.2 has introduced the frequency bands where LTE and LTE-A are designed to operate. Some observations can be made by analyzing Table 2.2 and Figure 2.8.

- Some bands are located very close to the GPS band: band 11 (about 120 MHz far), band 21 ($\approx$ 110 MHz) and band 24 ($\approx$ 20 MHz). When transmission is taking place in one of those bands, it is very likely that some signal power will leak to the GPS band, because of the nonlinearities of the DDRM. Therefore, the -160 dBc/Hz noise requirement is very challenging to meet in such cases.

- Some bands are located even closer to the ISM band: band 7 (16 MHz far), band 40 (0 MHz!) and band 41 (12 MHz). Similar observations can be stated as for the GPS band. Note that the transmission of LTE-A signals with bandwidths up to 40 MHz can take place in bands 40 and 41. In other words, the -160 dBc/Hz noise requirement will *not* be met in these cases.

- Some FDD bands are specified with a very small duplex distance: about 30 MHz for bands 12, 13, 14, and 17, and 41 MHz for band 20. Especially the latter band is very challenging, since LTE signals up to 20 MHz bandwidth

can be transmitted there. Such bands set tight linearity requirements for the DDRM.

- Bands 4 and 10 have the *largest* duplex distance (400 MHz). This sets a lower bound for the sampling rate of the baseband input signal to the RF-DACs. The sampling rate should be higher than 400 MHz, in order to make sure that the digital images attenuated by the weak *sinc* response of the ZOH do not disturb the own RX-band.

- Two bands (13 and 14) are located at frequencies such that the 2^{nd} Harmonic Distortion (HD_2) falls exactly in the GPS band. The HD_2 is (ideally) zero if the DDRM is implemented differentially, but it becomes a problem in case of single-ended realization.

- Three bands (5, 18, and 26) have the HD_3 falling in the ISM band. Since the HD_3 is a natural product of the square-wave LO signal used for upconversion in the DDRM, it can be only filtered out at the DDRM output (e.g. by the RF matching network).

The above statements, coupled with the observation that the LTE / LTE-A operating bands can be divided into four groups (see Section 2.4.2), lead to the following design choices.

5.1.1 Sampling rate

As stated in Section 2.3.2, the input sampling rate F_s should be an integer fraction of the LO frequency f_c. A good choice for F_s could be, for example:

- $F_s = f_c$ for bands belonging to Group I (699 - 915 MHz);

- $F_s = f_c/2$ for bands belonging to Group II and III (1427.9 - 2690 MHz);

- $F_s = f_c/4$ for bands belonging to Group IV (3400 - 3800 MHz).

In this way, F_s is always in the range 699 - 1345 MHz, which is a good compromise between speed requirements for the digital front-end, and relaxation of the DAC resolution. In addition, the chosen F_s is fairly higher than the 400 MHz specified above.

The digital front-end performs the necessary conversion from the LTE base sampling rate $F_{s,0}$ (Table 2.1) to f_c/M. A detailed description of the system-level architecture of such sampling rate converter can be found in [37]. For the simulations presented in the next sections, the LTE test vectors are created directly with high OSR, through the signal generator described in Section 3.1.

5.1.2 RF matching network

The design of the RF matching network is out of scope of this thesis. However, the grouping of the frequency bands described in Section 2.4.2 suggests that four different matching networks (or even four different RF front-ends) could be optimized for each of the band groups I - IV. This means that the passband of each matching network should be wide enough to accommodate every band belonging to the group, while the stopband attenuation should be large enough to reject all of the ZOH *sinc* images, harmonic distortion products, etc., thus preventing them to interfere with other bands.

5.2 Number of bits

As anticipated in Section 2.3.2, the main source of out-of-band noise in the DDRM (and, more generally, in all kinds of all-digital transmitters) is quantization noise, whose properties were explained in Section 4.2.1. Hence, the -160 dBc/Hz noise requirement directly determines the number of bits N_{bits} needed for the D/A conversion in the RF-DACs.

The high F_s of the baseband signal at the output of the digital front-end helps relaxing this requirement to some extent, because a high OSR increases the SNR in the quantized signal. Nowadays, this is the best means of dealing with quantization noise, because modern deep-submicron CMOS processes provide transistors with high switching speed, but poor analog performance. Thereby, it becomes easier to design a converter with reasonably higher sampling rate and smaller number of bits.

A lower bound for N_{bits} can be determined analytically, by observing that the SNR defined by (4.2) should be at least as large as the power density difference Δp given by (2.14). Therefore, a comparison between the two expressions results in

$$\overbrace{6.02N_{bits} + 10\log_{10}(OSR)}^{\text{SNR}} \geqslant \overbrace{160 - 10\log_{10} BW_{occ}}^{\Delta p}. \tag{5.1}$$

Inverting (5.1) and substituting $OSR = F_s/BW$ yields[1]

$$N_{bits} \geqslant \frac{160 - 10\log_{10} BW_{occ} - 10\log_{10}(F_s/BW)}{6.02}. \tag{5.2}$$

Note that $BW \approx BW_{occ}$ (see Table 2.1), and thus (5.2) could be further simplified to

$$N_{bits} \geqslant \frac{160 - 10\log_{10}(F_s)}{6.02}, \tag{5.3}$$

which clearly highlights the aforementioned relationship between N_{bits} and F_s.

Equation (5.2) reveals that the minimum required N_{bits} which achieves -160 dBc/Hz noise floor is 13. However, in order to leave some margin for errors, it was finally decided to use $N_{bits} = 14$ in the DDRM (as in [8]). This is a challenging requirement, which requires calibration in order to compensate for the inevitable static nonlinearity [17].

[1] According to the sampling theorem, the minimum theoretical sampling rate for an LTE signal is given by its RF bandwidth BW.

Input signal	CW	LTE
IRR (dBc)	-31	-
HD_3 (dBc)	-9	-10
Output power (dBm)	-	3
$ACLR_1$ (dB)	-	94
EVM_{best} (%)	-	0.76
Noise floor (dBc/Hz)	-	-167

Table 5.1: Simulated performance of the ideal DDRM.

5.2.1 Average output power

After fixing the converter resolution, we can determine the LSB current from the output power requirement. As stated in Section 2.4.3, the DDRM needs to provide about 12 dBm (i.e. 15.9 mW) peak output power to the PA. For a differential load impedance $R_L = 100\,\Omega$, this corresponds to a peak current

$$I_{peak} = \sqrt{\frac{P_{peak}}{R_L}} = 12.6 \text{ mA}. \tag{5.4}$$

Let us assume, for simplicity, that all of this current has to be provided by one single branch of the DDRM (i.e. either I or Q). The LSB current is then simply given by

$$I_{LSB} = \frac{I_{peak}}{2^{N_{bits}}} = 768 \text{ nA}. \tag{5.5}$$

The above calculation results in a slightly higher output signal power, because the value assumed by one DDRM branch when the other branch peaks is nonzero in practice. However, a certain amount of this power consists of out-of-band power (harmonic distortion, *sinc* images, etc.), which is filtered out by the RF matching network. As will be shown through simulations, these two effects perfectly compensate each other.

5.3 Ideal system-level simulations

Figure 5.1 shows the output spectrum of an ideal Continuous Wave (CW) simulation, i.e. with cosine/sine inputs (see Section 2.2). The simulation is performed with the MATLAB model depicted in Figure 4.1. The RF spectrum shows the desired upconverted tone at frequency $f_c + f_0$, as well as a large image tone (-31 dBc) located at $f_c - f_0$. The spectrum is repeated at the multiples of F_s, and attenuated by the *sinc* response of the ZOH (also shown in Figure 5.1). The HD_3 product (located around $3f_c$) is only 9 dB below the wanted tone (due to the square-wave LO signal), and thus it has to be largely attenuated by the RF matching network. The simulated performance is summarized in the second column of Table 5.1.

The poor IRR of the DDRM is due to the folding of the digital repetition spectrum (attenuated by the *sinc* response) around the zero-frequency. The IRR of an

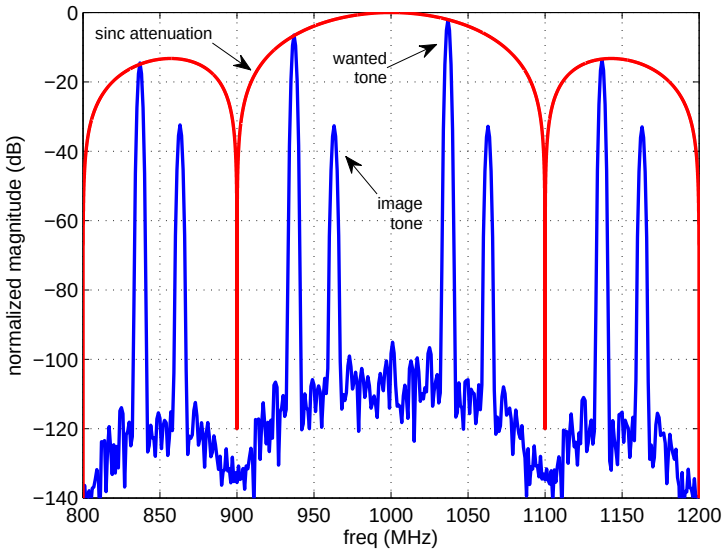

(a) *Narrowband spectrum*

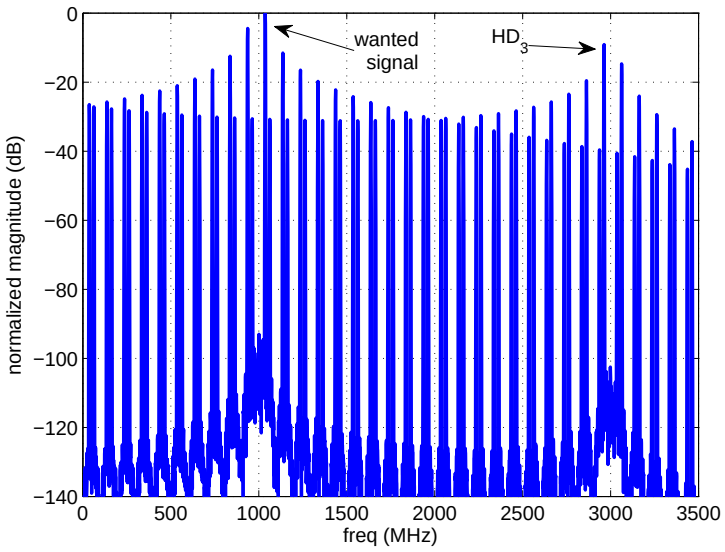

(b) *Wideband spectrum*

Figure 5.1: Output spectrum of ideal DDRM with CW input signal. Simulation with $f_0 = 37$ MHz, $F_s = 100$ MHz, $f_c = 1$ GHz.

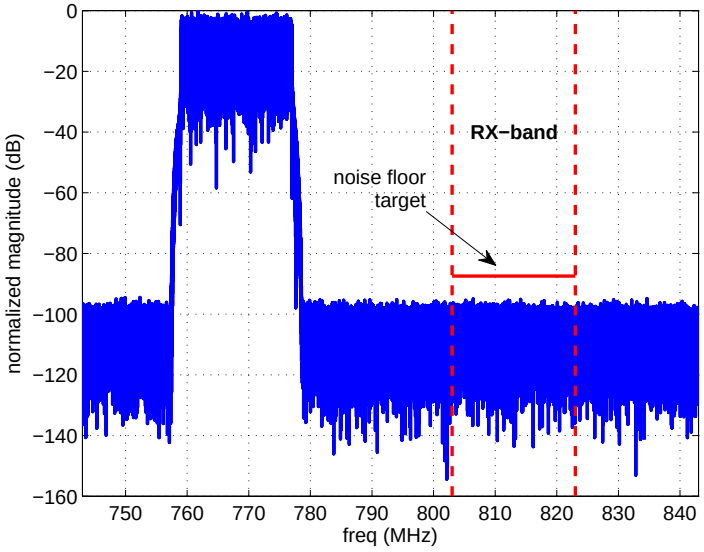

(a) *Narrowband spectrum*

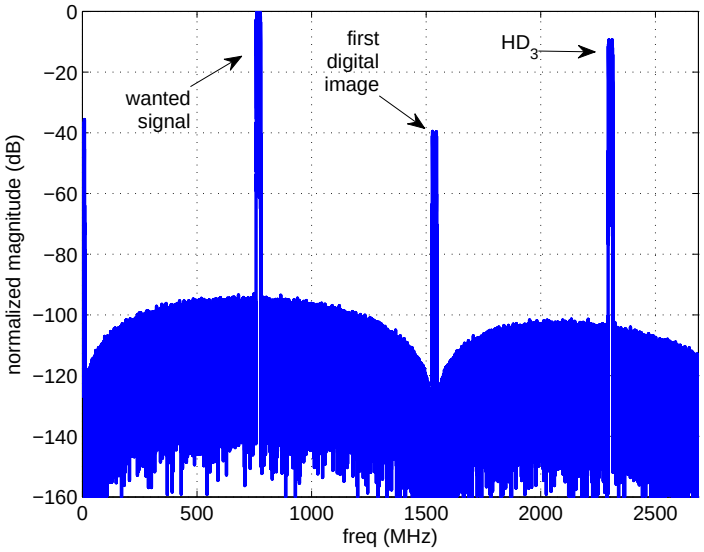

(b) *Wideband spectrum*

Figure 5.2: Output spectrum of ideal DDRM with 100 RB (20 MHz) LTE input. Simulation with $f_c = F_s = 768$ MHz (which does not belong to any of the bands listed in Table 2.2, but it allows to easily generate the baseband vector with $OSR = 25$). A duplex distance of 45 MHz was assumed, being very typical of Group I bands.

ideal DDRM is given by

$$IRR \approx -20\log_{10}\left(\frac{2f_c}{f_0} - 1\right) + 4 \qquad \text{[dB]}, \tag{5.6}$$

which shows no dependence on F_s, but only on the ratio between carrier frequency and baseband tone frequency. The detailed derivation of (5.6) is presented in Appendix C.

Figure 5.2 shows the output spectrum of the ideal DDRM with LTE input signal. Thanks to the *sinc* attenuation, the first digital image is attenuated by 39 dB, which will be further improved by the output matching network. The third column of Table 5.1 shows the simulated performance metrics. The -160 dBc/Hz noise floor is met with sufficient margin, confirming that the needed resolution for the D/A conversion is 14 bits, as derived in Section 5.2. The average output power (integrated only over the TX channel) perfectly fulfills the requirement, as predicted in Section 5.2.1. The ACLR is very large because it is determined by the quantization noise floor, as no nonlinearities affect the DDRM at this stage. The only parameter which shows a slight degradation is EVM_{best} (0.76%, from nearly 0% at the DDRM input). This is due to the same mechanisms that governs the finite IRR (see Appendix C).

5.4 Current source mismatches

The effect of static mismatches between current source transistors depends on the partitioning of the 14 input bits between the MSB and LSB segments, as will be shown later on in this section. The simulations presented below, unless otherwise stated, assume 6 thermometer-coded MSBs, and 8 binary-coded LSBs, with no calibration of the static nonlinearity.

Figure 5.3 shows the simulation result of a single RF-DAC fed with CW input signal. Equation (4.17) has been used to model the static mismatch in current source transistors with different weights. The resulting nonlinearity manifests itself as a large amount of spurs in the output spectrum. Since the degradation of the converter linearity has been already analyzed thoroughly in published literature [17], in this thesis the focus is shifted towards the effects on the LTE performance.

Figure 5.4 illustrates the consequences of transistor mismatches on the output RF spectrum of the DDRM, with LTE input. The relatively wide sidelobes around the main signal indicate high-order distortion, coming from the complex shape of the INL curve of the converter [17]. The net result is a higher out-of-band noise floor, especially in the vicinity of the main signal. The increased noise can potentially disturb other receive bands.

More insight into the LTE performance in presence of mismatches is given by the set of simulations presented in Figure 5.5. These simulations show the behavior of $ACLR_1$ (for the first adjacent LTE channel), RX-band noise floor, and EVM_{best}, as a function of the relative LSB current standard deviation $\sigma_{I_{LSB}}/I_{LSB}$. It is seen that $ACLR_1$ degrades quite linearly with $\sigma_{I_{LSB}}$, but the obtained values meet the specifications (Table 2.4) for LSB current deviations up to 100%. The same outcome

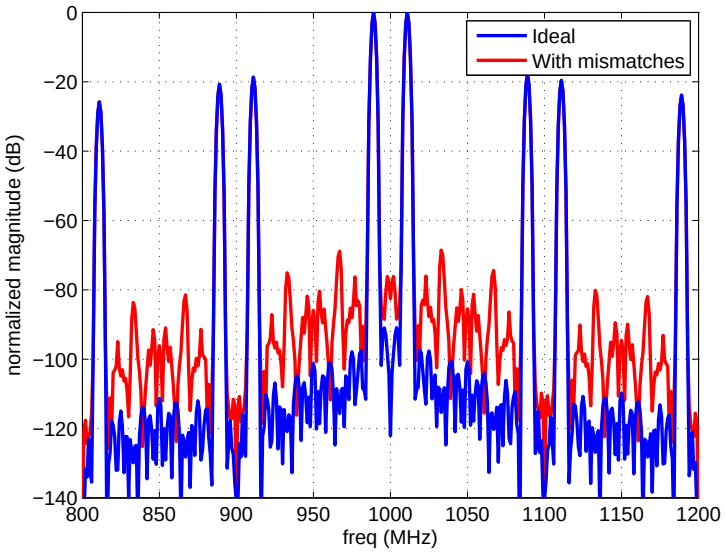

Figure 5.3: Effect of current source mismatches on the output spectrum of a single RF-DAC, with CW input signal. Simulation with $f_0 = 11$ MHz, $F_s = 100$ MHz, $f_c = 1$ GHz, $\sigma_{I_{LSB}}/I_{LSB} = 10\%$.

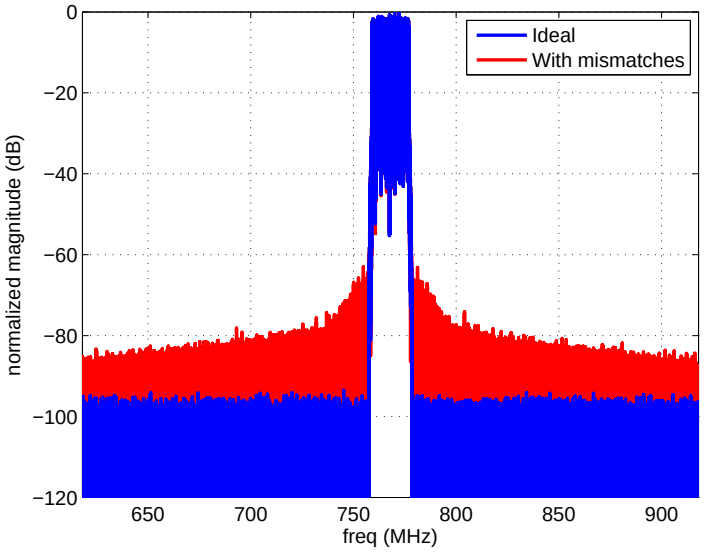

Figure 5.4: Effect of current source mismatches on the output spectrum of the DDRM, with 100 RB (20 MHz) LTE input. Simulation with $f_c = F_s = 768$ MHz, $\sigma_{I_{LSB}}/I_{LSB} = 10\%$.

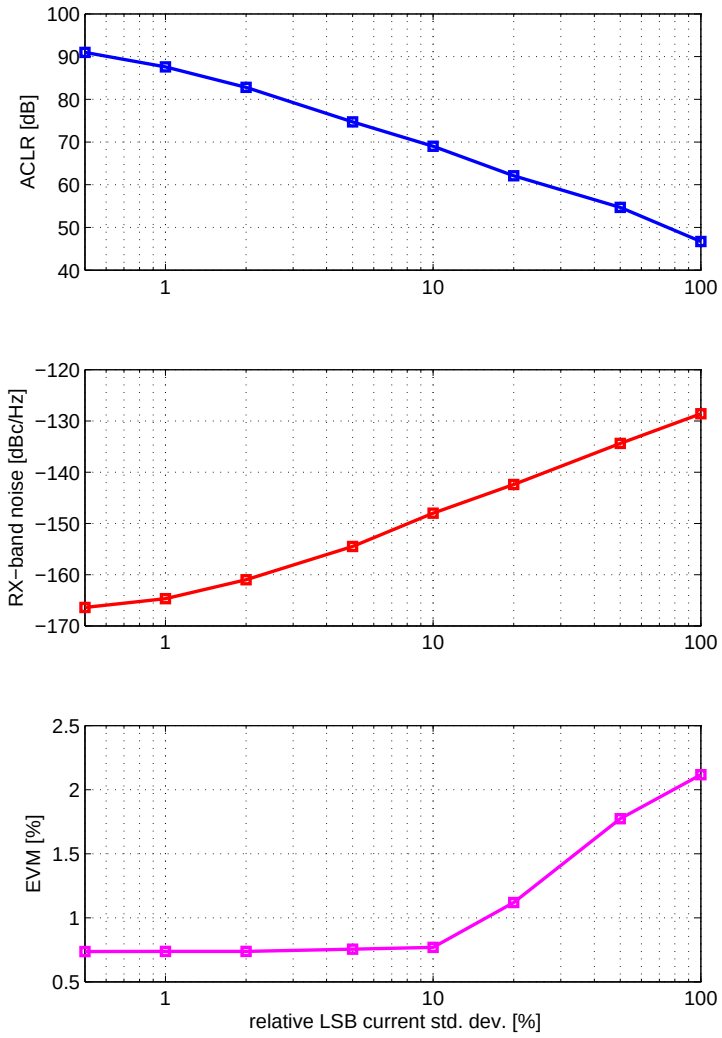

Figure 5.5: Effect of current source mismatches on various figures of merit of the DDRM, as a function of the relative LSB current standard deviation. Simulation with 100 RB (20 MHz) LTE input, $f_c = F_s = 768$ MHz. A duplex distance of 45 MHz was assumed.

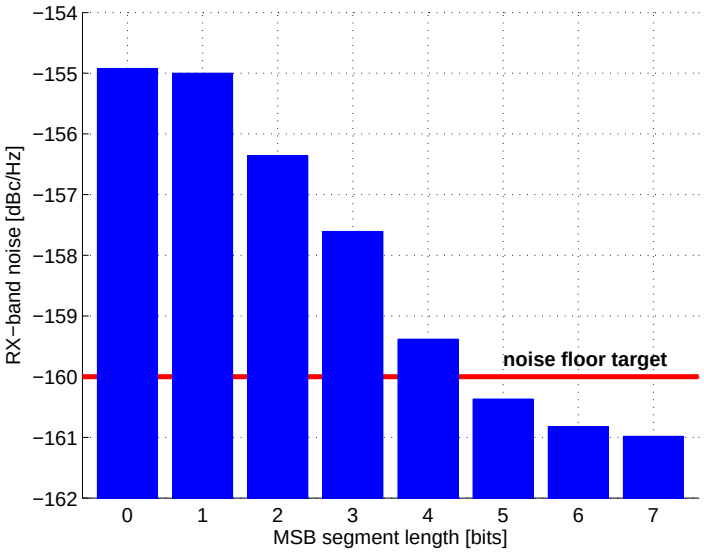

Figure 5.6: Effect of current source mismatches on the noise floor of the DDRM, as a function of the number of thermometer-coded MSBs. Simulation with 100 RB (20 MHz) LTE input, $f_c = F_s = 768$ MHz, $\sigma_{I_{LSB}}/I_{LSB} = 2\%$. A duplex distance of 45 MHz was assumed.

can be stated for EVM_{best}. On the other hand, the RX-band noise floor becomes higher than allowed already with $\sigma_{I_{LSB}}/I_{LSB} \approx 2\%$.

Figure 5.6 illustrates the behavior of the noise floor with various MSB segment lengths, assuming an LSB current deviation of 2%. Results highlight the trade-off between DC linearity and circuit complexity mentioned in Section 2.3.2. A given $\sigma_{I_{LSB}}$ determines the total amount of distortion power, which translates into raised noise floor (like in Figure 5.4). However, the shape of the INL curve of the converter changes with the number of MSBs. Increasing this number spreads the distortion power to higher frequencies. In the simulation of Figure 5.6 this is seen as decreased noise floor, because the assumed duplex distance is very small [17].

5.5 Clock jitter

In all clock jitter simulations presented in this section, the jitter signal $w(n)$ is chosen to have a second-order dependency on the input signal given by [17]

$$w(n) = w_{MAX}\big|x(n) - x(n-1)\big|^2. \tag{5.7}$$

This relationship reflects the physical origin of the jitter signal in the circuit, that is, the switching activity due to the number of changing thermometer-coded MSBs.

Figure 5.7 illustrates the RF output spectrum of the single converter with code-dependent clock jitter on the BB sampling clock. It is confirmed that a second-order

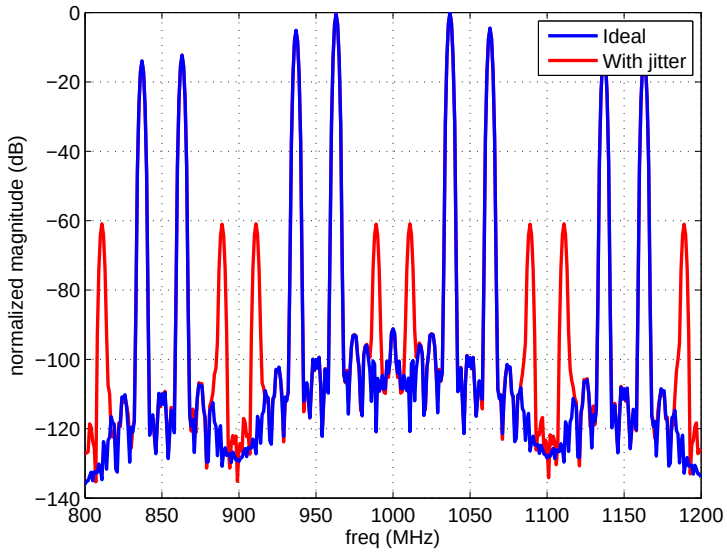

Figure 5.7: Output spectrum of single RF-DAC with CW input signal, and second-order code-dependent BB clock jitter. Simulation with $f_0 = 37$ MHz, $F_s = 100$ MHz, $f_c = 1$ GHz, $w_{MAX}/T_s = 0.1\%$.

dependency of $w(n)$ on $x(n)$ results in third-order distortion upconverted to RF (i.e. CIM_3), as predicted in Section 4.3.2.

Figure 5.8 plots the maximum relative BB jitter (w_{MAX}/T_s) which satisfies the linearity requirement $CIM_3 \leqslant -60$ dBc, as a function of the OSR of the input signal. It is seen that the negative effects of clock jitter are reduced as OSR is increased, because the magnitude of the discrete-time derivative in (4.20) gets smaller. By considering the practical worst-case OSR, i.e. when the largest bandwidth signal (20+20 MHz LTE-A) is processed at the lowest possible F_s (Band 1, $F_s = f_c/2 \approx$ 1000 MHz), the relative jitter signal has to be smaller than 2% to meet the CIM_3 target, which is a rather relaxed requirement. However, if the *absolute* magnitude of the jitter is fixed, then increasing the OSR does not help, because the *relative* jitter increases proportionally. In this case, the magnitude of the distortion spurs is only determined by the dependence of $w(n)$ on the input signal $x(n)$.

Much more severe is the impact of clock jitter in the LO signal. The output spectrum of the single RF-DAC with second-order LO jitter looks similar to that of Figure 5.7. However, now the distortion cannot be reduced by increasing the OSR of the baseband signal. As explained in Section 4.3.2, the only means of dealing with LO jitter is by decreasing the jitter signal itself.

Figure 5.9 shows the simulated magnitude of the CIM_3 term, versus the maximum relative LO jitter w_{MAX}/T_{LO}. In order to fulfill $CIM_3 \leqslant -60$ dBc, the jitter signal has to be smaller than 0.07% of the LO period. For the maximum carrier frequency $f_c = 3.8$ GHz, this means $w_{MAX} < 0.18$ ps. In order to achieve such a low jitter, the path of the LO signal in the RF-DAC has to be be very well isolated

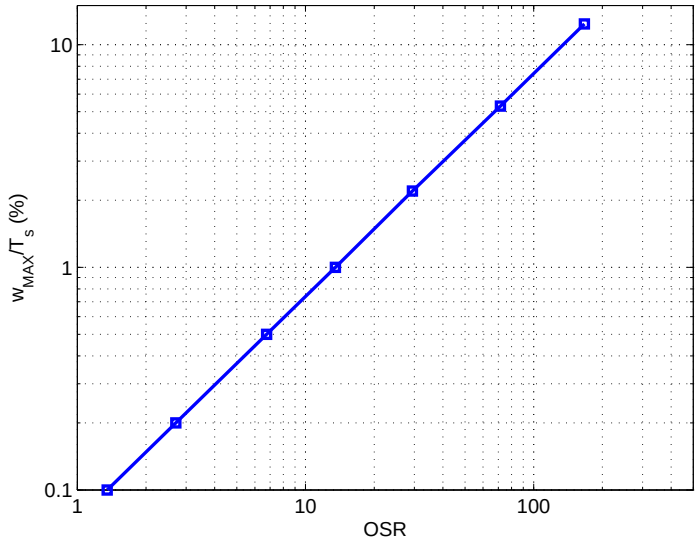

Figure 5.8: Simulated maximum relative BB jitter versus OSR of input signal, which meets $CIM_3 \leqslant -60$ dBc.

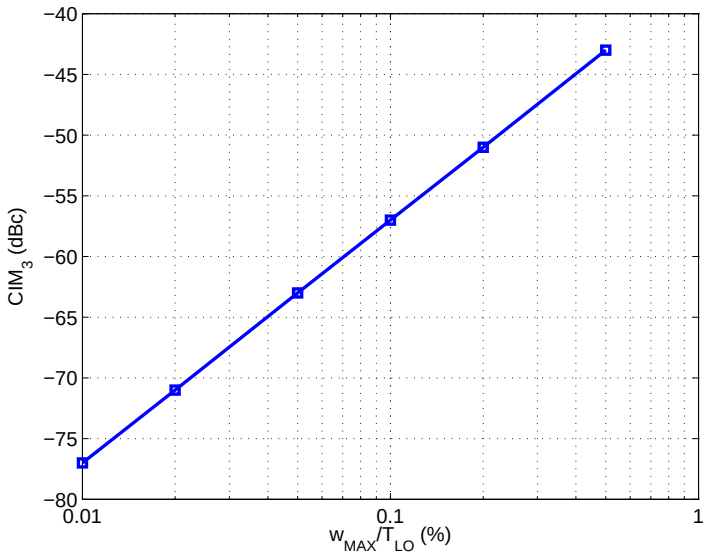

Figure 5.9: Simulated CIM_3 of the RF-DAC, versus maximum relative LO jitter.

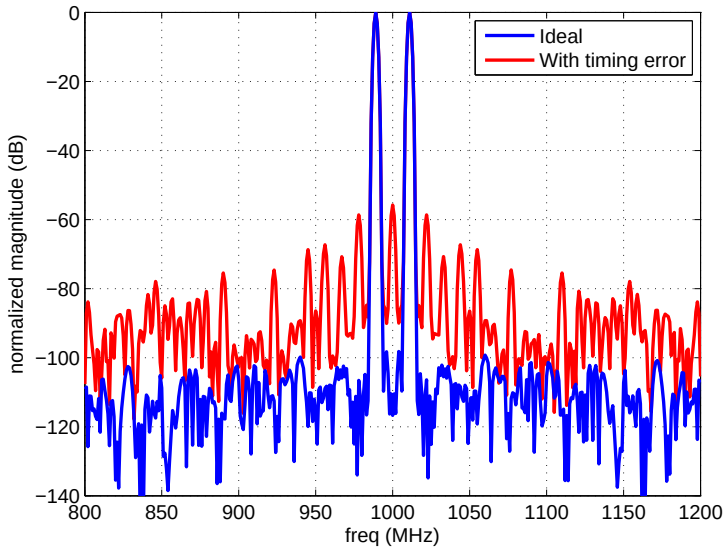

Figure 5.10: Output spectrum of single RF-DAC with CW input signal, and random Gaussian LO timing error in the MSB segment. Simulation with $f_0 = 11$ MHz, $F_s = 500$ MHz, $f_c = 1$ GHz. The standard deviation of the timing error is chosen such that the maximum delay mismatch between different cells is $d_{max} \approx 1\% \cdot T_{LO}$.

from the signal path. As a conclusion, it can be stated that clock jitter in the LO signal is a potentially critical source of nonlinearity in the RF-DAC.

5.6 Timing error

As in the case of current source mismatches, the effect of timing error in the distribution of the LO signal is affected by the MSB and LSB segment lengths. A 6+8 strategy is also assumed for the simulations presented in this section, unless otherwise stated. The effect of LO timing error is studied separately for each segment.

5.6.1 Timing error on the MSB segment

Figure 5.10 shows the CW output spectrum of a single RF-DAC, with Gaussian distributed LO timing error in the MSB segment (i.e. the delay of the LO signal to each MSB cell is a Gaussian random variable), and no timing error in the LSB segment. It is seen that even small delay mismatches can severely degrade the performance of the converter, resulting in raised noise floor and distortion spurs. The simulated noise floor, for example, is equivalent to that of an ideal 11-bit RF-DAC.

The simulation results can be intuitively explained as follows. As stated in Section 4.3.3, LO timing error can be thought as the addition of an error signal $e_{BB}(t)$ to the ideal baseband signal $x(t)$. In the discrete version of the analytical

model developed in this thesis (see Appendix B), the error signal is given by

$$e_{BB}(t) \approx \sum_{0}^{\text{round}[x(t)]} \varphi(i) - \frac{1}{2}\left[\sum_{1}^{2^{B-1}-1} \varphi(i) - \sum_{-(2^{B-1}-1)}^{-1} \varphi(i)\right]. \tag{5.8}$$

The first term in (5.8) is a time-variant summation of constant Gaussian random variables, i.e. the number of variables that are summed varies over time according to the input signal. The result of the summation is also a Gaussian random variable, whose time-varying standard deviation is given by

$$\begin{aligned} \sigma_e(t) &= \sqrt{\left|\sum_{i=0}^{\text{round}[x(t)]} \sigma^2_{\varphi(i)}\right|} \\ &\approx \sqrt{\left|x(t)\right|} \cdot \sigma_{MSB}, \end{aligned} \tag{5.9}$$

where $\sigma_{MSB} = \sigma_{\varphi(i)}$ is the standard deviation of the phase error for each MSB unit conversion cell. Hence, the resulting effect on the output is increased noise (because the error is random) *and* increased distortion (because the standard deviation is a function of the input).

Figure 5.11 illustrates the CW output spectra of a single RF-DAC, with the second-order LO timing error profiles shown in Figure 5.12. These simulations were performed on a 10-bit fully thermometer-coded converter. It is confirmed that even-order profiles result in odd-order distortion, whereas arbitrary profiles cause both even- and odd-order distortion. As anticipated in Section 4.3.3, the LO leakage caused by uneven profiles is very large.

Thanks to the continuous version of the analytical model, it is possible to calculate the nonlinearity in closed form. For example, the first phase error profile of Figure 5.12 can be expressed as

$$\frac{\tilde{\varphi}(a)}{2\pi f_c} = d_{max}(1 - 4a^2), \tag{5.10}$$

where $a \in [-1/2, +1/2]$, and d_{max} is the maximum amount of LO delay mismatch, reached for $a = 0$. The primitive of (5.10) is then given by

$$\Psi(a) = \int \tilde{\varphi}(a)da = 2\pi f_c d_{max}\left(a - \frac{4}{3}a^3\right). \tag{5.11}$$

For a single-tone input signal $\tilde{x}(t) = 0.5\cos(2\pi f_0 t)$, the error signal is calculated according to (4.39), yielding

$$\begin{aligned} e_{BB}(t) &= \Psi\left(\frac{1}{2}\cos(2\pi f_0 t)\right) \\ &= 2\pi f_c d_{max}\left(\frac{1}{2}\cos(2\pi f_0 t) - \frac{1}{6}\cos^3(2\pi f_0 t)\right) \\ &= \frac{1}{2}\pi f_c d_{max}\left(\frac{3}{2}\cos(2\pi f_0 t) - \frac{1}{6}\cos(2\pi 3 f_0 t)\right). \end{aligned} \tag{5.12}$$

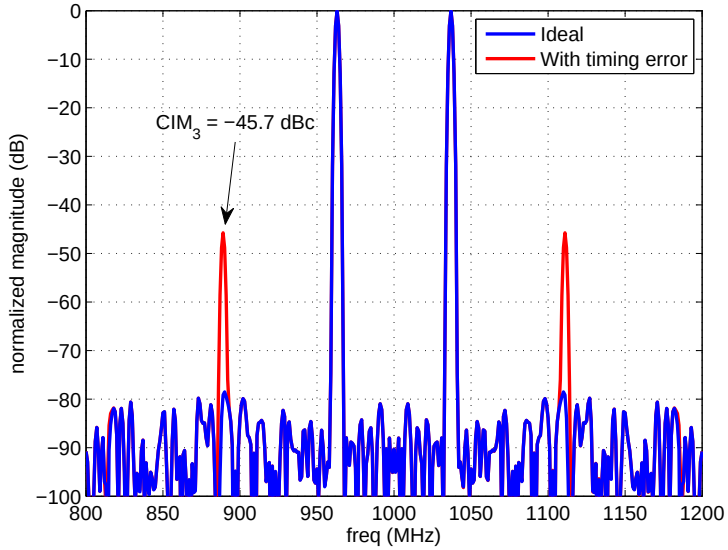

(a) *Profile (1)*

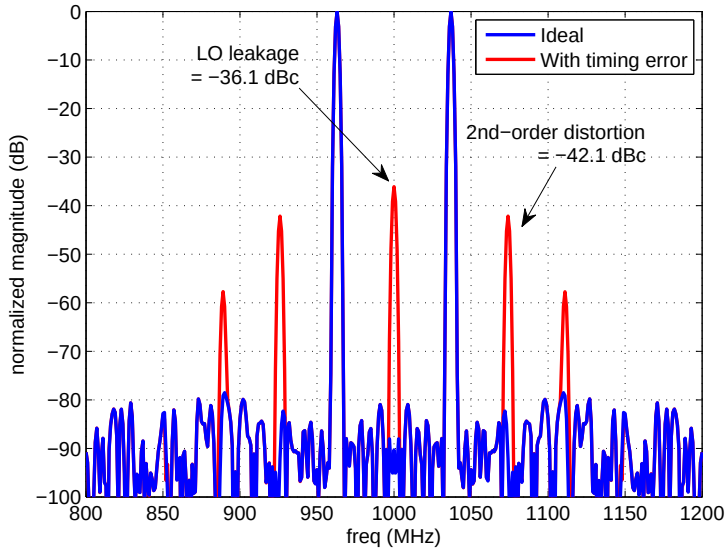

(b) *Profile (2)*

Figure 5.11: Output spectra of single RF-DAC with CW input signal, and two different second-order LO timing error profiles (see Figure 5.12). Simulation on a 10-bit fully thermometer-coded converter with $f_0 = 37$ MHz, $F_s = f_c = 1$ GHz. The maximum delay mismatch between different cells is $d_{max} = 1\% \cdot T_{LO}$.

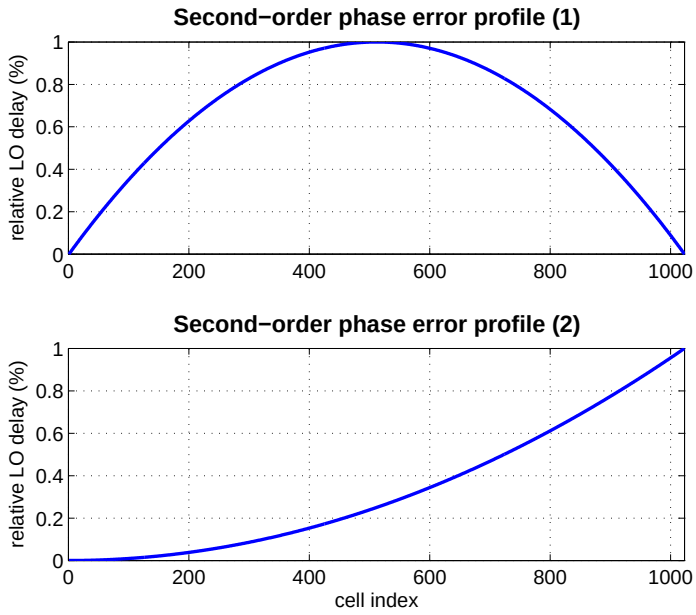

Figure 5.12: Second-order phase error profiles used for the simulations of Figure 5.11.

The third-order distortion CIM_3 is defined as the magnitude of the term at $3f_0$, relative to that of the wanted tone. If we neglect the first term of (5.12) (which does not represent distortion, and its amplitude is very small compared to that of $\tilde{x}(t)$), we finally get

$$CIM_3 = 20\log_{10}\left(\frac{1}{6}\pi f_c d_{max}\right) \qquad \text{[dB]}. \tag{5.13}$$

By substituting the values of f_c and d_{max} used for the simulation of Figure 5.11a into (5.13), we get $CIM_3 = -45.6$ dBc, which confirms the correctness of the analytical model. Moreover, (5.13) highlights that the distortion increases with the carrier frequency. This is rather obvious, because the delay mismatches account for a higher fraction of the LO period. This observation holds in general, for any kind of phase error profile.

5.6.2 Timing error on the LSB segment

Figure 5.13 shows the CW output spectrum of a single RF-DAC, with timing error dependent on the unit cell weights (i.e. the delay of the LO signal to each cell is directly proportional to the current provided by the cell itself). Such timing error affects only the LSB segment, since all unit cells on the MSB segment have the same weight, and thus the same delay. Once again, an increment of the noise floor can be observed from the output spectrum. This increment is similar to what would be observed with random Gaussian timing error on the LSB segment.

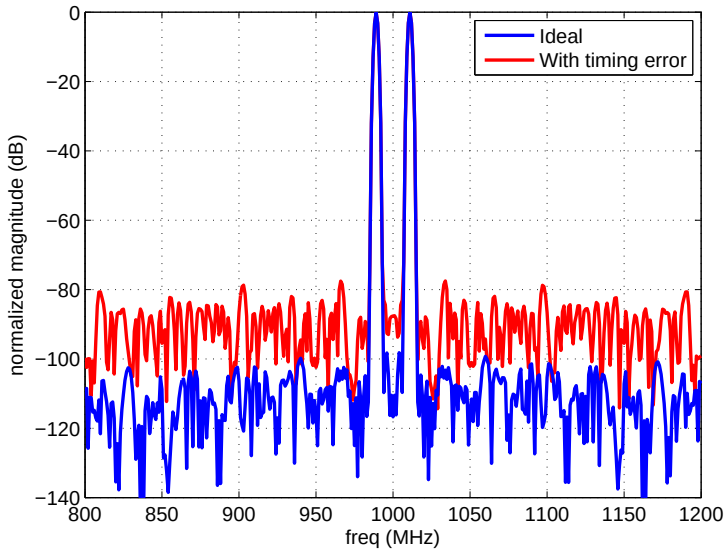

Figure 5.13: Output spectrum of single RF-DAC with CW input signal, and LO timing error dependent on the unit cell weights. Simulation with $f_0 = 11$ MHz, $F_s = 500$ MHz, $f_c = 1$ GHz. The maximum delay mismatch between different cells is $d_{max} = 1\% \cdot T_{LO}$.

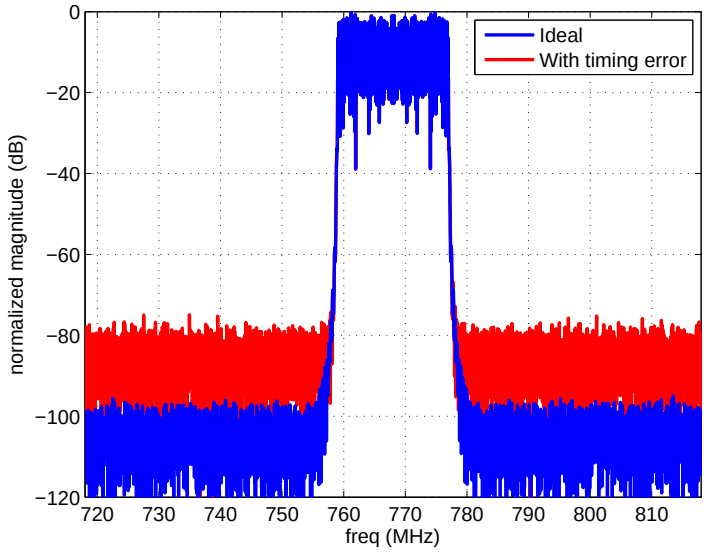

Figure 5.14: Output spectrum of single RF-DAC with 100 RB (20 MHz) LTE input signal (only real part), and LO timing error dependent on the unit cell weights. Simulation with $f_c = F_s = 768$ MHz. The maximum delay mismatch between different cells is $d_{max} = 1\% \cdot T_{LO}$.

Figure 5.14 shows the output spectrum of the RF-DAC with LTE input signal, under the same conditions as above. This simulation confirms the effects of timing error on the output noise floor (+20 dB in this example, corresponding to a $\approx$ 3-bit decrement in resolution). Therefore, as a general conclusion, it can be stated that it does make sense to increase N_{bits} in the RF-DAC, only if very accurate timing on the LO distribution tree can be achieved.

5.7 Summary

Table 5.2 summarizes the performance of the DDRM evaluated in this thesis. The presented results should be considered valid in the context of the particular application targeted by this work (LTE / LTE-A transmitter for mobile phone), but they may not hold in general.

The DDRM architecture is inherently wideband, as the only frequency-selective part is the RF matching network. However, the wide range of supported carrier frequencies (0.7 - 3.8 GHz) poses serious implementation challenges, and multiple RF front-ends may be required in order to cover all LTE / LTE-A bands. The third-order nonlinearity (CIM_3) is severely affected by many DDRM impairments, hence the -60 dBc target may be challenging to meet. The LO leakage benefits from the missing analog baseband signal processing. The finite IRR is intrinsic to the DDRM architecture, and its lower bound is only a function of the ratio f_c/f_0. Both ACLR and EVM are affected by the nonlinearities of the modulator, but the specifications leave a very large margin for signal degradation. On the other hand, the -160 dBc/Hz noise floor target translates into very tight linearity and timing requirements for the two RF-DACs. Thereby, as a general conclusion, it can be stated that more practical methods to reduce the out-of-band noise in all-digital transmitters should be researched.

Parameter	**Performance**
Channel bandwidth	$+$
Carrier frequency	$-$
CIM_3	$-$
LO leakage	$+$
IRR	$-$
EVM	$++$
ACLR	$++$
Noise floor	$--$

Table 5.2: Summary of DDRM performance.

Chapter 6

Conclusion

This thesis presents a thorough system-level analysis of an all-digital 4G transmitter based on the DDRM architecture. First, a brief overview of the LTE / LTE-A radio standards is given, and the transmitter structure is introduced. The RF specifications for the I-Q modulator are then defined and discussed. These specifications are used to determine, through MATLAB simulations, the system-level requirements that must be fulfilled by the two RF-DACs. Moreover, in order to fully understand the DDRM operation in presence of non-idealities, the major RF-DAC impairments are subject of a detailed mathematical analysis. In particular, the analytical model of timing error in the LO signal distribution is developed and verified through simulations.

Already at an early stage of this project, it has become clear that Error Vector Magnitude is something more than a simple specification for the digital TX. The reason is that EVM measurement requires the complete modeling of a baseband LTE demodulator. For this reason, the new goal of creating a baseband LTE environment has soon arisen. This target has led to the MATLAB implementation of a powerful baseband signal generator/demodulator, completed with ideal RX chain. The new LTE environment not only enables to measure EVM, but also allows to create and demodulate test vectors with arbitrary parameters, like the oversampling ratio. The possibility to play around with LTE parameters is by far preferable than being limited by the few available options in commercial softwares like Agilent Signal Studio. Furthermore, a good understanding of LTE and LTE-A has proven unquestionably helpful in the context of the larger project to which this thesis is related. It is also hoped that this study will serve as a useful and practical reference for other people.

The main goal of this work has been to evaluate whether it is possible to use an RF-DAC type of digital TX in a 4G mobile handset, without the need of analog filtering at the RF output. The RF-DAC requirements that were found confirm that this goal is very challenging.

The main benefit of the DDRM architecture is that the analog baseband filter is no longer necessary, because its functionality is replaced by the digital interpolation chain. Moreover, the single upconversion cell driven by digital signals is easier to design with respect to an analog mixer. In addition, the power control can be directly performed by the biasing circuitry of the converters, without the need of

extra variable-gain amplifiers.

These advantages come at the expense of much more challenging requirements for the D/A converter. The 14-bit resolution cannot be achieved without calibration of the static nonlinearity. Furthermore, the timing requirements for the distributed LO signal, in terms of both jitter and timing error, become very tight. Missing these requirements results in higher out-of-band noise, which can potentially disturb other receive bands. Therefore, a separate SAW filter must be inserted to isolate each RX from the TX, which is very undesirable in multiband systems like LTE / LTE-A.

It is believed that further progress in silicon technology will strengthen the need for digital TX architectures even more. However, there is little point of moving towards digital RF, if all the saved design effort has to be spent on the D/A converter. Hence, new methods to reduce the out-of-band noise in all-digital transmitters should be researched, in order to really render the digital TX solution more attractive than its analog counterpart.

Bibliography

[1] P. Eloranta and P. Seppinen, "Direct-digital RF modulator IC in 0.13 μm CMOS for wide-band multi-radio applications," in *IEEE Int. Solid-State Circuits Conf. Dig. Tech. Papers*, 2005, pp. 532–615.

[2] P. Eloranta, P. Seppinen, S. Kallioinen, T. Saarela, and A. Pärssinen, "A WCDMA transmitter in 0.13 μm CMOS using direct-digital RF modulator," in *IEEE Int. Solid-State Circuits Conf. Dig. Tech. Papers*, 2007, pp. 340–607.

[3] ——, "A multimode transmitter in 0.13 μm CMOS using direct-digital RF modulator," *IEEE Journal of Solid-State Circuits*, vol. 42, no. 12, pp. 2774–2784, Dec. 2007.

[4] P. Eloranta, P. Seppinen, and A. Pärssinen, "Direct-digital RF-modulator: a multi-function architecture for a system-independent radio transmitter," *IEEE Communications Magazine*, vol. 46, no. 4, pp. 144–151, Apr. 2008.

[5] A. Jerng and C. Sodini, "A wideband $\Delta\Sigma$ digital-RF modulator for high data rate transmitters," *IEEE Journal of Solid-State Circuits*, vol. 42, no. 8, pp. 1710–1722, Aug. 2007.

[6] A. Pozsgay, T. Zounes, R. Hossain, M. Boulemnakher, V. Knopik, and S. Grange, "A fully digital 65nm CMOS transmitter for the 2.4-to-2.7GHz WiFi/WiMAX bands using 5.4GHz $\Delta\Sigma$ RF DACs," in *IEEE Int. Solid-State Circuits Conf. Dig. Tech. Papers*, 2008, pp. 360–619.

[7] N. Zimmermann, B. Thiel, R. Negra, and S. Heinen, "System architecture of an RF-DAC based multistandard transmitter," in *52nd IEEE Int. Midwest Symp. Circuits and Systems*, Aug. 2009, pp. 248–251.

[8] Z. Boos, A. Menkhoff, F. Kuttner, M. Schimper, J. Moreira, H. Geltinger, T. Gossmann, P. Pfann, A. Belitzer, and T. Bauernfeind, "A fully digital multimode polar transmitter employing 17b RF DAC in 3G mode," in *IEEE Int. Solid-State Circuits Conf. Dig. Tech. Papers*, 2011, pp. 376–378.

[9] V. Giannini, M. Ingels, T. Sano, B. Debaillie, J. Borremans, and J. Craninckx, "A multiband LTE SAW-less modulator with -160 dBc/Hz RX-band noise in 40nm LP CMOS," in *IEEE Int. Solid-State Circuits Conf. Dig. Tech. Papers*, 2011, pp. 374–376.

[10] O. Oliaei, M. Kirschenmann, D. Newman, K. Hausmann, H. Xie, P. Rakers, M. Rahman, M. Gomez, C. Yu, B. Gilsdorf, and K. Sakamoto, "A multiband multimode transmitter without driver amplifier," in *IEEE Int. Solid-State Circuits Conf. Dig. Tech. Papers*, 2012, pp. 164–166.

[11] "Framework and overall objectives of the future development of IMT-2000 and systems beyond IMT-2000," Recommendation ITU-R M.1645, Jun. 2003.

[12] "ITU World Radiocommunication Seminar highlights future communication technologies," Press Release, Dec. 2010. [Online]. Available: http://www.itu.int/net/pressoffice/press_releases/2010/48.aspx

[13] S. Sesia, I. Toufik, and M. Baker, *LTE–the UMTS long term evolution: from theory to practice*, 2nd ed. Chichester: Wiley, 2011.

[14] J. Zyren, "Overview of the 3GPP long term evolution physical layer," White Paper, Freescale Semiconductor, Jul. 2007.

[15] S. Parkvall, E. Dahlman, A. Furuskar, Y. Jading, M. Olsson, S. Wanstedt, and K. Zangi, "LTE-Advanced - Evolving LTE towards IMT-Advanced," in *IEEE 68th Vehicular Technology Conf.*, Sep. 2008, pp. 1–5.

[16] B. Razavi, *RF Microelectronics*. Upper Saddle River (N.J.): Prentice Hall PTR, 1998.

[17] M. Kosunen, "Digital signal processing and digital-to-analog converters for wide-band transmitters," Ph.D. dissertation, Helsinki University of Technology, Department of Electrical and Communications Engineering, Electronic Circuit Design Laboratory, 2006.

[18] J. Vankka, J. Ketola, O. Vaananen, J. Sommarek, M. Kosunen, and K. Halonen, "A GSM/EDGE/WCDMA modulator with on-chip D/A converter for base station," in *IEEE Int. Solid-State Circuits Conf. Dig. Tech. Papers*, 2002, pp. 236–463.

[19] M. Kosunen, J. Vankka, M. Waltari, and K. Halonen, "A multicarrier QAM modulator for WCDMA base-station with on-chip D/A converter," *IEEE Transactions on Very Large Scale Integration (VLSI) Systems*, vol. 13, no. 2, pp. 181–190, Feb. 2005.

[20] *User Equipment (UE) radio transmission and reception*, 3GPP Std. TS 36.101, Rev. 11.0.0, Mar. 2012.

[21] Y. Li, J. Lopez, P.-H. Wu, W. Hu, R. Wu, and D. Lie, "A SiGe envelope-tracking power amplifier with an integrated CMOS envelope modulator for mobile WiMAX/3GPP LTE transmitters," *IEEE Transactions on Microwave Theory and Techniques*, vol. 59, no. 10, pp. 2525–2536, Oct. 2011.

[22] H. Myung, J. Lim, and D. Goodman, "Peak-to-average power ratio of single carrier FDMA signals with pulse shaping," in *IEEE 17th Int. Symp. Personal, Indoor and Mobile Radio Communications*, Sep. 2006, pp. 1–5.

[23] A. W. Scott, *RF Measurements for Cellular Phones and Wireless Data Systems*. Wiley & Sons Inc.: Hoboken, New Jersey, 2008, ch. 32.

[24] *Physical channels and modulation*, 3GPP Std. TS 36.211, Rev. 10.4.0, Dec. 2011.

[25] *N7624B Signal Studio for 3GPP LTE FDD*, Online Documentation, Agilent Technologies, Inc., Dec. 2011.

[26] Motorola, "R1-062061: Uplink DC subcarrier distortion considerations in LTE," 3GPP TSG RAN WG1, meeting 46, Tallinn, Estonia, Aug. 2006.

[27] P. Bloomfield, *Fourier Analysis of Time Series: An Introduction*. New York: Wiley-Interscience, 2000, p. 69.

[28] D. A. Johns and K. Martin, *Analog Integrated Circuit Design*. New York: John Wiley, 1997.

[29] S. K. Mitra, *Digital Signal Processing: A Computer-Based Approach*, 2nd ed. New York: McGraw-Hill, 2001.

[30] K. Lakshmikumar, R. Hadaway, and M. Copeland, "Characterisation and modeling of mismatch in MOS transistors for precision analog design," *IEEE Journal of Solid-State Circuits*, vol. 21, no. 6, pp. 1057–1066, Dec. 1986.

[31] M. Pelgrom, A. Duinmaijer, and A. Welbers, "Matching properties of MOS transistors," *IEEE Journal of Solid-State Circuits*, vol. 24, no. 5, pp. 1433–1439, Oct. 1989.

[32] M. Kosunen and K. Halonen, "Sampling jitter and power supply interference in current-steering D/A converters," in *Proc. 2005 European Conf. Circuit Theory and Design*, vol. 1, Aug.-Sept. 2005, pp. I/305–I/308.

[33] V. Turunen, T. Nieminen, M. Kosunen, and K. Halonen, "12-bit 2.4 GHz D/A upconverter," in *18th European Conf. Circuit Theory and Design*, Aug. 2007, pp. 228–231.

[34] T. Chen and G. Gielen, "The analysis and improvement of a current-steering DACs dynamic SFDR-I: the cell-dependent delay differences," *IEEE Transactions on Circuits and Systems—Part I: Regular Papers*, vol. 53, no. 1, pp. 3–15, Jan. 2006.

[35] Y. Tang, H. Hegt, and A. van Roermund, "Predictive timing error calibration technique for RF current-steering DACs," in *IEEE Int. Symp. Circuits and Systems*, May 2008, pp. 228–231.

[36] S. Luschas and H.-S. Lee, "Output impedance requirements for DACs," in *Proc. 2003 Int. Symp. Circuits and Systems*, vol. 1, May 2003, pp. I/861–I/864.

[37] E. Roverato, M. Kosunen, J. Lemberg, K. Stadius, J. Ryynänen, P. Eloranta, R. Kaunisto, and A. Pärssinen, "A programmable DSP front-end for all-digital 4G transmitters," unpublished.

Appendix A

Generation of the Demodulation Reference Signal

This appendix explains in details how to generate the Demodulation Reference Signal for LTE SC-FDMA vectors, according to the procedure described in 3GPP specifications [24]. Emphasis is especially given to clarify the points that are a bit obscure in [24]. Only the details that are meaningful to this work are treated here, whereas all of the "exotic" cases (e.g. when less than 3 RBs are active, and so on) are left out.

Before moving to the generation procedure, it is good to define a few parameters that will be used throughout the algorithm.

- The length of the reference signal sequence is the same as the number of active subcarriers, which equals N_{sc} for full-filled LTE vectors (the only case considered in this work).
- Different base sequences are identified by two numbers: $u \in \{0, \ldots, 29\}$ is the group number, and $\nu \in \{0, 1\}$ is the base sequence number within the group. In this work it is assumed $u = \nu = 0$ all the time, i.e. both group and sequence hopping are disabled.
- The Zadoff-Chu sequence length N_{ZC} is given by the largest prime number smaller than N_{sc}, which can be computed with MATLAB's built-in functions.
- Parameters $n_{DMRS}^{(1)}$ and $n_{DMRS}^{(2)}$ are needed to calculate the cyclic shift of the base sequence. Different values for these parameters are listed in [24], but in this work the simplest option $n_{DMRS}^{(1)} = n_{DMRS}^{(2)} = 0$ is assumed.

The generation of the DMRS starts from the q-th root Zadoff-Chu sequence

$$x_q(m) = e^{-j\frac{\pi q m(m+1)}{N_{ZC}}}, \qquad m = 0, \ldots, N_{ZC} - 1, \tag{A1}$$

where q is given by

$$\begin{aligned} q &= \lfloor \bar{q} + 1/2 \rfloor + \nu \cdot (-1)^{\lfloor 2\bar{q} \rfloor}, \\ \bar{q} &= N_{ZC} \cdot (u+1)/31, \end{aligned} \tag{A2}$$

and $\lfloor x \rfloor$ denotes the integer part of x.

After that, the base sequence is calculated from $x_q(m)$ as

$$\bar{r}(k) = x_q(k \mod N_{ZC}), \qquad k = 0, \ldots, N_{sc} - 1. \tag{A3}$$

If less than 3 RBs are active, the base sequence $\bar{r}(k)$ is defined in a different way. However, this case is not treated here.

Multiple reference signal sequences are defined by applying different values of a pseudorandom cyclic shift α to the base sequence, according to

$$r_\alpha(k) = e^{j\alpha k}\bar{r}(k), \qquad k = 0, \ldots, N_{sc} - 1. \tag{A4}$$

In this work, each of the reference signal sequences $r_\alpha(k)$ is directly used as a vector of subcarrier amplitudes for the 4^{th} SC-FDMA symbol of each slot. Other cases are considered in [24], but they are not presented here. The output $N_{sc} \times N_{slots}$ matrix r used in the SC-FDMA signal generator is thus defined as

$$r(k, n_s) = r_{\alpha(n_s)}(k), \qquad k = 0, \ldots, N_{sc} - 1, \tag{A5}$$

where $\alpha(n_s)$ is calculated for each slot $n_s = 0, \ldots, N_{slots} - 1$, according to the procedure described below.

The procedure starts by initializing the pseudorandom sequence generator $c(i)$ defined in [24]. In this work, the initial value is assumed to be $c_{init} = 0$. Notice that $c(i)$ *must* be defined exactly as in [24], otherwise the generated DMRS will assume unknown values, and thus it cannot be used as a reference signal. The pseudorandom algorithm is based on a length-31 Gold sequence, and it is not reported here.

The pseudorandom sequence generator is then used to calculate the quantity $n_{PN}(n_s)$ as

$$n_{PN}(n_s) = \sum_{i=0}^{7} c\big(8N_{symb} \cdot n_s + i\big) \cdot 2^i, \qquad n_s = 0, \ldots, N_{slots} - 1, \tag{A6}$$

where $N_{symb} = 7$ is the number of SC-FDMA symbols per slot assuming normal CP length.

Thereafter, the quantity $n_{PN}(n_s)$ is used to calculate

$$n_{cs}(n_s) = \big(n^{(1)}_{DMRS} + n^{(2)}_{DMRS} + n_{PN}(n_s)\big) \mod 12, \tag{A7}$$

and the pseudorandom cyclic shift is finally defined as

$$\alpha(n_s) = \frac{2\pi n_{cs}(n_s)}{12}, \tag{A8}$$

for $n_s = 0, \ldots, N_{slots} - 1$.

The DMRS generation algorithm was tested by comparing the sequences produced by the above algorithm implemented in MATLAB, to the sequences that were found in LTE SC-FDMA vectors generated with Agilent Signal Studio. The test was successfully performed on 25, 50, 100, and 100+100 RB vectors (i.e. 5, 10, 20, and 20+20 MHz channel bandwidths).

Appendix B

Derivation of the LO timing error model

In this appendix, the analytical model for the LO timing error in the RF-DAC is derived.[1] The derivation is performed for a differential, fully thermometer-coded converter, although the single-ended case would be easier to treat. The correctness of the presented procedure is verified in Section 5.6 through comparison with some MATLAB simulations. These simulations also prove the reasonableness of the simplifying assumptions that will be made throughout the derivation.

We start from the basic definition of thermometer-coding, where the quantized signal $x_q(n)$ is obtained by means of summing a number of equal, unity-weighted elements. This can be expressed mathematically as

$$x_q(n) = \sum_{i=-(2^{B-1}-1)}^{2^{B-1}-1} b_i(n), \tag{B1}$$

where B is the binary word length, and $b_i(n)$ is the "thermometer bit" function, defined from the unquantized signal $x(n)$ as

$$b_i(n) = \frac{1}{2}\operatorname{sgn}\big(x(n) - i\big) = \begin{cases} -1/2, & x(n) < i, \\ 1/2, & x(n) \geqslant i. \end{cases} \tag{B2}$$

The above expressions can be better understood by looking to the transfer curve of a 2-bit uniform quantizer, shown in Figure B1. It is clear that, for each $i \in \{-1, 0, 1\}$, the corresponding thermometer bit switches its value from $-1/2$ to $1/2$ when x becomes greater than i.

According to the discussion in Section 4.3.3, in presence of LO timing error each thermometer bit is modulated by a phase-shifted version of the LO signal. The

[1] Although analytical timing error models have already been developed for high-speed DACs [34, 35], they do not describe the non-ideal distributed upconversion taking place in RF-DACs. Therefore, the derivation presented in this appendix was carried out independently from the results published in [34, 35].

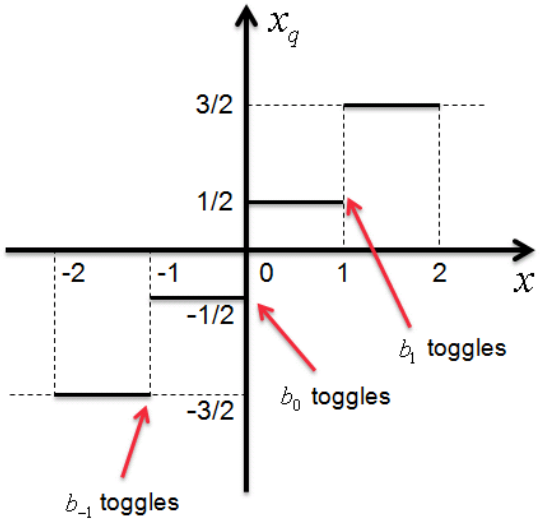

Figure B1: Transfer curve of a 2-bit uniform quantizer.

amount of shift for each unit element is given by the phase error profile $\varphi(i)$. The overall RF signal is thus

$$RF_{real}(t) = \sum_{i=-(2^{B-1}-1)}^{2^{B-1}-1} b_i(t) \cdot e^{j(2\pi f_c t + \varphi(i))}, \tag{B3}$$

where $b_i(t)$ is the continuous-time version of $b_i(n)$, defined as in (B2) but with $x(t)$ instead of $x(n)$ (i.e. here we are not considering zero-order hold).

Since $\varphi(i)$ was assumed to be much smaller than 1 (because the phase shift is just a small fraction of the LO period), the approximation $e^{j\varphi(i)} \approx 1 + j\varphi(i)$ is valid, and (B3) becomes

$$RF_{real}(t) = RF_{ideal}(t) + e_{RF}(t), \tag{B4}$$

where $RF_{ideal}(t)$ is the ideal RF signal with no timing error, the RF error is

$$\begin{aligned} e_{RF}(t) &= \sum_{i=-(2^{B-1}-1)}^{2^{B-1}-1} b_i(t) \cdot j\varphi(i) \cdot e^{j2\pi f_c t} \\ &= e_{BB}(t) \cdot e^{j\left(2\pi f_c t + \frac{\pi}{2}\right)}, \end{aligned} \tag{B5}$$

and the BB error

$$e_{BB}(t) = \sum_{i=-(2^{B-1}-1)}^{2^{B-1}-1} b_i(t)\varphi(i). \tag{B6}$$

By exploiting the definition of $b_i(t)$, the sum in (B6) can be broken into two

parts, yielding

$$\begin{aligned} e_{BB}(t) &= \frac{1}{2}\left[\sum_{-(2^{B-1}-1)}^{\lfloor x(t)\rfloor}\varphi(i)\right] - \frac{1}{2}\left[\sum_{\lceil x(t)\rceil}^{2^{B-1}-1}\varphi(i)\right] \\ &= \frac{1}{2}\left[\sum_{-(2^{B-1}-1)}^{-1}\varphi(i) + \sum_{0}^{\lfloor x(t)\rfloor}\varphi(i)\right] - \frac{1}{2}\left[\sum_{\lceil x(t)\rceil}^{0}\varphi(i) + \sum_{1}^{2^{B-1}-1}\varphi(i)\right] \\ &\approx \sum_{0}^{\text{round}[x(t)]}\varphi(i) - \frac{1}{2}\left[\sum_{1}^{2^{B-1}-1}\varphi(i) - \sum_{-(2^{B-1}-1)}^{-1}\varphi(i)\right], \end{aligned} \tag{B7}$$

where all the sums are intended to be "with sign" (i.e. $\sum_a^b = -\sum_b^a$), and round$[x]$ is the closest integer to x.

The above result can be expressed more clearly by following a different approach. Let us restart from (B1) and (B2) by normalizing $x_q(n)$ to the range $[-1/2, +1/2]$. Since the extreme values assumed by the quantized signal are $\pm(2^B-1)/2$, the characteristic of Figure B1 must be scaled by a factor $\Delta a = 1/(2^B-1)$. Equation (B1) then modifies to

$$\begin{aligned} \tilde{x}_q(n) &= \Delta a \cdot \left[\sum_{i=-(2^{B-1}-1)}^{2^{B-1}-1}\tilde{b}_i(n)\right] \\ &= \sum_{i=-(2^{B-1}-1)}^{2^{B-1}-1}\left[\frac{1}{2}\operatorname{sgn}\big(\tilde{x}(n) - i\Delta a\big)\right]\cdot\Delta a, \end{aligned} \tag{B8}$$

where the tilde denotes the normalized quantities.

It is now obvious that, if $B \to +\infty$, then Δa becomes infinitesimal, and the extreme values assumed by $i\Delta a$ approach $\pm 1/2$. Thereby, the sum in (B8) turns into an integral, yielding

$$\tilde{x}_q(n) = \frac{1}{2}\int_{-\frac{1}{2}}^{+\frac{1}{2}}\operatorname{sgn}\big(\tilde{x}(n) - a\big)da = \tilde{x}(n), \tag{B9}$$

where the rightmost equality, reported just for completeness, can be easily proven by splitting the integral into two parts (from $-1/2$ to $\tilde{x}(n)$, and from $\tilde{x}(n)$ to $+1/2$).

By similarity with equations (B3) to (B6), the baseband error signal can be now calculated as

$$\begin{aligned} e_{BB}(t) &= \frac{1}{2}\int_{-\frac{1}{2}}^{+\frac{1}{2}}\tilde{\varphi}(a)\operatorname{sgn}\big(\tilde{x}(t) - a\big)da \\ &= \frac{1}{2}\left[\int_{-\frac{1}{2}}^{\tilde{x}(t)}\tilde{\varphi}(a)da - \int_{\tilde{x}(t)}^{+\frac{1}{2}}\tilde{\varphi}(a)da\right] \\ &= \Psi\big(\tilde{x}(t)\big) - \frac{\Psi\left(\frac{1}{2}\right) + \Psi\left(-\frac{1}{2}\right)}{2}, \end{aligned} \tag{B10}$$

where $\tilde{\varphi}(a)$ is the continuous version of the phase error profile function with normalized index $a \in [-1/2, +1/2]$, and $\Psi(a)$ is given by

$$\Psi(a) = \int \tilde{\varphi}(a) da. \tag{B11}$$

The timing error model described by (B10) and (B11) is nothing else than the continuous version of that described by (B7). In both models, the baseband error $e_{BB}(t)$ is the sum of

- a constant term, which depends only on the phase error profile, and
- a time-varying term, which is a function of both input signal and phase error profile.

The main advantage of the continuous model is that it allows to calculate the error signal in closed form, if $\tilde{\varphi}(a)$ is some "textbook" function of a (e.g. linear, parabolic, etc.). However, the phase error profile is in general arbitrary, and the discrete model has to be used then.

Appendix C

Image Rejection Ratio of the DDRM

In order to understand the reason for finite IRR in the DDRM, let us first study what happens when a single, digital baseband tone with frequency f_0 undergoes ZOH and upconversion with sinusoidal carrier. The discrete-time, complex baseband signal is given by

$$x(n) = e^{j2\pi f_0 n T_s}, \tag{C1}$$

where $T_s = 1/F_s$ is the sampling period. As explained in Section 4.2.2, when $x(n)$ is converted to continuous-time through the ZOH, its spectrum (which is an infinite series of unity-amplitude tones at frequencies $f_0 + kF_s$, $k \in \mathbb{Z}$) is attenuated by a *sinc* response. The result can be thus expressed as

$$x_{ZOH}(t) = \sum_{k=-\infty}^{+\infty} \mathrm{sinc}\left(\frac{kF_s + f_0}{F_s}\right) \cdot e^{j2\pi(kF_s+f_0)t}. \tag{C2}$$

Ideal upconversion to RF is performed by means of multiplication with a complex sinusoidal carrier, according to

$$x_{RF}(t) = x_{ZOH}(t) \cdot e^{j2\pi f_c t}, \tag{C3}$$

which corresponds to right-shifting the spectrum of $x_{ZOH}(t)$ by a quantity f_c. However, as discussed in Section 2.2, the I-Q modulator only takes the real part of (C3) as output. This is equivalent to mirroring its spectrum with respect to the y-axis, as illustrated in Figure C1. Because f_c should be an integer multiple of F_s in the DDRM (see Section 2.3.2), such operation causes one of the repetition tones to be mirrored exactly to the image frequency $f_c - f_0$.

In order to derive an analytical expression for the IRR in this simplified case, let

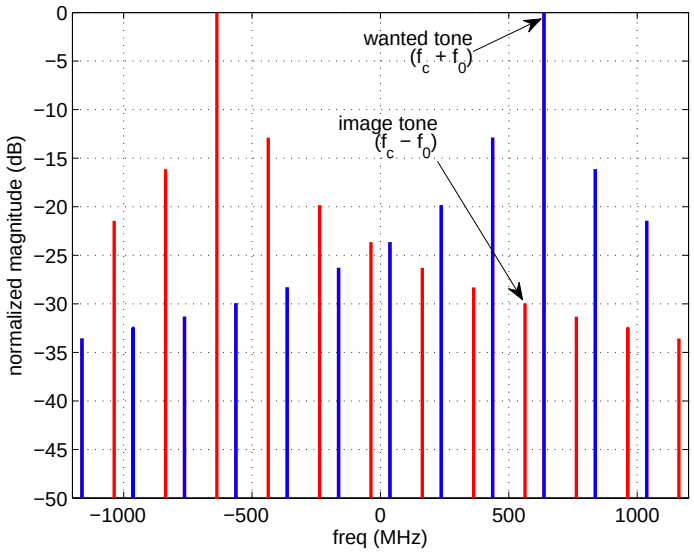

Figure C1: When $x_{ZOH}(t)$ undergoes ideal upconversion, its spectrum is right-shifted by an amount f_c (blue tones). When the real part of $x_{RF}(t)$ is taken, the "mirror" spectrum is then added to the output (red tones). This is the reason for the image tone. Simulation performed with $f_c = 600$ MHz, $f_0 = 37$ MHz, $F_s = 200$ MHz.

us consider the two terms of (C2) located at f_0 and $-2f_c + f_0$:[1]

$$\begin{aligned} x_{ZOH}(t) = \operatorname{sinc}\left(\frac{f_0}{F_s}\right) \cdot e^{j2\pi f_0 t} + \\ \operatorname{sinc}\left(\frac{-2f_c + f_0}{F_s}\right) \cdot e^{j2\pi(-2f_c+f_0)t} + \dots . \end{aligned} \tag{C4}$$

These tones are then upconverted through multiplication with $e^{j2\pi f_c t}$, resulting in

$$\begin{aligned} x_{RF}(t) = \operatorname{sinc}\left(\frac{f_0}{F_s}\right) \cdot e^{j2\pi(f_c+f_0)t} + \\ \operatorname{sinc}\left(\frac{-2f_c + f_0}{F_s}\right) \cdot e^{j2\pi(-f_c+f_0)t} + \dots . \end{aligned} \tag{C5}$$

Taking the real part of (C5) yields

$$\begin{aligned} \operatorname{Re}\big[x_{RF}(t)\big] = \operatorname{sinc}\left(\frac{f_0}{F_s}\right) \cdot \cos\big(2\pi(f_c + f_0)t\big) + \\ \operatorname{sinc}\left(\frac{2f_c - f_0}{F_s}\right) \cdot \cos\big(2\pi(f_c - f_0)t\big) + \dots , \end{aligned} \tag{C6}$$

[1] If f_c is a multiple of F_s, then $-2f_c$ is also a multiple of F_s, and thus there is a tone located at $-2f_c + f_0$.

where the fact that both *cos* and *sinc* are even functions was exploited.

Equation (C6) explicitly shows the presence of the image tone in the output RF signal. The IRR can be thus calculated as the ratio (in decibels) between the amplitudes of the two tones, according to

$$\begin{aligned} IRR &= 20\log_{10}\frac{\left|\mathrm{sinc}\left(\frac{2f_c-f_0}{F_s}\right)\right|}{\left|\mathrm{sinc}\left(\frac{f_0}{F_s}\right)\right|} \\ &= 20\log_{10}\frac{\left|\frac{\sin(\pi(2f_c-f_0)/F_s)}{\pi(2f_c-f_0)/F_s}\right|}{\frac{\sin(\pi f_0/F_s)}{\pi f_0/F_s}} \\ &= 20\log_{10}\left(\frac{f_0}{2f_c-f_0}\cdot\frac{\left|\sin(2\pi f_c/F_s-\pi f_0/F_s)\right|}{\sin(\pi f_0/F_s)}\right) \\ &= 20\log_{10}\left(\frac{1}{2f_c/f_0-1}\cdot\frac{\left|-\sin(\pi f_0/F_s)\right|}{\sin(\pi f_0/F_s)}\right) \\ &= -20\log_{10}\left(\frac{2f_c}{f_0}-1\right), \end{aligned} \tag{C7}$$

where the simplification between the third and fourth line holds because f_c/F_s is integer.

Equation (C7) reveals a curious property: the IRR does *not* depend on the sampling rate F_s. This feature can be intuitively understood as follows. When F_s is increased, the main tone of $x_{ZOH}(t)$ (i.e. the one at f_0) is less affected by the *sinc* attenuation of the ZOH. In other words, its amplitude gets larger. However, at the same time, the tone at $-2f_c+f_0$ belongs to a *sinc* lobe of lower order (i.e. with less attenuation), because the integer ratio f_c/F_s is smaller. Hence, in the end its amplitude becomes also larger. The net result is that these two effects perfectly compensate each other, and the IRR remains unchanged.

Unfortunately, in the DDRM the situation is much more complicated than the scenario described above, because the LO signal is a square-wave. Hence, each of the LO harmonics at $3f_c$, $5f_c$, $7f_c$, etc. will also convert a couple of tones of $x_{ZOH}(t)$ to frequencies $f_c \pm f_0$.

The square-wave carrier can be expressed analytically by means of its complex Fourier series

$$\begin{aligned} c(t) &= \frac{4}{\pi}\sum_{k=0}^{+\infty}\frac{(-1)^k}{2k+1}\cdot e^{j2\pi(-1)^k(2k+1)f_c t} \\ &= \frac{4}{\pi}e^{j2\pi f_c t}-\frac{4}{3\pi}e^{-j2\pi 3f_c t}+\frac{4}{5\pi}e^{j2\pi 5f_c t}-\frac{4}{7\pi}e^{-j2\pi 7f_c t}+\ldots. \end{aligned} \tag{C8}$$

It is easy to show that the real and imaginary parts of $c(t)$ are two square-waves with the same 90° phase difference as in the complex sinusoidal carrier $e^{j2\pi f_c t}$.

By proceeding similarly to equations (C4)-(C7) for each of the harmonics in (C8),

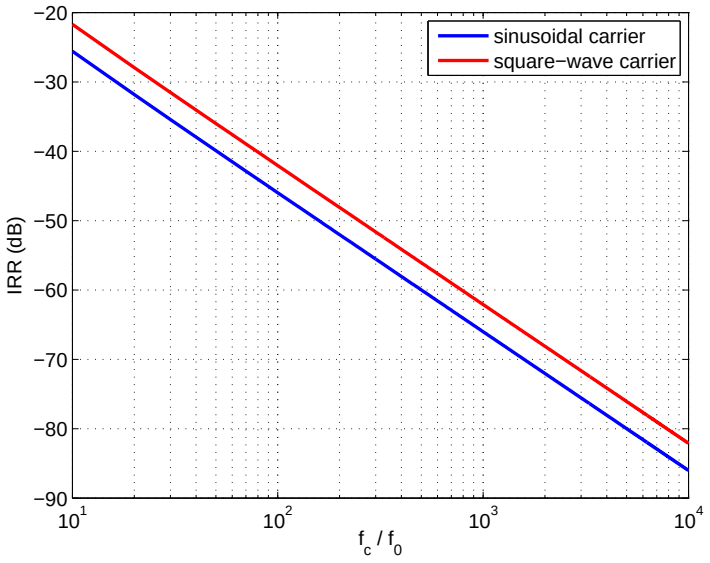

Figure C2: IRR of the DDRM, as a function of the ratio between carrier frequency and baseband tone frequency.

one can derive the following expression for the IRR of the DDRM:

$$IRR = 20\log_{10}\frac{\left|\sum_{k=0}^{+\infty}\frac{(-1)^k}{(2k+1)\left\{-2\cdot\left[(-1)^k\cdot k+|\cos(k\pi/2)|\right]\cdot f_c+f_0\right\}}\right|}{\left|\sum_{k=0}^{+\infty}\frac{(-1)^k}{(2k+1)\left\{-2\cdot\left[(-1)^k\cdot k-|\sin(k\pi/2)|\right]\cdot f_c+f_0\right\}}\right|}, \qquad \text{(C9)}$$

which shows no dependence on F_s like (C7).

Figure C2 plots (C7) and (C9) versus f_c/f_0. It can be seen that the difference between the two curves is approximately 4 dB over a wide range of ratios. This suggests that (C9) could be simplified to the more practical form

$$IRR \approx -20\log_{10}\left(\frac{2f_c}{f_0}-1\right)+4. \qquad \text{(C10)}$$

Equation (C10) can be verified through MATLAB simulations. However, this is actually just a lower bound for the IRR of a DDRM. In practice, there are a multitude of factors that can degrade this figure of merit (the most plausible being the phase shift between in-phase and quadrature carriers different from 90°). For example, the experimental results in [3] show a measured IRR of -43 dB for a 1.6 MHz baseband tone with 1.9 GHz carrier frequency, whereas (C10) gives a theoretical IRR of -64 dB with the same values of f_0 and f_c.